USGS
science for a changing world

Geology and Geophysics Applied to Groundwater Hydrology at Fort Irwin, California

David C. Buesch, Editor

Time-Domain Electromagnetic Surveys at Fort Irwin, San Bernardino County, California, 2010–12

By Matthew K. Burgess and Paul A. Bedrosian

Open-File Report 2013–1024–F

U.S. Department of the Interior
U.S. Geological Survey

U.S. Department of the Interior
SALLY JEWELL, Secretary

U.S. Geological Survey
Suzette M. Kimball, Acting Director

U.S. Geological Survey, Reston, Virginia: 2014

Suggested citation:
Burgess, M.K., and Bedrosian, P.A., 2014, Time-domain electromagnetic surveys at Fort Irwin, San Bernardino County, California, 2010–12, chap. F *of* Buesch, D.C., ed., Geology and geophysics applied to groundwater hydrology at Fort Irwin, California: U.S. Geological Survey Open-File Report 2013–1024, 64 p., *http://dx.doi.org/10.3133/ofr20131024F*.

ISSN 2331-1258 (online)

Contents

Figures

Tables

Appendixes

Conversion Factors

Inch/Pound to SI

Multiply	By	To obtain
	Length	
foot (ft)	0.3048	meter (m)
mile (mi)	1.609	kilometer (km)
	Area	
square foot (ft^2)	0.09290	square meter (m^2)
	Flow rate	
gallon per minute (gal/min)	0.06309	liter per second (L/s)
	Transmissivity*	
foot squared per day (ft^2/d)	0.09290	meter squared per day (m^2/d)

SI to Inch/Pound

Multiply	By	To obtain
	Length	
meter (m)	3.281	foot (ft)
	Area	
square meter (m^2)	10.76	square foot (ft^2)

*Transmissivity: The standard unit for transmissivity is cubic foot per day per square foot times foot of aquifer thickness [(ft^3/d)/ft^2]ft. In this report, the mathematically reduced form, foot squared per day (ft^2/d), is used for convenience.

Datum

Vertical coordinate information is referenced to the North American Vertical Datum of 1988 (NAVD 88).

All elevations are presented in feet above mean sea level (asl).

Time-Domain Electromagnetic Surveys at Fort Irwin, San Bernardino County, California, 2010–12

By Matthew K. Burgess and Paul A. Bedrosian

Abstract

Between 2010 and 2012, a total of 79 time-domain electromagnetic (TEM) soundings were collected in 12 groundwater basins in the U.S. Army Fort Irwin National Training Center (NTC) study area to help improve the understanding of the hydrogeology of the NTC. The TEM data are discussed in this chapter in the context of geologic observations of the study area, the details of which are provided in the other chapters of this volume. Selection of locations for TEM soundings in unexplored basins was guided by gravity data that estimated depth to pre-Tertiary basement complex of crystalline rock and alluvial thickness. Some TEM data were collected near boreholes with geophysical logs. The TEM response at locations near boreholes was used to evaluate sounding data for areas without boreholes. TEM models also were used to guide site selection of subsequent boreholes drilled as part of this study. Following borehole completion, geophysical logs were used to ground-truth and reinterpret previously collected TEM data. This iterative process was used to site subsequent TEM soundings and borehole locations as the study progressed. Although each groundwater subbasin within the NTC boundaries was explored using the TEM method, collection of TEM data was focused in those basins identified as best suited for development of water resources. At the NTC, TEM estimates of some lithologic thicknesses and electrical properties in the unsaturated zone are in good accordance with borehole data; however, water-table elevations were not easily identifiable from TEM data.

Introduction

Between 2010 and 2012, a total of 79 time-domain electromagnetic (TEM) soundings were collected in 12 groundwater basins in the U.S. Army Fort Irwin National Training Center (herein referenced to as NTC or base) study area to help improve the understanding of the hydrogeology of the base. The TEM method was used in this study to estimate subsurface electrical resistivity structure from the land surface to depths as great as 1,650 ft below land surface (bls), by deriving a one-dimensional (1D) resistivity model from data collected at the land surface. Electrical resistivity structure can serve as a proxy for layered Earth materials. When investigating the subsurface, changes to these materials or between material types, are expressed as changes in subsurface resistivity and can be identified by analyzing the Earth's response to the electromagnetic (EM) fields used in TEM and other EM methods. The layer-cake model of the Earth derived from these data can potentially identify significant geologic and hydrologic features.

The resistivity of near-surface Earth materials can vary by orders of magnitude, ranging from 100,000 ohm-m or more for dry carbonates and unweathered crystalline rocks to 100 ohm-m or less for saturated alluvium and as low as 1 ohm-m for clay (Palacky, 1987). In unconsolidated sediments, higher electrical resistivity is associated with coarse-grained deposits such as alluvial sand and gravel or

sandstone. Conversely, lower resistivity corresponds to smaller grain size, because the higher surface area of fine particles promotes transmission of electrical current (Biella and others, 1983; Kwader, 1985). Resistivity also is a function of porosity, where resistivity decreases proportionally to porosity based on the amount and quality of interconnected pore water (Archie, 1942). Although the wide variability of resistivity values in the Earth can provide valuable information about the subsurface, there are also significant ambiguities that can complicate the interpretation of resistivity data for development of a hydrogeologic framework (Minsley and others, 2010). As such, resistivity data alone can be challenging to interpret correctly, but when correlated with independent information such as geologic units on the surface and lithologic logs at depth, resistivity data can extend the understanding of subsurface geology to areas where other information is not available. More information regarding the electrical properties of rocks can be found in Keller (1987, 1989), Palacky (1987), Hearst and Nelson (1985), Hallenburg (1998), and Hearst and others (2000).

This chapter describes: (1) 79 TEM soundings collected in 12 groundwater basins located within the U.S. Army Fort Irwin National Training Center (NTC) study area (fig. 1; table 1); (2) TEM data, acquisition, calibration, and modeling; (3) comparisons of TEM data to borehole data, and comparisons and correlations between TEM model results within and between basins; and (4) summarizes the applications and limitations of the TEM method at the NTC. Examples of TEM models are provided to illustrate the insensitivity to the water table, evidence for faulting, sensitivity to basement, insensitivity to lava flows, and contrasts in model layer resistivity between soundings collected near wells of differing water production rate, as confirmed by aquifer tests. TEM data grouped into subbasins are displayed for Nelson Basin, where these data were critical to constraining the aerial extents of fault-bounded aquifers for hydrogeologic framework models.

Table 1. Location, elevation, and date of time-domain electromagnetic data collection in the Fort Irwin National Training Center study area, California, November 2010–January 2012.

[Elevation in feet above North American Vertical Datum of 1988 (NAVD 88) at transmitter-loop center. Root mean squared (RMS) of in-loop and out-of-loop data jointly inverted presented. Where the jointly inverted smooth model RMS exceeds 1.0, the RMS of the in-loop only inversion is presented. Model depth of investigation calculated during inversion (Christiansen and Auken, 2010) is displayed in feet below land surface at transmitter-loop center. ft, feet; --, no data; >, greater than value shown]

Basin	Sounding	Elevation (ft)	Latitude	Longitude	Date	Joint model RMS (smooth/ minimum)	In-loop model RMS (smooth/ minimum)	Depth of investigation (ft)
Goldstone	AU1	3179	35° 25' 27.459" N	116° 54' 28.163" W	Jan 2011	0.64/ 0.77		>1640
	AU2	3045	35° 23' 38.052" N	116° 53' 45.471" W	Jan 2011	0.46/ 0.55		>1640
	AU3	3041	35° 21' 49.290" N	116° 52' 45.497" W	Jan 2011	0.47/ 0.56		1515
Bicycle	BL1	2359	35° 16' 56.337" N	116° 39' 0.773" W	Dec 2010	0.74/ 0.8		>1640
	BL2	2356	35° 17' 11.244" N	116° 38' 28.047" W	Dec 2010	0.66/ 0.76		1280
	BL3	2356	35° 17' 31.111" N	116° 38' 2.226" W	Dec 2010	0.74/ 0.95		899
	BL4	2369	35° 17' 55.113" N	116° 37' 42.413" W	Dec 2010	0.51/ 0.77		1220
	BL5	2344	35° 17' 25.200" N	116° 37' 20.800" W	May 2011	--	1.01/ 1.15	265
	BL6	2346	35° 17' 6.800" N	116° 37' 28.000" W	May 2011	--	0.66/ 0.90	363
Central Corridor	CC1	2733	35° 22' 4.773" N	116° 37' 1.951" W	Jan 2011	0.51/ 0.66		1515
	CC2	2293	35° 21' 39.271" N	116° 31' 2.183" W	Jan 2011	1.20/ 1.49	0.68/ 0.60	344
	CC3	2349	35° 21' 50.260" N	116° 26' 14.613" W	Jan 2011	1.20/ 1.38	0.42/ 0.42	1099
	CC4	2517	35° 21' 36.100" N	116° 35' 32.000" W	May 2011	0.77/ 1.00		663
	CC5	2680	35° 22' 58.700" N	116° 26' 18.900" W	May 2011	0.82/ 1.20	0.66/ 0.66	1220
	CC6	2614	35° 20' 43.702" N	116° 37' 8.998" W	Jul 2011	0.57/ 0.68		1393
	CC7	2843	35° 22' 58.144" N	116° 34' 23.959" W	Jul 2011	1.14/ 1.39	0.97/ 1.22	1220
Cronise	CR1	1568	35° 15' 12.679" N	116° 24' 44.406" W	Jan 2011	0.75/ 0.89		1515
	CR2	1440	35° 14' 20.064" N	116° 28' 26.652" W	Jan 2011	0.71/ 0.82		1279
	CR3	1670	35° 11' 30.125" N	116° 28' 58.316" W	Jan 2011	0.49/ 0.57		>1640
	CR4	2110	35° 10' 27.986" N	116° 32' 49.844" W	Jan 2011	0.53/ 0.73		>1640
	CR5	1467	35° 15' 4.500" N	116° 25' 43.300" W	May 2011	0.55/ 0.65		1175
	CR6	1659	35° 10' 50.300" N	116° 27' 53.700" W	May 2011	0.38/ 0.46		1515
	CR7	1907	35° 11' 32.002" N	116° 32' 15.198" W	Jul 2011	0.51/ 0.62		1393
Drinkwater	DK1	3392	35° 29' 47.113" N	116° 35' 2.293" W	Jan 2011	1.25/ 1.46	0.73/ 0.87	427
	DK2	3337	35° 29' 38.483" N	116° 32' 51.646" W	Jan 2011	0.63/ 0.69		955
	DK3	3261	35° 27' 1.573" N	116° 30' 0.298" W	Jan 2011	0.49/ 0.46		974
Riggs	EG1	899	35° 22' 27.500" N	116° 12' 4.600" W	May 2011	7.26/ 8.60	0.31/ 0.40	886
Langford	LN1	2251	35° 10' 15.243" N	116° 37' 34.708" W	Nov 2010	0.41/0.54		>1640
	LN2	2395	35° 9' 31.976" N	116° 37' 27.926" W	Nov 2010	0.40/0.48		1515
	LN3	2513	35° 9' 2.215" N	116° 37' 21.401" W	Nov 2010	0.61/ 0.75		1515
Leach	LE1	2493	35° 39' 17.908" N	116° 42' 34.784" W	Nov 2010	--	0.75/ 0.81	986
	LE2	2408	35° 38' 31.122" N	116° 41' 50.020" W	Nov 2010	--	0.84/ 0.85	1077
	LE3	2178	35° 37' 41.035" N	116° 40' 58.762" W	Nov 2010	--	0.56/ 0.57	1515
	LE4	2021	35° 37' 48.060" N	116° 39' 17.431" W	Nov 2010	--	0.69/ 0.67	986
	LE5	1729	35° 38' 12.328" N	116° 37' 56.769" W	Nov 2010	--	0.85/ 0.86	284
	LE6	1480	35° 38' 23.558" N	116° 36' 54.171" W	Nov 2010	--	0.69/ 0.69	682
	LE7	1194	35° 38' 38.652" N	116° 35' 35.284" W	Nov 2010	--	0.53/ 0.55	902
Nelson	NL1	3248	35° 25' 51.814" N	116° 51' 13.277" W	Nov 2010	1.03/ 1.75	0.53/ 0.56	>1640
	NL2	3202	35° 30' 9.871" N	116° 45' 47.494" W	Nov 2010	0.69/ 0.94		>1640
	NL3	3084	35° 25' 37.653" N	116° 45' 39.405" W	Nov 2010	0.56/ 0.69		1279
	NL4	3150	35° 24' 29.784" N	116° 47' 43.465" W	Nov 2010	0.46/ 0.61		1280
	NL5	3219	35° 24' 11.122" N	116° 47' 50.205" W	Nov 2010	0.53/ 0.65		>1640
	NL6	3292	35° 26' 45.900" N	116° 48' 29.400" W	May 2011	0.50/ 0.60		1515
	NL7	3233	35° 25' 44.800" N	116° 43' 46.400" W	May 2011	0.96/ 1.16		1515
	NL8	3094	35° 25' 28.900" N	116° 41' 30.700" W	May 2011	1.03/ 1.08	0.40/ 0.51	1515
	NL9	3439	35° 28' 17.601" N	116° 53' 45.397" W	Jul 2011	0.81/ 0.99		1394
	NL10	3184	35° 28' 26.702" N	116° 47' 0.897" W	Jul 2011	0.47/ 0.56		1279

Basin	Sounding	Elevation (ft)	Latitude	Longitude	Date	Joint model RMS (smooth/ minimum)	In-loop model RMS (smooth/ minimum)	Depth of investigation (ft)
Nelson	NL11	3101	35° 26' 0.602" N	116° 47' 56.697" W	Oct 2011	0.54/ 0.65		>1640
	NL12	3390	35° 25' 0.103" N	116° 38' 10.798" W	Oct 2011	0.33/ 0.38		>1640
	NL13	2978	35° 23' 39.625" N	116° 41' 4.285" W	Oct 2011	0.41/ 0.49		1394
	NL14	3053	35° 24' 59.094" N	116° 42' 10.592" W	Oct 2011	0.61/ 0.70		>1640
	NL15	3181	35° 24' 27.289" N	116° 45' 6.234" W	Oct 2011	0.36/ 0.44		>1640
	NL16	3324	35° 26' 29.461" N	116° 50' 3.985" W	Oct 2011	0.57/ 0.67		>1640
	NL17	3302	35° 28' 2.501" N	116° 48' 20.631" W	Oct 2011	0.44/ 0.63		>1640
	NL18	3094	35° 28' 11.392" N	116° 45' 53.122" W	Oct 2011	0.47/ 0.58		>1640
	NL19	3407	35° 30' 39.643" N	116° 49' 3.883" W	Jan 2012	1.09/1.26	0.85/1.09	>1640
	NL20	3086	35° 25' 51.419" N	116° 47' 56.753" W	Jan 2012	1.07/1.28		>1640
	NL21	3064	35° 25' 25.014" N	116° 47' 28.742" W	Jan 2012	1.93/2.27	0.38/0.49	>1640
	NL22	3145	35° 25' 34.194" N	116° 48' 23.248" W	Jan 2012	1.25/1.44	0.48/0.67	>1640
	NL23	3211	35° 25' 42.508" N	116° 49' 7.845" W	Jan 2012	0.58/0.67		>1640
	NL24	3216	35° 25' 35.563" N	116° 49' 54.022" W	Jan 2012	0.63/0.75		>1640
	NL25	3207	35° 25' 30.884" N	116° 50' 38.369" W	Jan 2012	0.91/0.83		1515
	NL26	3223	35° 25' 7.573" N	116° 51' 1.176" W	Jan 2012	2.0/2.40		>1640
	NL27	3055	35° 25' 5.840" N	116° 47' 34.462" W	Jan 2012	1.10/ 1.28	0.74/ 0.83	>1640
	NL28	3170	35° 26' 29.065" N	116° 47' 51.464" W	Jan 2012	0.51/0.52		>1640
	NL29	3212	35° 26' 44.259" N	116° 47' 53.052" W	Jan 2012	1.33/1.72	1.21/ 1.34	>1640
	NL30	3130	35° 24' 32.751" N	116° 47' 46.521" W	Jan 2012	1.00/ 1.21		>1640
	NL31	3083	35° 24' 45.434" N	116° 48' 20.986" W	Jan 2012	1.21/1.36	0.60/0.84	>1640
	NL32	3135	35° 25' 17.645" N	116° 48' 27.055" W	Jan 2012	0.65/0.76		1220
Red Pass	RP1	3146	35° 26' 17.712" N	116° 22' 18.612" W	Jan 2011	1.06/ 1.15	0.85/ 0.65	>1640
	RP2	1808	35° 19' 13.707" N	116° 18' 58.587" W	Jan 2011	1.19/ 1.22	0.62/ 0.64	1515
	RP3	1755	35° 19' 4.320" N	116° 18' 7.025" W	Jan 2011	1.17/ 1.17	0.52/ 0.54	804
	RP4	2104	35° 21' 0.700" N	116° 20' 58.900" W	May 2011	0.72/ 0.74		974
Superior	SB1	3041	35° 16' 8.244" N	117° 5' 13.154" W	Dec 2010	0.39/ 0.43		951
	SB2	2999	35° 14' 57.398" N	117° 2' 32.595" W	Jan 2011	0.92/ 0.95		722
	SB3	3064	35° 15' 47.366" N	117° 3' 34.038" W	Jan 2011	0.57/ 0.96		1050
	SB4	3032	35° 16' 9.017" N	117° 1' 42.328" W	Jan 2011	0.61/ 0.64		328
Coyote	YO1	2438	35° 8' 40.935" N	116° 43' 10.452" W	Dec 2010	0.48/0.69		896
	YO2	2436	35° 9' 9.000" N	116° 44' 25.800" W	May 2011	--	0.54/ 0.85	570

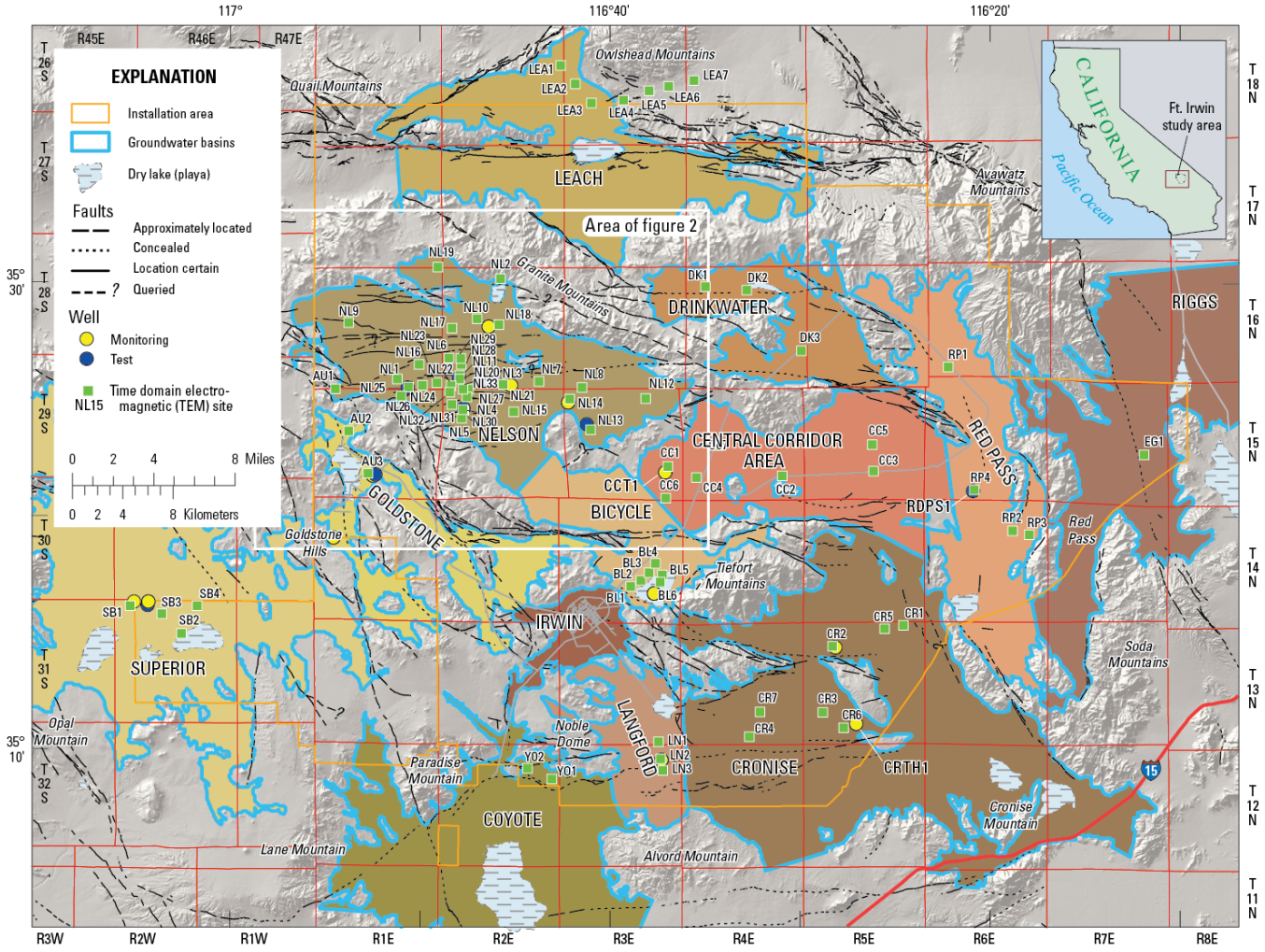

Figure 1. Map showing location of time-domain electromagnetic soundings and faults at Fort Irwin National Training Center, California.

Data Acquisition Methods

TEM is an inductive electromagnetic technique that provides a measure of near-surface resistivity by passing a current through a wire loop which, as explained by Ampere's law, generates a primary magnetic field. The primary current is rapidly turned off, thereby causing a time-varying change in magnetic flux, which induces voltages, and hence eddy currents in conductive bodies according to Faraday's law. In TEM, a secondary magnetic field is produced by the decay of these subsurface eddy currents, and the time derivative of this secondary magnetic field, d**B**/dt, commonly is measured as a voltage with time after primary current turnoff at one or more surface receivers. An apparent resistivity is calculated from the measured voltage at the receiver coil and the time elapsed after turnoff (Fitterman and Labson, 2005).

The apparent resistivity is solely a mathematical transform; however, it serves two important purposes. First, through its power law dependence on voltage and time, apparent resistivity accentuates

changes in the slope of the d**B**/dt curve associated with changes in subsurface conductivity. Second, the apparent resistivity is a proxy for true Earth resistivity, and in the case of a uniform half space, it is equal to the true resistivity at late times. The actual electrical resistivity distribution in the Earth is computed from the measured apparent resistivity through the process of inversion. Additional details on the TEM sounding method can be found in Christiansen and others (2011), Fitterman and Labson (2005), Danielsen and others (2003), and Nabighian and Macnae (1991).

TEM data were collected using a Geonics ProTEM system. All data were collected using a single 100- by 100- m square transmitter loop. All depths are reported in feet below sea level (bls). The depth of investigation (DOI) is dependent on subsurface resistivity as well as the signal-to-noise ratio and varies between sounding locations. DOI also scales with the transmitter moment (calculated from the number of transmitter wire turns times transmitter current times transmitter loop area) with a rule of thumb placing the DOI at 2–3 times the length of a side of the square transmitter loop; however, the DOI also was assessed qualitatively for all TEM sites by evaluating the sensitivity of an individual model parameter to the data (Christiansen and Auken, 2010). In this study, resolved depths were at least 265 ft with an average DOI of 1,289 ft. The maximum DOI of 1,640 ft was achieved at 28 locations (table 1).

At all locations, data were collected in a central-loop configuration where the receiver coil was placed at the center of the transmitter loop (normal to the midpoint of each transmitter loop edge). Additional data were collected at a single location outside of the transmitter loop at a distance of 50 m normal to the midpoint of the nearest transmitter loop edge. Out-of-loop data are recorded as the time derivative of the secondary magnetic field (that is, d**B**/dt, where **B** is the magnetic induction). Out-of-loop data were used as a qualitative check on the assumption of one-dimensionality (layer-cake Earth structure) required for subsequent modeling and inversion. Out-of-loop data also were modeled and inverted jointly with the central-loop data to better constrain the final resistivity models.

Calibration of a TEM system is essential to an accurate recovery of near-surface resistivity structure (Christiansen and others, 2011). Calibration, in this context, involves the characterization of system filters, the knowledge of system geometry, measurement of the transmitted waveform, assessment of system bias, and correction for timing and normalization errors for a particular combination of instrument components (data logger, transmitter, and receiver). The ProTEM system used in this study was calibrated in 2009 and again in 2011 at an established test site at Lyngby, Denmark (Geological Institute, 2002a, 2002b).

Data were collected at a range of repetition frequencies using a combination of high-frequency (Geonics HF Coil) and low-frequency (Geonics 3D-3LF Coil) receivers together with low-current (Geonics ProTEM 47) and high-current (Geonics ProTEM 57) transmitters. With the high frequency receiver/low current transmitter configuration, data were collected at 285, 75, and 30 hertz (Hz). For the low frequency receiver/high current transmitter configuration data were collected at 30, 7.5, and 3 Hz. Average current was 2.5 and 10.0 amperes (A) for the low- and high-current transmitters respectively, giving rise to an average transmitter moment of 25,000 ampere-square meter (A-m^2) for the low frequency receiver and 85,000 A-m^2 for the high frequency receiver. All data were collected with induction coil receivers, with moments of 31.4 A-m^2 and 200 A-m^2 for the high- and low-frequency coils, respectively. During each transient decay, data were sampled at 20 logarithmically spaced time gates from 6 microseconds (μs) to 6 milliseconds (ms) after turn-off of the transmitter current. At each repetition frequency, individual voltage decay curves, corresponding to a single current pulse, were averaged over a time interval between 4 and 15 seconds. A minimum of 20 such readings were made to permit robust error calculation. Background noise measurements also were made with each receiver at

each station by acquiring data with the transmitter turned off. Such noise measurements are used during processing to determine the time at which actual data fall below the measured noise envelope.

Data Analysis and Modeling

Data analysis for all soundings consisted of data format conversion, statistical analysis and averaging, forward modeling, data inversion, and model assessment. Data were processed and inverted using the SiTEM data processing and Single-Site Electromagnetics Data Inversion (SEMDI) software packages (Auken and Nebel, 2001), which permit full waveform specification, the modeling of system filters, the incorporation of data errors and reported error bounds on inverted parameters (layer thicknesses and resistivities). For a detailed discussion on TEM noise and inversion calculation of root-mean-squared (RMS) errors in the SiTEM program refer to Effersø and others (1999).

Data were inverted for two end-member model classes: (1) minimum-layer models, and (2) 20-layer, smooth or Occam-style, inverse models (Constable and others, 1987). The former approach seeks to fit the data with as few distinct layers as possible, as defined by the geophysicist processing the data. The latter approach seeks to fit the data with a large number of thin layers of fixed thickness under the constraint that the resistivity varies slowly between adjacent layers. Minimum-layer models are more appropriate in settings where abrupt changes in resistivity are expected (for example, an unconformity, a volcanic flow boundary, or a water table), whereas smooth inverse models are more realistic when gradual changes are expected (for example, changes in grain size or clay content). Independent information from geologic mapping, borehole lithology, and geophysical borehole logs was used to assess which of the previously described model classes may be more appropriate in interpreting subsurface structure.

The modeling and inversion of TEM data are commonly one-dimensional analyses. The 1D assumption is reasonable for this study given the (1) nature of the regional geology, that is, a relatively simple stratigraphy that can be approximated by horizontal beds and associated electrical properties, (2) compact footprint of the TEM method, and (3) limited depth of investigation (not more than 1,640 ft). Lithologic and stratigraphic logs from nearby boreholes (Adam Kjos, U.S. Geological Survey, written commun., 2012) were used to confirm or reject lateral correlation between soundings. Joint inversion of the in- and out-of-loop data are mostly consistent with a 1D subsurface resistivity structure. Where smooth models of joint inversion data had a RMS < 1.0, the 1D models were assumed to be representative of the subsurface. Where smooth models of joint inversion data exceed an RMS > 1.0, additional degrees of subsurface dimensionality are required to resolve the data. These relatively high errors are assumed to be a system response to a subsurface electrical discontinuity (either a fault, or depositional feature) (Hobza and others, 2011).

To assess the DOI of each inverse model, we apply the sensitivity-based approach of Christiansen and Auken (2010). Column-wise sums of the Jacobian, or sensitivity matrix, provide an estimate of the mean sensitivity of an individual model parameter to the data. Calculating a cumulative sum of these sensitivities, starting from the bottom of the model, gives an impression of how data sensitivity is built up within the model. A threshold value, here equal to 0.8, is used to define the DOI, which can be interpreted as the depth below which the data have little or no influence on the model. The choice of threshold value is subjective, hence the DOI value should be considered in a relative, rather than absolute sense.

In the application of inverse theory to geophysics, inverse models, including TEM models, exhibit a degree of non-uniqueness (Aster and others, 2005). Thus, for any measured dataset, typically, a range of models can be determined that adequately fit the data. As such, available ground-truth from

borehole logs was needed to accurately model TEM data and constrain interpretations. For most electrical methods, equivalence exists between models with equal conductance (depth-integrated conductivity). Thus, for example, a model with a 164-ft thick, 10 ohm-m layer produces nearly identical measured data as a 33-ft thick layer with a resistivity of 2 ohm-m. Additionally, the TEM method has difficulty resolving resistive layers because of the low current densities induced within them as compared to conductive layers.

TEM Survey Results

TEM Models

Locations of soundings in Nelson and Goldstone Basins are shown in figure 2; all other TEM sounding locations are shown in figure 1. An example TEM sounding curve and model, Nelson Basin sounding 11 (NL11), is shown in figure 3. All other TEM sounding curves and models (appendix A, figs. A1–A39) are located at the end of this chapter. At each station, the left panel of the figure (*A*) shows the sounding curves of central-loop data plotted as apparent resistivity in ohm-m against time for each repetition frequency at which data were collected. The right panel of the figure (*B*) shows the best-fit minimum-layer (red) and smooth (blue) inverse models. In most cases, the model response of the jointly inverted in- and out-of-loop data meets the error threshold established for data quality (RMS ≤ 1.0). For these models, the out-of-loop data are plotted as the time derivative (d**B**/dt) in volts per square meter along with the central loop data in the left panel. The out-of-loop data are always the upper-right of the two curves presented in the left panel. Where jointly inverted in- and out-of-loop smooth models exceeded the error threshold, only the central-loop data are presented in the left panel.

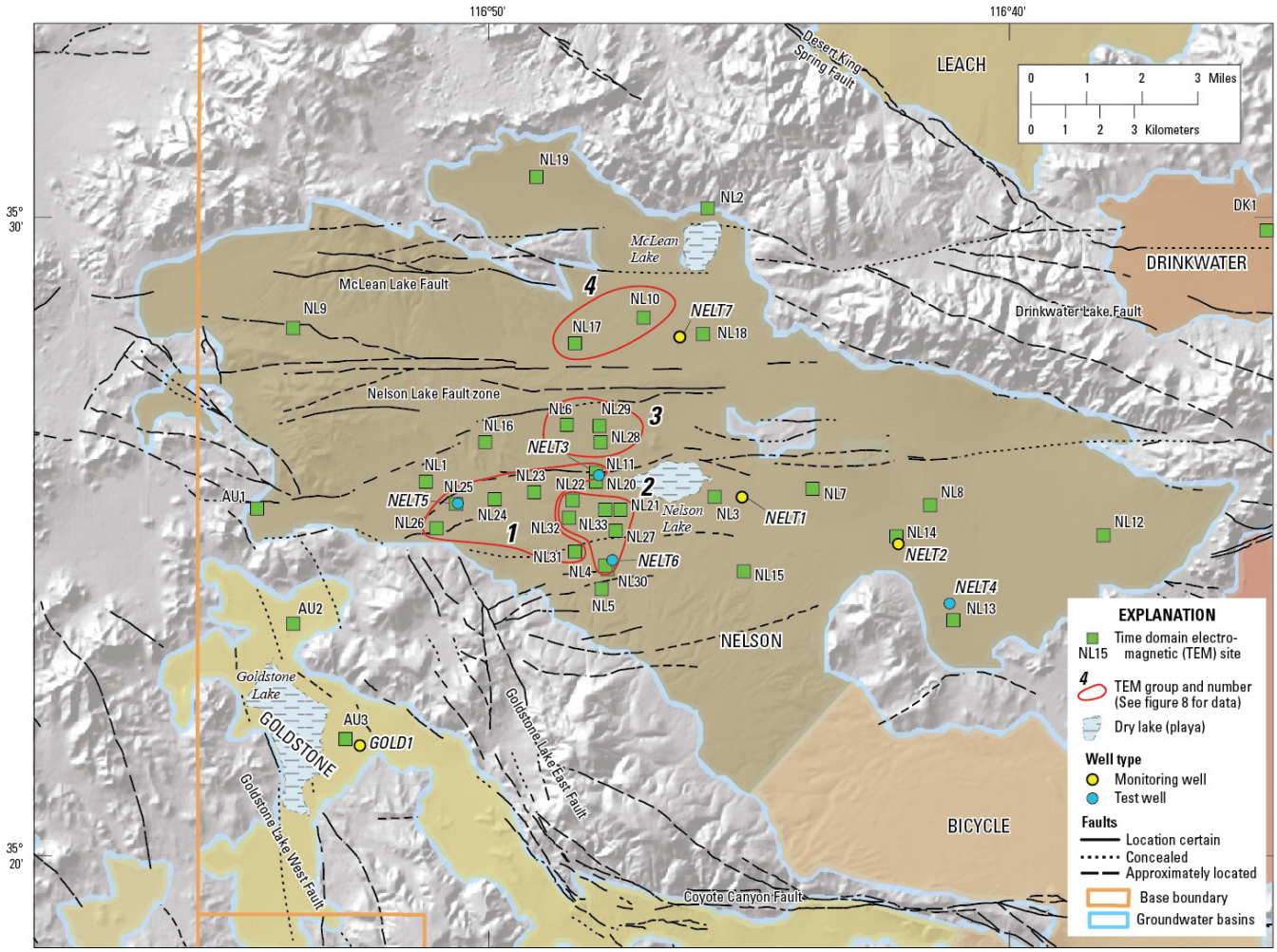

Figure 2. Index map showing TEM sites, wells, and faults in Nelson and Goldstone Basins, Fort Irwin National Training Center, California. Subbasins as defined by TEM sounding curves are delineated in red.

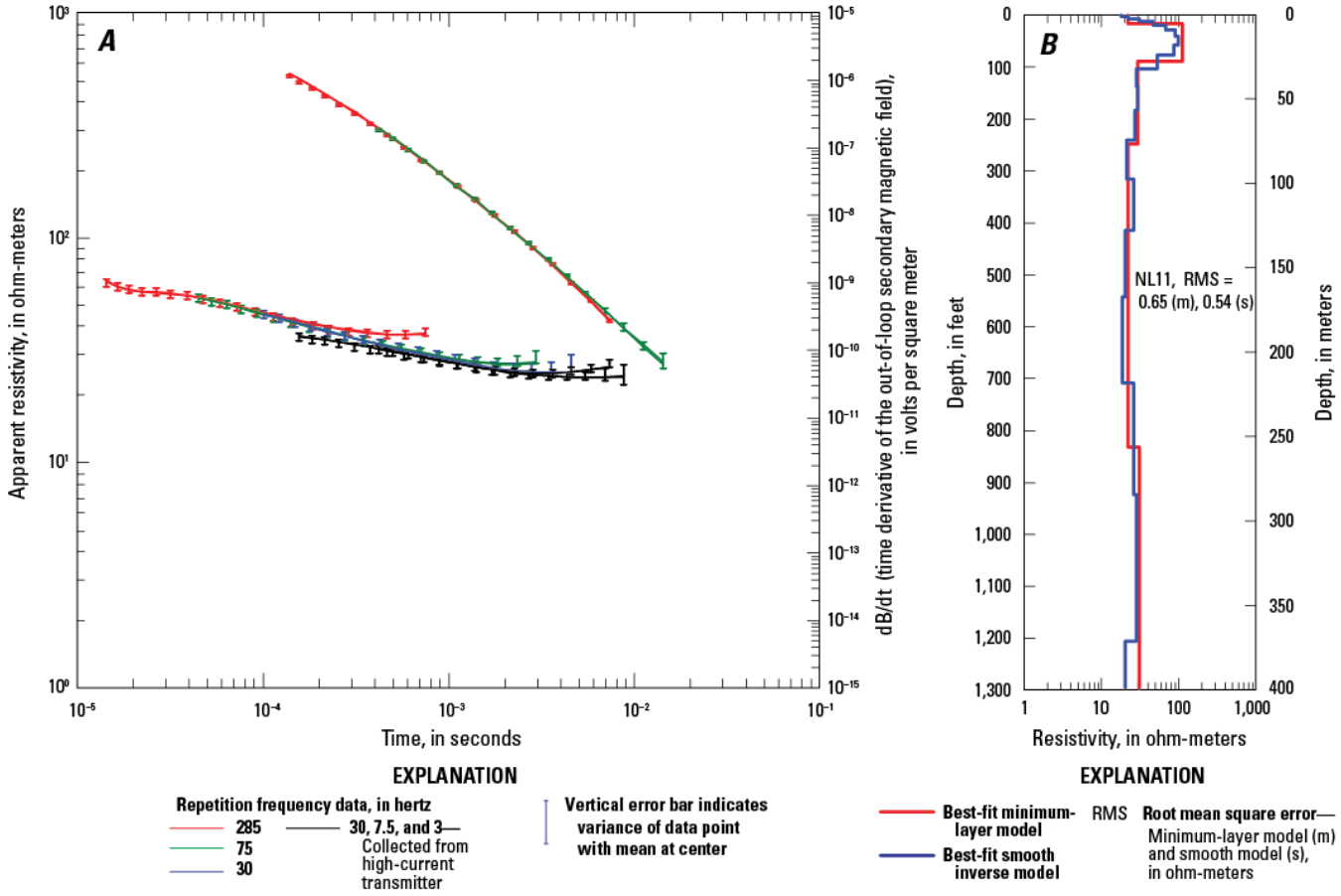

Figure 3. Graphs showing relations between *A*, central-loop resistivity (lower left curve, left axis), out-of-loop vertical magnetic field (time-derivative, upper right curve, right axis), and time; *B*, depth below land surface and subsurface resistivity modeled from TEM sounding for site NL11, Fort Irwin National Training Center, California.

TEM Model Uncertainty

TEM models fit the measured data with RMS < 1 at 52 of the 79 sounding locations. The RMS error for all soundings collected for this report are indicated in table 1 and on each model figure (appendix A, figs. A1–A39, panel *B*). The RMS error was usually slightly larger for the minimum-layer models, than for the smooth models, reflecting the greater difficulty in fitting the data with a smaller number of model parameters. However, RMS errors generally were similar for the smooth and minimum-layer models, suggesting that the minimum-layer parameterization can adequately represent the subsurface resistivity structure, and by inference, the stratigraphy. When processing minimum-layer models, the standard deviation for each model parameter (resistivity, depth and layer thickness) was considered along with the RMS error for each model fit. This provided the ability to quantitatively assess, at each site, which parameter the data were most sensitive to when considering various models. The minimum-layer model approach is consistent with the known geologic history of the area, including a number of unconformities associated with tectonically controlled changes to sediment input, erosion, and sediment source from non-volcanic to syn-volcanic sources and can be based on borehole data.

In contrast, the smooth models, which only vary in resistivity at fixed depths, cannot incorporate any conceptual understanding of the subsurface and is purely a mathematical best fit based on the inverse model. The smooth models can be used to develop and improve minimum-layer model fits to the data. Neither model type is preferred and both model types provide important information, as both are valid representations of the data presuming the RMS is within tolerance.

TEM Model Interpretation

In the groundwater basins on the NTC, the data generally supported 3- to5-layer TEM models for resistivity stratigraphy. These minimum-layer models, as well as the smooth models, compare favorably in magnitude and character to the 64-inch, long-normal, borehole resistivity logs, especially where boreholes and TEM sounding are located less than 3 km apart. In this study, distances between TEM soundings and the nearest borehole location within the same groundwater basin range from 135 m to 9.8 km; therefore, differences in land-surface elevation, as well as lateral variations in lithologic, hydrogeologic, and electrical properties within lithologic units, and in the orientation (strikes and dips) of lithologic units may cause uncertainties in the comparability of TEM and borehole data with increasing separation distance. In Coyote Basin, Drinkwater Basin, and eastern Red Pass, there are no borehole data to compare with TEM data. Correlation of TEM soundings to other datasets may also be complicated by unmapped faults, where the offset of lithologies is unknown between adjacent soundings and/ or boreholes.

In most TEM models (excluding soundings collected on Bicycle Lake playa [BL5 and BL6] or those above shallow bedrock), there are one or two more or less resistive layers (which generally range from 50 to 300 ohm-m, but are as low as 30 ohm-m in a few models) from the near surface to as deep as about 328 ft, and these layers overlie a thick, lower resistivity layer (less than 40 ohm-m) (figs. 4, 5, and 6). In some models, there is a thin, lower resistivity unit (20–40 ohm-m) in the upper 20–50 ft below land surface. This near-surface resistivity low is interpreted to represent unsaturated zone moisture held by lithostratigraphic-controlled, matric potential forces within the upper-most lithologic unit. Where soundings are adjacent to boreholes, the depths of model layers generally correlate to lithologic changes identified in borehole cuttings and resistivity logs. In a few locations in Nelson Basin (NL20, NL11), where sounding loop centers were less than 200 m from the NELT3 (16N/02E-31H1S) borehole, TEM data could be modeled to fit the water-table depth measured in the well; however, the fit of the model fixed to the water-table depth resulted in a higher RMS than an unconstrained TEM model and was therefore not presented here with the best-fit models.

Because the uncertainty of the individual model parameters can be estimated, changes to each parameter can be evaluated as TEM data are modeled to fit boundaries observed in lithologic or geophysical logs. Thus, it is possible to determine if models are more sensitive to changes in resistivity, thickness, or depth.

TEM-Borehole and TEM-TEM Comparisons

Four examples are presented in the following sections that demonstrate seven different facets of TEM model interpretation: (1) variations between borehole resistivity logs and TEM models; (2) variations between nearby TEM profiles; (3) insensitivity to the water table; (4) evidence for faulting; (5) insensitivity to lava flows; (6) contrasts in model layer resistivities compared to wells of differing transmissivity as confirmed by aquifer tests; and (7) model sensitivity to crystalline basement.

Variations between Borehole Resistivity Logs and TEM Models, Variations between Nearby TEM Profiles, Evidence for Faulting and Model Insensitivity to the Water Table

In west-central Nelson Basin (fig. 4), borehole NELT3 and TEM soundings NL11 and NL20 provide insights regarding the correlations of lithologic features between TEM models; illustrate the insensitivity to the water table in both borehole resistivity and TEM data and boreholes; as well as contrasts resistivity profiles across a fault. Each of these data points are roughly north–south to each other. NELT3 and NL20 are approximately 150 m apart and are on the south side of a mapped fault, whereas NL11 is 135 m north of NELT3 and north of the fault.

There is a decrease in resistivity in the NL20 TEM models—from 255 to 41 ohm-m at an elevation of 2,970 ft in the minimum-layer model and from 83 to 36 ohm-m at an elevation of 2,946 ft in the smooth model (fig. 4). These changes in TEM model resistivity roughly correlate (differences of 22 and 46 ft) to a distinct decrease in resistivity values in the 64-inch, long-normal borehole resistivity log at an elevation of 2,992 ft (Unpublished data). This change in borehole resistivity correlates well with a contact between (1) several lithologic features in the near-surface rocks to an elevation of 2,987 ft that are consistent with the rocks being part of the possible Quaternary or Pliocene sequence, and (2) the rocks from 2,987 ft and deeper being part of the possible Miocene sequence (D. Buesch, written commun., 2012) (fig. 4). Water levels measured in Nelson Basin are below the high resistivity (>40 ohm-m) section of the possible Quaternary/Pliocene unit seen in borehole resistivity logs. This establishes that the depth of the initial decrease in resistivity in TEM models in west-central Nelson Basin represents a minimum thickness of the unsaturated zone based on the high resistivity of the unsaturated, possible Pliocene/Quaternary section.

The NL20 and NL11 TEM models are similar in character, except the sharp decrease in resistivity values are offset by approximately 55 ft, with the NL20 minimum-layer model resistivity decrease occurring at an elevation of 3,011 ft and the smooth layer models decrease in resistivity at 2,998 ft. Although the NL11 models agree better with elevation of the contact in the borehole resistivity data than NL20, the 55-ft offset between NL20 and NL11 illustrates the apparent down-to-the-south separation of the lithologic units or variations in lithologic unit thickness associated with an offset across the fault.

Although the possible Miocene is the water-bearing unit in western Nelson Basin, there is no change within this unit in the resistivity of the borehole resistivity log nor the TEM models at the static water level in borehole NELT3 (elevation 2,879 ft) (Joseph Nawikas, U.S. Geological Survey, written commun., 2012). A screened section of NELT3 at an elevation of 2,726–2,626 ft (360–460 ft bls) is within the possible Miocene unit. The estimated transmissivity on this screened interval, calculated from aquifer tests, is 1,552 feet squared per day (ft^2/d) (Joseph Nawikas, U.S. Geological Survey, written commun., 2012). This correlation of model layer resistivity to hydrologic data establishes that in western Nelson Basin (and possibly elsewhere in the region), TEM model layers with resistivity values between 35 and 20 ohm-m, located beneath a higher resistivity near-surface unit, are good targets for productive aquifers.

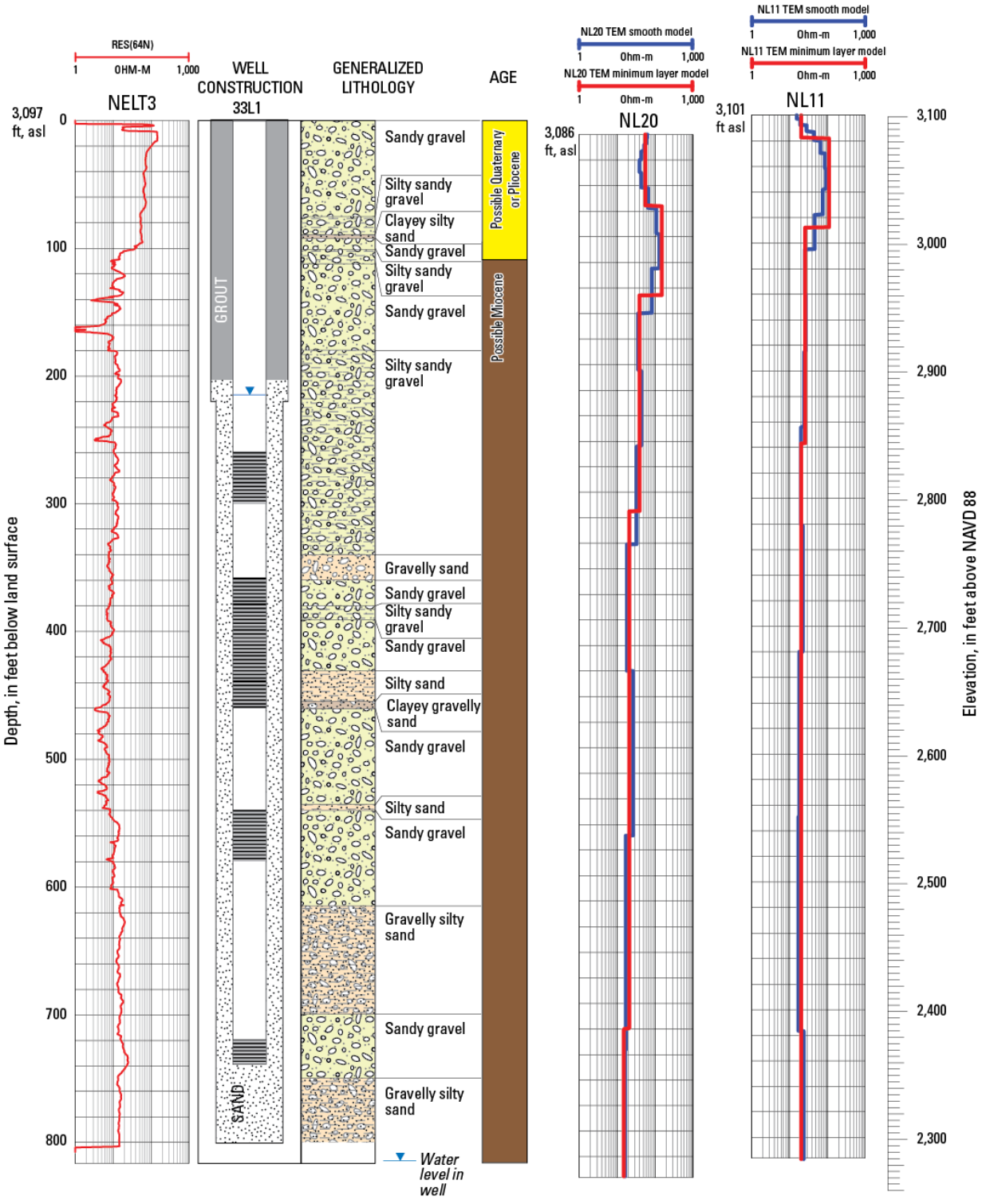

Figure 4. Resistivity and lithologic data from borehole NELT3 and TEM soundings NL20 and NL11 in Nelson Basin (fig. 2), Fort Irwin National Training Center, California. Elevation scale on right applies to all data in this figure. Depth scale on left applies to borehole NELT3 data only. In the well construction diagram, screened intervals are indicated as horizontally hatched gray areas. Geologic ages assigned to the stratigraphic column are from D. Buesch (written commun., 2012).

Insensitivity to Thick Lava Flows and Resistivity Correlation to High Transmissivity Unit

In Goldstone, Cronise, and Superior Basins, TEM data were collected near where lava flows are known to occur from well data. These buried volcanic rocks produced high resistivity spikes in the borehole resistivity data, but were not resolved in the TEM data. In Goldstone Basin, within borehole GOLD1 (15N/01E-28R1-3S; elevation 3,058 ft) a 124-ft thick (294–418 ft), fractured crystallized volcanic section in GOLD1 is interpreted as a dacite lava flow or an avalanche breccia (D. Buesch, written commun., 2012). A 20-ft thick interval within this section, screened from 350 to 370 ft has an estimated transmissivity, calculated from slug test data, of 3,328 ft^2/d (Joseph Nawikas, U.S. Geological Survey, written commun., 2012). This is one of the most productive water producing intervals in the NTC study area. This dacite section correlates to an *increase* in resistivity of more than 10 ohm-m in the borehole resistivity logs.

GOLD1 is approximately 500 m at a bearing of 108 degrees from TEM sounding AU3 (elevation 3,041 ft), and the TEM models correlate in general character and magnitude to the borehole resistivity log (fig. 5). There is a moderate *decrease* in resistivity from 27 to 22 ohm-m about 50 ft above the dacite section, but the dacite section itself is not resolved in the TEM data. The TEM model does not distinguish the resistive layer nested within a lower resistivity layer, which is an inherent limitation of the method. However, the minimum-layer model resistivities below the water table are similar to those seen in productive units in Nelson Basin (fig. 4), further establishing the target for a productive unit to have a resistivity between 35 and 20 ohm-m and to be located beneath a higher resistivity near-surface unit.

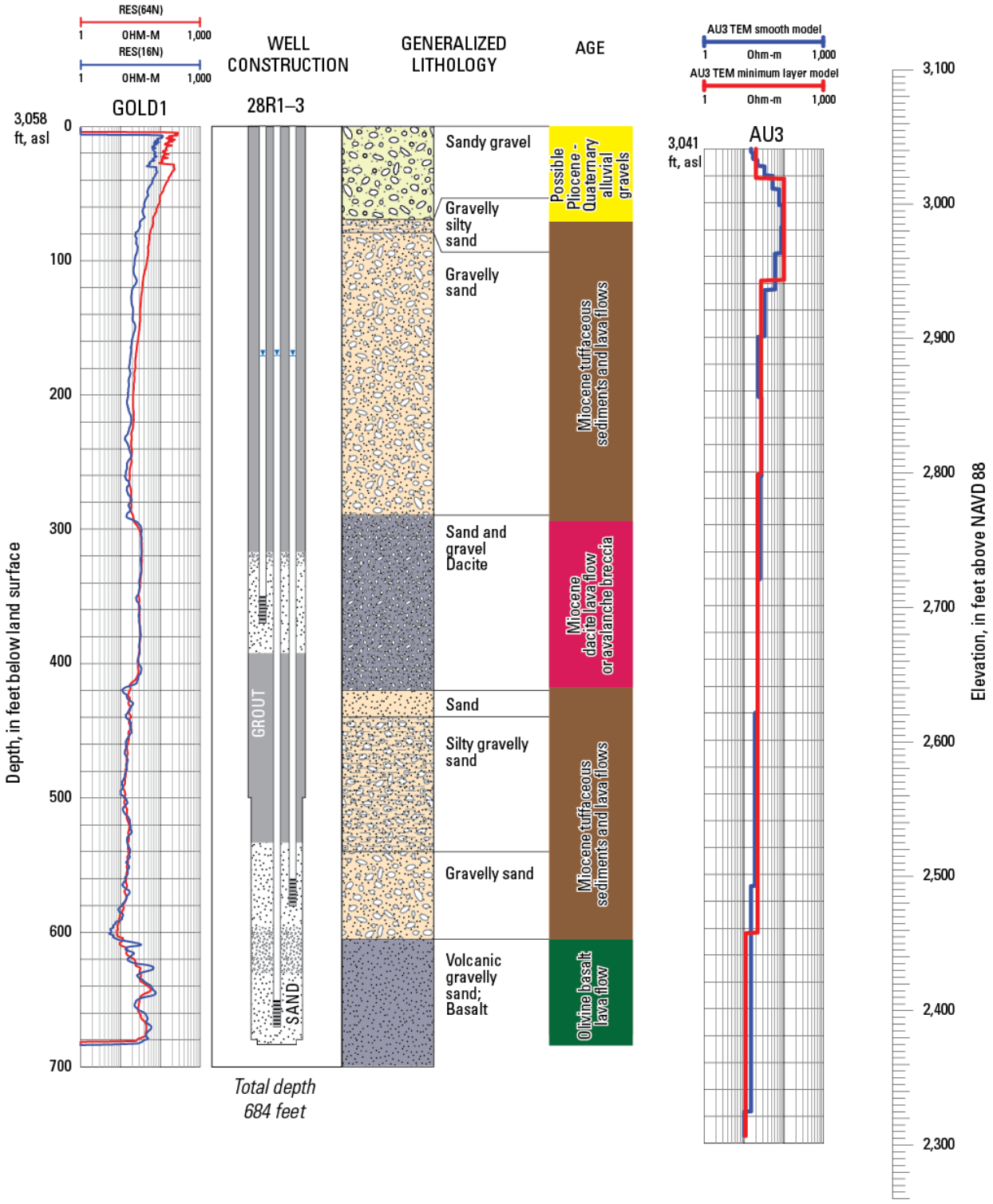

Figure 5. Resistivity and lithologic data from borehole GOLD1 and TEM sounding AU3 in Goldstone Basin, Fort Irwin National Training Center, California. Elevation scale on right applies to all data in this figure. Depth scale on left applies to borehole GOLD1 data only. In the well construction diagram, screened intervals are indicated as horizontally hatched gray areas. Geologic ages assigned to the stratigraphic column are from D. Buesch (written commun., 2012).

Insensitivity to Thin Lava Flows and Resistivity Correlation to Low Transmissivity Unit

In Cronise Basin, the TEM sounding CR6 (elevation 1,659 ft) is best fit by a 4-layer minimum layer model (fig. 6). The TEM sounding CR6 is 1.1 km at a bearing of 287 degrees from CRTH1 (fig. 1, 13N/05E-28Q1-3S, elevation 1,577 ft); the model from this sounding did not resolve the water table at 1,417 ft (160 ft bls) nor the lava flow, which produced an increase in the borehole resistivity log from 1,337 to 1,322 ft (240–255 ft bls) (fig. 6). Above the basalt, there is a marked decrease in borehole resistivity from 40 to 10 ohm-m over 80 ft (elevation 1,477–1,397 ft, [182–262 ft bls]) that correlates to a change in lithology to finer grained sediments (Kjos and others, 2013). Coincidently, the water table of the well screened within this upper unit occurs at 1,418 ft (159 ft bls). The upper 260 ft of the minimum-layer TEM model is expressed as two model layers. The TEM model shows only a single decrease in resistivity from the land surface to a depth of about 270 ft, presumably below the resistive basalt. In this instance, the smooth TEM model detects some variation in resistivity observed in the borehole log above the basalt. There is a decrease from 52 to 16 ohm-m in the smooth model at an elevation of 1,418 ft (222 ft bls) that correlates to the elevation of the water table in CRTH1 (fig. 6). A second decrease in resistivity (to 6 ohm-m) occurs in the smooth model, presumably below the basalt in CRTH1 at an elevation of 1,339 ft (320 ft bls). The thick section of low-resistivity (<10 ohm-m) values in the TEM models are similar in character and magnitude to the generally low-resistivity values of the borehole geophysical log.

The low-resistivity layers beneath the lava flow in CRTH1 correlate to a fine-grained, lower water-bearing unit. Transmissivity values calculated from slug tests conducted in wells screened within this lower water-bearing unit in CRTH1 are approximately 100 ft^2/d (Joseph Nawikas, U.S. Geological Survey, written commun., 2012). These transmissivity values are in contrast to transmissivity values from the water-bearing unit in Nelson Basin (1,552 ft^2/d), which have an average resistivity of 22.6 ohm-m. The rocks correlative to resistivity values less than 20 ohm-m in TEM models have been shown through comparison to CRTH1 to be generally too fine-grained to viably produce water. This correlation is further supported by data from Red Pass (appendix A, figs. A36 and A37) and Central Corridor (appendix A, figs. A5 and A6) where less than 20 ohm-m model layers in TEM soundings can be correlated to fine grained units in boreholes RDPS1 and CCT1 (fig. 1; Adam Kjos, U.S. Geological Survey, written commun., 2012). The contrast between values in saturated lower sections can be extended to evaluate other TEM models where borehole control is not available to evaluate an area's potential to produce economically feasible quantities of water. It would not have been possible to develop such a tolerance prior to borehole installation and aquifer testing. Anecdotally, because of the prevalence of TEM model layers between 10 and 20 ohm-m in the eastern half of the base, during the initial stages of exploration, these layers were optimistically interpreted as being potentially water bearing.

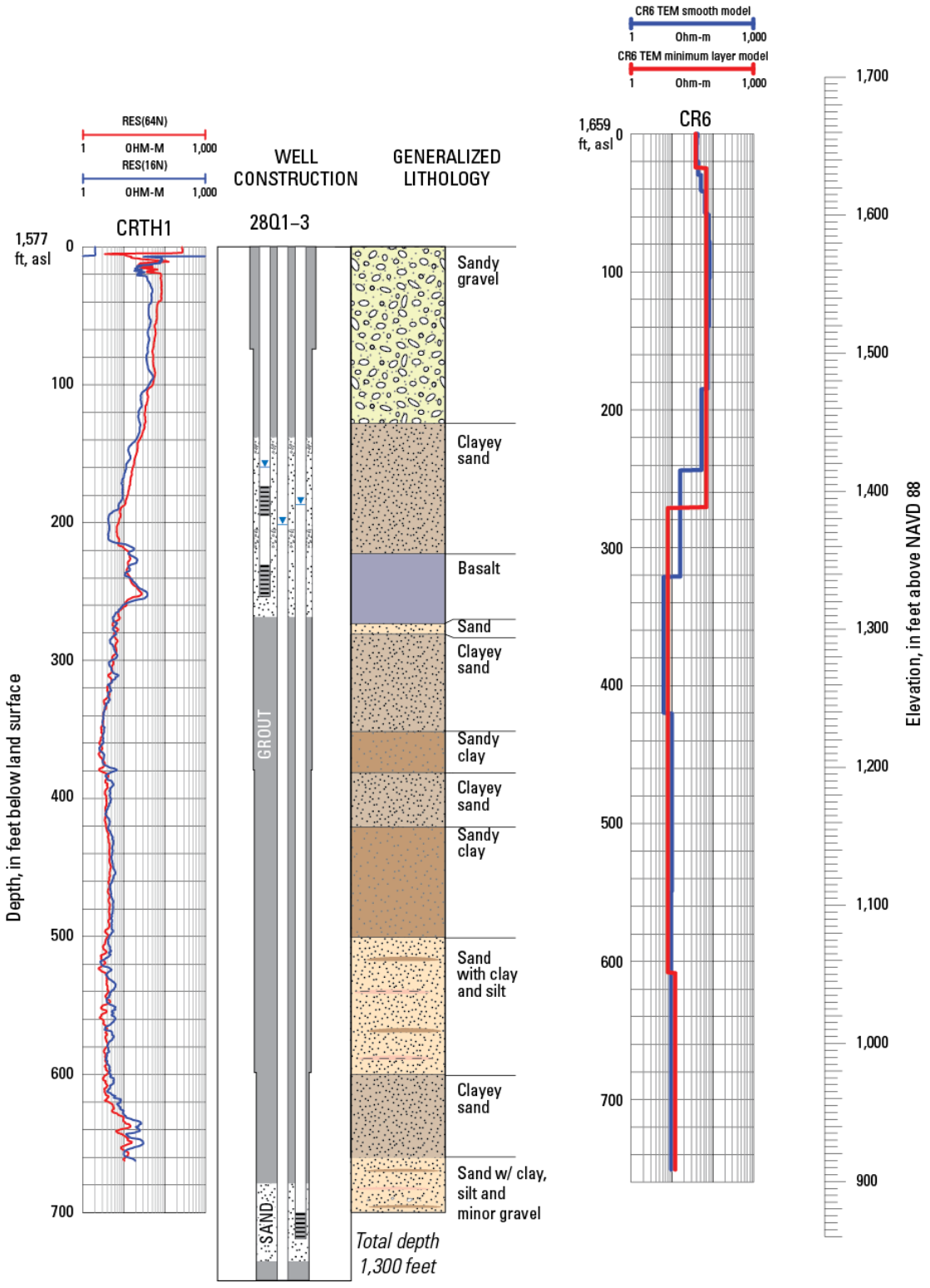

Figure 6. Resistivity and lithologic data from CRTH1 and TEM sounding CR6 in Cronise Basin, Fort Irwin National Training Center, California. Elevation scale on right applies to all data in this figure. Depth scale on left applies to borehole CRTH1 data only. In the well construction diagram, screened intervals are indicated as horizontally hatched gray areas.

Sensitivity to Basement

Because the DOI is dependent on the signal strength, which is in part a function of the signal-to-noise ratio, the low-electrical noise environment of the NTC allows for a great depth of investigation using TEM. In this setting, models typically are valid to at least depths of between 1,312 and 1,640 ft, resulting in the potential to detect bedrock at less than these depths. Highly resistive layers (>500 ohm-m) were detected beneath four TEM soundings (DK1, DK3, CC2, and YO2) (fig. 7*A*, fig. 1). These soundings, collected near the margins of the basin or in shallow basins as indicated by gravity data, are interpreted as shallow bedrock. These depths to bedrock, inferred from TEM models, are consistent with the depths to bedrock obtained from gravity data (Jachens and Langenheim, this volume, chap. H). Another five sounding locations (DK2, RP2, RP3, NL12, and CC7) (fig. 7*B*, fig. 1) from other basin margins that display deep layers with resistivity greater than 100 ohm-m are also inferred to correlate to bedrock depths obtained from gravity data (Jachens and Langenheim, this volume, chap. H). With the exception of RP2, these layers occur below thick, low-resistivity layers. In these locations, low-resistivity units above the bedrock may be absorbing the secondary magnetic field (the Earth's response to the primary magnetic field generated by the turn-on of the TEM system), thereby diminishing the apparent resistivity of the bedrock.

Although not included in figure 7, sounding NL13 (appendix A, fig. A25) was collected near borehole NELT4 (fig. 2), which penetrated a gneissic bedrock at a depth of 840 ft (Kjos and others, 2013). A gneiss-clast-rich sediment was penetrated at a depth of 777 ft. The NL13 sounding curve is characterized by a positively sloped curve (increasing apparent resistivity) for later gates in the 75–3 Hz data, indicating an increase in resistivity at depth. The minimum-layer model is best fit by a four-layer solution, which models the section beneath a depth of 300 ft as a single 30 ohm-m layer. The smooth model increases in resistivity from approximately 10 ohm-m at a depth of 250 ft to approximately 40 ohm-m at a depth of 425 ft. Below this maximum resistivity value, the model decreases in resistivity to slightly less than 30 ohm-m at a depth of 700 ft before increasing again to 40 ohm-m at a depth of 1,200 ft. Although a strong resistor is not modeled at the depth measured in the borehole, the models reflect a generally resistive section beneath a low-resistivity unit (approximately 10 ohm-m) from 100 to 300 ft in the minimum-layer model. These results reinforce the assertion that low-resistivity units above the bedrock may be absorbing the secondary magnetic field and reducing the apparent resistivity of the bedrock in the other soundings collected near the margins of basins.

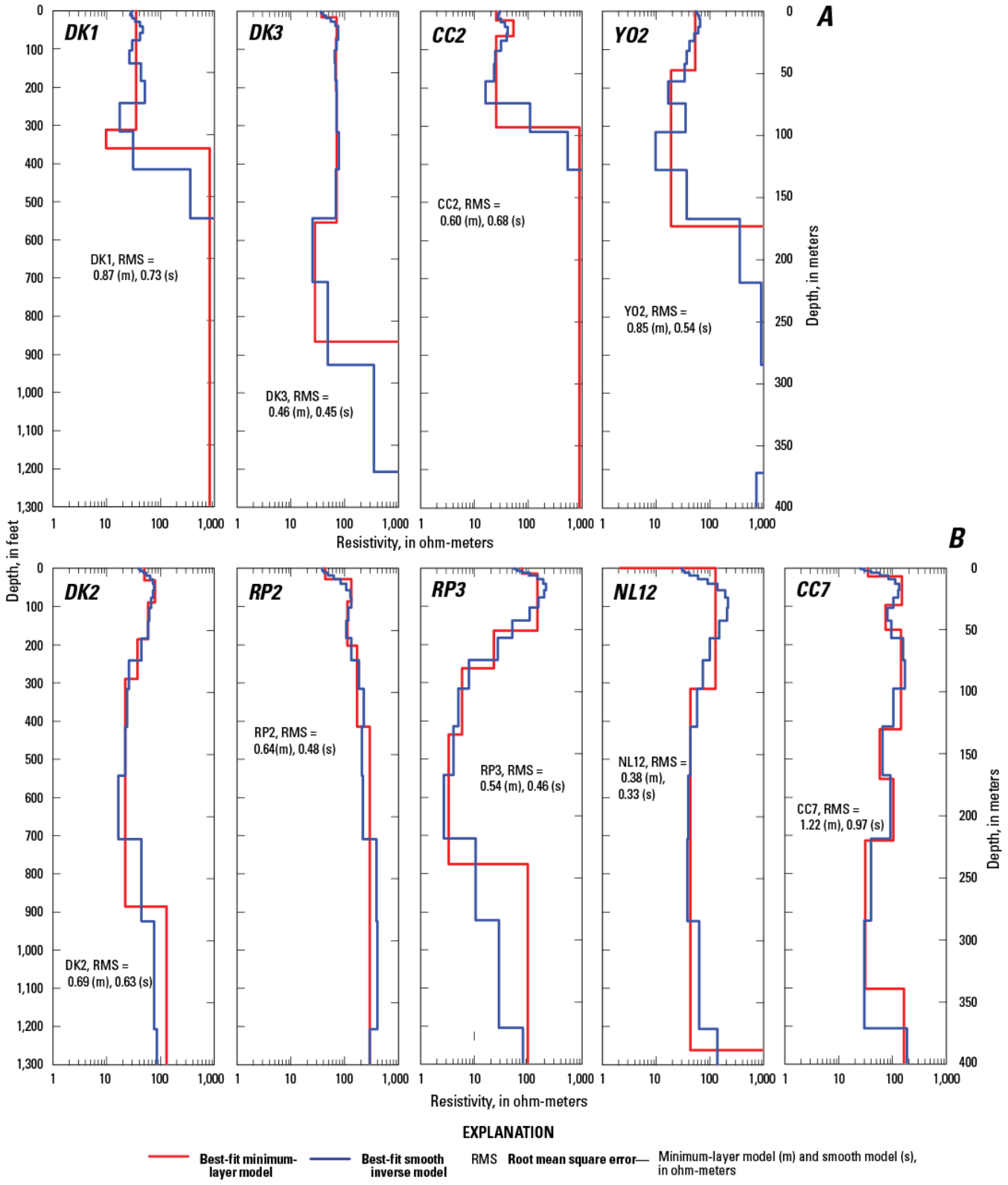

Figure 7. TEM models illustrating method sensitivity to basement less than 1,300 ft below land surface. *A*, Models with model layers greater than 500 ohm-m interpreted as bedrock. *B*, Models with model layers greater than 100 ohm-m interpreted as bedrock.

Compartmentalization of Nelson Basin based on TEM Models

By comparing the apparent resistivity vs. time plots for models from Nelson Basin, a clear grouping of sites can be made. By analyzing the shape of the data curves (fig. 8), issues created by the fitting of data to various models (that is, model RMS, parameter standard deviation, model layer elevations and resistivities of non-unique solutions, and differing land-surface elevations) are removed because the evaluation of the data is based on similarity of curves at different sites. When these grouped sites are analyzed in a spatial context (fig. 2), insight is provided to the compartmentalization of the basin not available from other methods, including geologic mapping and gravity. These subbasins within the larger Nelson Basin potentially limit the availability of water that can be withdrawn because of a reduced total storage of the aquifers. Thus, short of conducting a much more expensive airborne electromagnetic (AEM) survey (P. Bedrosian, written commun., 2012), an ensemble of TEM profiles helps to approximately locate subbasins and prioritize locations for additional investigations to identify faults that serve as barriers to groundwater flow. These data provide critical inputs for developing a hydrogeologic framework model for quantifying total groundwater availability and modeling groundwater flow.

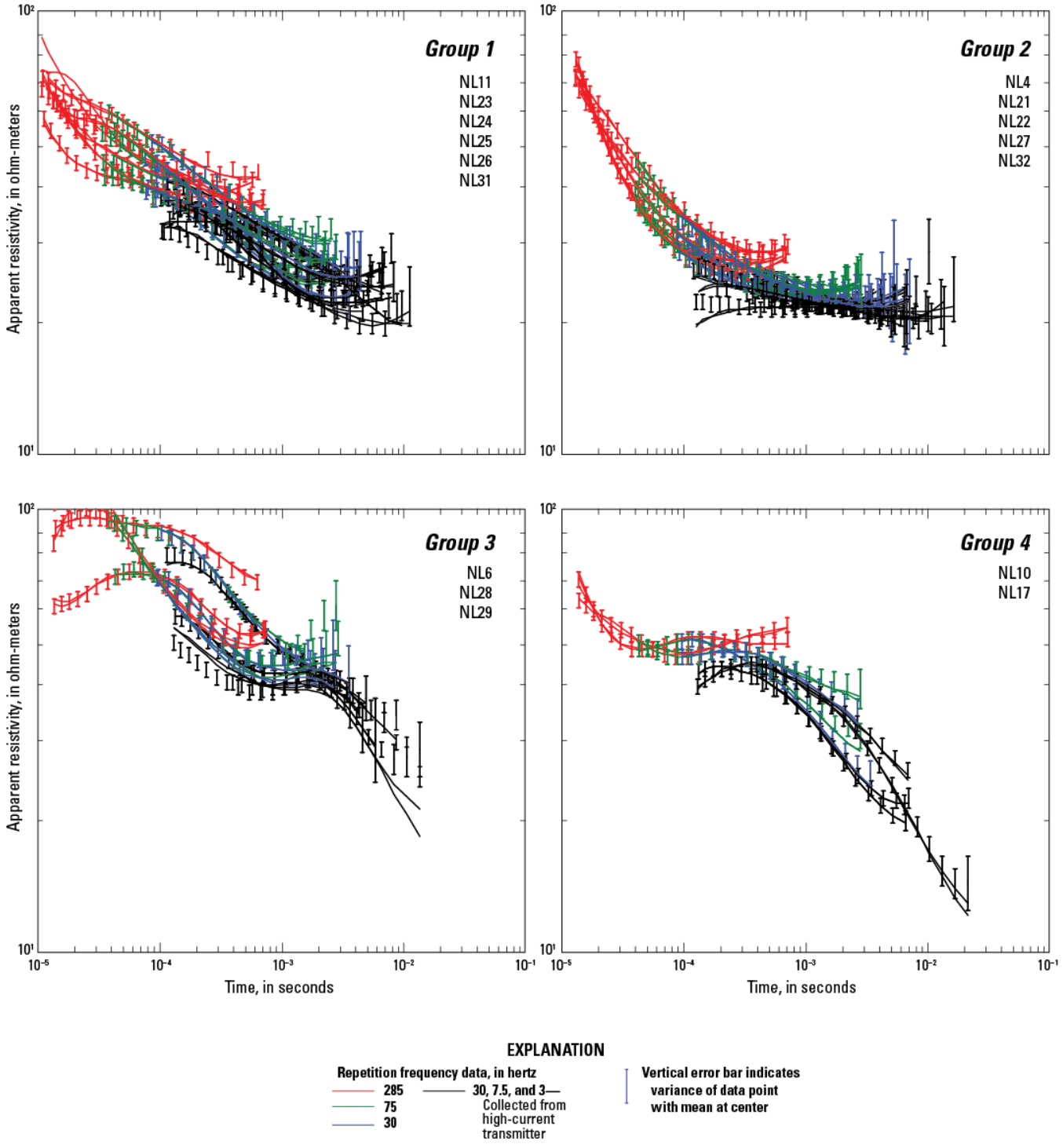

Figure 8. Graphs showing TEM data from Nelson Basin grouped by similarity of sounding curves and subbasins based on these groupings, Fort Irwin National Training Center, California. TEM sounding locations in Nelson Basin shown in figure 2.

Conclusion

Although time-domain electromagnetic (TEM) data have been used in other studies to identify the depth to water, the TEM data from Fort Irwin National Training Center (NTC) did not yield this information. The TEM data from the NTC can provide estimates of resistivity properties in lithologic units and the minimum thickness of the unsaturated zone. In some basins such as Nelson, the entire basin is subdivided by faults into numerous hydraulically isolated groundwater subbasins. By analyzing spatial correlations, separations of the thicknesses, and resistivities of TEM model layers, the TEM models provided insight for understanding the structure of each basin and the identification of potential subbasins. TEM results were particularly useful for information about the upper layers of the basin.

TEM and borehole resistivity data show five trends within and between basins:

A. The most common trend in nearly all of the data is one (and locally two) layers of high resistivity (>100 ohm-m, <500 ohm-m) in the near surface to depths greater than 500 ft below land surface.
B. Where confirmed by water-level measurements in nearby boreholes, the layers of high resistivity occur entirely in the unsaturated zone, and the transitions from high-to-low resistivity layers appear to correlate to variations in lithostratigraphic features and properties.
C. Below a thin near-surface layer of moderate resistivity (20–50 ohm-m) in most smooth models and some minimum layer models, the TEM model resistivity values generally decreased with depth.
D. The magnitude of the decrease in resistivity values varies between basins, but is fairly consistent within basins.
E. For the thick unsaturated zones on the NTC, the depth to water was not easily identified from resistivity methods alone (either TEM or borehole resistivity logs).

TEM surveys at the NTC were most successful in discriminating between fine- and coarse-grained deposits that may host groundwater. Beneath the near-surface resistive unit interpreted as an unsaturated Plio-Pleistocene to Holocene alluvial section present over most of the NTC, the TEM model layers can be grouped into two classes. The first class, observed in the northwestern part of the base, was characterized by moderate resistivities (20–35 ohm-m) and correlate to sections in boreholes in Nelson and Goldstone Basins where wells produce viable amounts of water. The second class, observed in the eastern half of the NTC, was characterized by resistivity values less than 20 ohm-m, and correlated to sections of low yield, fine-grained to clayey deposits in boreholes in Cronise Basin, the 'Central Corridor' Basin and Red Pass Basin. Prior to comparison of the TEM models to subsequently collected borehole data, the resistivity values less than 20 ohm-m in TEM models of data collected in the eastern half of the base were speculated to be potentially productive water-bearing zones.

Based on correlation with aquifer tests from wells screened at similar depths within the groundwater basins at the NTC, the TEM model resistivity threshold for a layer's ability to produce water is 20 ohm-m. Below this value (through comparisons to boreholes CRTH1, RDPS1, and CCT1), the sediments are too fine-grained and have resistivities less than 20 ohm-m as measured in borehole resistivity logs and modeled with TEM data. For example, a thick layer in the TEM model at depth in CR3 has a resistivity of 11.25 ohm-m; however, the water production from the deeper parts of the CRTH1 is negligible. In contrast, model layers that correlate to water-bearing units in the Nelson Basin have an average resistivity of 22.6 ohm-m and never less than 20 ohm-m. The contrast between resistivity values of saturated lower sections can be extended to other TEM models where borehole controls are not available to evaluate an area's potential to economically produce water.

Acknowledgments

We gratefully acknowledge financial support from Fort Irwin. We thank Burke Minsley and Frederick Day-Lewis for their reviews that improved the manuscript. Discussions on the geologic setting and well data with Peter Martin, Anthony Brown, David Buesch, and David Miller were helpful for putting these data in context. Jill Densmore, Sarah Falk, Joseph Nawikas, David O'Leary, Carl Muheim, Andy Morita, Krishangi Groover, Greg Smith, and Andrew Schneider (all of U.S. Geological Survey) assisted with data collection in the field.

References Cited

Archie, G.E., 1942, The electrical resistivity log as an aid in determining some reservoir characteristics: Petroleum Transactions American Institute of Mining, Metallurgical, and Petroleum Engineers, v. 146, p. 54–62.

Aster, R., Borchers, B., and Thurber, C., 2005, Parameter estimation and inverse problems: International Geophysics Series, Burlington, Mass., Elsevier Academic Press, no. 90, 301 p.

Auken, E., and Nebel, L., 2001, Getting started with SiTEM and SEMDI: University of Aarhus, Denmark, Hydro Geophysics Group.

Biella, G., Lozej, A., and Tabacco, I., 1983, Experimental study of some hydrogeophysical properties of unconsolidated porous media: Ground Water, v. 21, no. 6, p. 741–751.

Constable, S.C., Parker, R.L., and Constable, C.G., 1987, Occam's inversion—A practical algorithm for generating smooth models from electromagnetic sounding data: Geophysics, v. 52, no. 3, p. 289–300.

Christiansen, A.V. and Auken, E., 2010, A global measure for depth of investigation in EM and DC modeling: Australian Society of Exploration Geophysicists Annual meeting, 2010.

Christiansen, A.V., Auken, E., and Viezzoli, A., 2011, Quantification of modeling errors in airborne TEM caused by inaccurate system description: Geophysics, v. 76, p. F43–F52.

Danielsen, J.E., Auken, E., Jørgensen, F., Søndergaard, V., and Sørensen, K.I., 2003, The application of the transient electromagnetic method in hydrogeophysical surveys: Journal of Applied geophysics, v. 53, no. 4, p. 181–198.

Effersø, F., Auken, E., and Sørensen, K.I., 1999, Inversion of band-limited TEM responses: Geophysical prospecting, v. 47, p. 551–564.

Fitterman, D.V., and Labson, V.F., 2005, Electromagnetic induction methods for environmental problems, *in* Butler, D.K. ed., Near surface geophysics: Investigations in Geophysics series, no. 13, Society of Exploration Geophysicists, p. 301–355.

Geological Institute, 2002a, Vejledning i kalibrering af TEM måleudstyr (in Danish): Aarhus University, Denmark, 12 p.

Geological Institute, 2002b, Test og sammenligning af Transient Elektromagnetiske instrumenter i Danmark (in Danish): Aarhus University, Denmark,118 p.

Jachens, R.C., and Langenheim, V.E., 2014, Gravity survey and interpretation of Fort Irwin and vicinity, Mojave Desert, California, chap. H *of* Buesch, D.C., ed., Geology and geophysics applied to groundwater hydrology at Fort Irwin, California: U.S. Geological Survey Open-File Report 2013–1024 (this volume).

Hallenburg, J.K., 1998, Non-hydrocarbon methods of geophysical formation evaluation: Boca Raton, Florida, Lewis Publishers, 265 p.

Hearst, J.R., and Nelson, P.H., 1985, Borehole logging for physical properties: New York, McGraw-Hill, 571 p.

Hearst, J.R., Nelson, P.H., and Paillet, F.L., 2000, Borehole logging for physical properties (2d ed.): New York, John Wiley, 483 p.

Hobza, C.M., Asch, T.H., and Bedrosian, P.A., 2011, Hydrostratigraphic interpretation of test-hole and geophysical data, Upper Loup River Basin, Nebraska, 2008-10: U.S. Geological Survey Open-File Report 2011–1289, 60 p.

Keller, G.V., 1987, Rock and mineral properties, *in* Nabighian, M.N., ed., Electromagnetic methods in applied geophysics theory: Tulsa, Oklahoma, Society of Exploration Geophysicists, v. 1, p. 13–51.

Keller, G.V., 1989, Electrical properties, *in* Carmichael, R.S., ed., Practical handbook of physical properties of rocks and minerals: Boca Raton, Florida, CRC Press, p. 359–427.

Kwader, T., 1985, Estimating aquifer permeability from formation resistivity factors: Ground Water, v. 23, no. 6, p. 762–766.

Minsley, B.J., Ball, L.B., Burton, B.L., Caine, J.S., Curry-Elrod, E., and Manning, A.H., 2010, Geophysical characterization of subsurface properties relevant to the hydrology of the Standard Mine in Elk Basin, Colorado: U.S. Geological Survey Open-File Report 2009-1284, 46 p.

Nabighian, M.N., and Macnae, J.C., 1991, Time-domain electromagnetic prospecting methods, *in* Nabighian, M.N., ed., Electromagnetic methods in applied geophysics, v. 2: Society of Exploration Geophysicists, p. 427–520.

Palacky, G. J., 1987, Resistivity characteristics of geologic targets, *in* Nabighian, M.N., ed., Electromagnetic methods in applied geophysics, v. 1: Society of Exploration Geophysicists, p. 53–129.

Appendix A. Graphs of TEM Sounding Data and Model Results at Fort Irwin, California

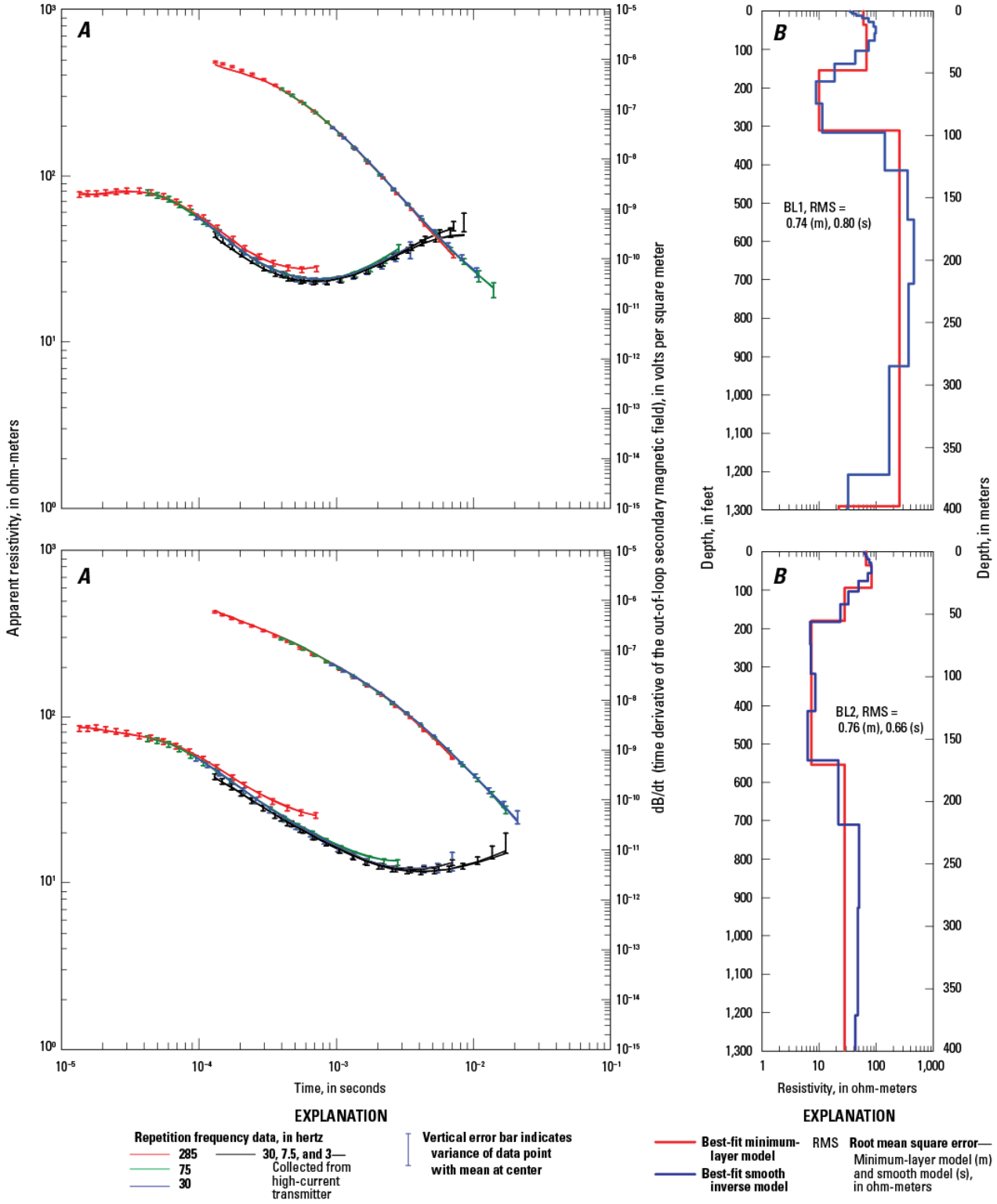

Figure A1. Graphs showing relations between *A*, central-loop resistivity (lower left curve, left axis), out-of-loop vertical magnetic field (time-derivative, upper right curve, right axis), and time; *B*, depth below land surface and subsurface resistivity modeled from TEM sounding for sites BL1 and BL2, Fort Irwin National Training Center, California.

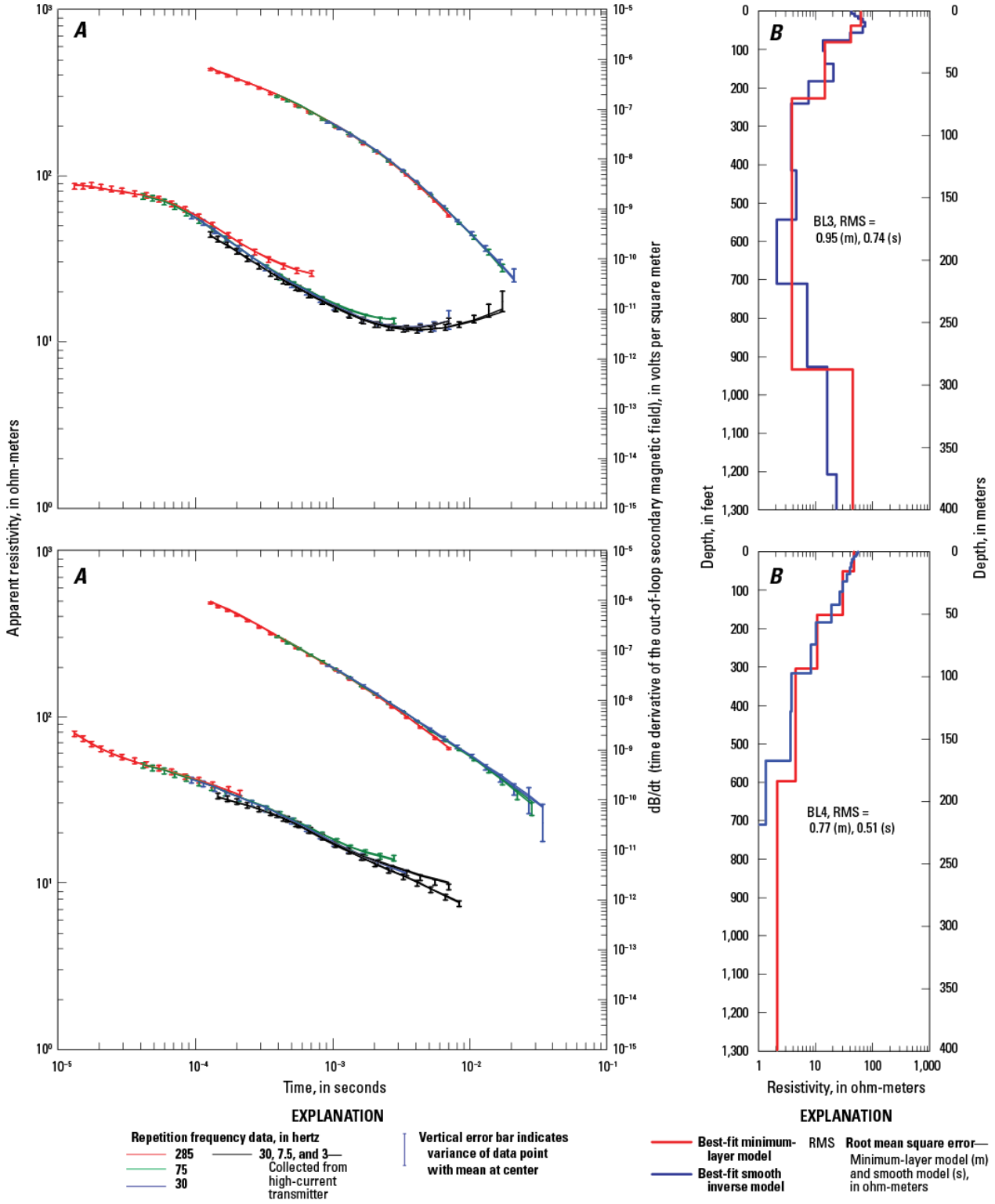

Figure A2. Graphs showing relations between *A*, central-loop resistivity (lower left curve, left axis), out-of-loop vertical magnetic field (time-derivative, upper right curve, right axis), and time; *B*, depth below land surface and subsurface resistivity modeled from TEM sounding for sites BL3 and BL4, Fort Irwin National Training Center, California.

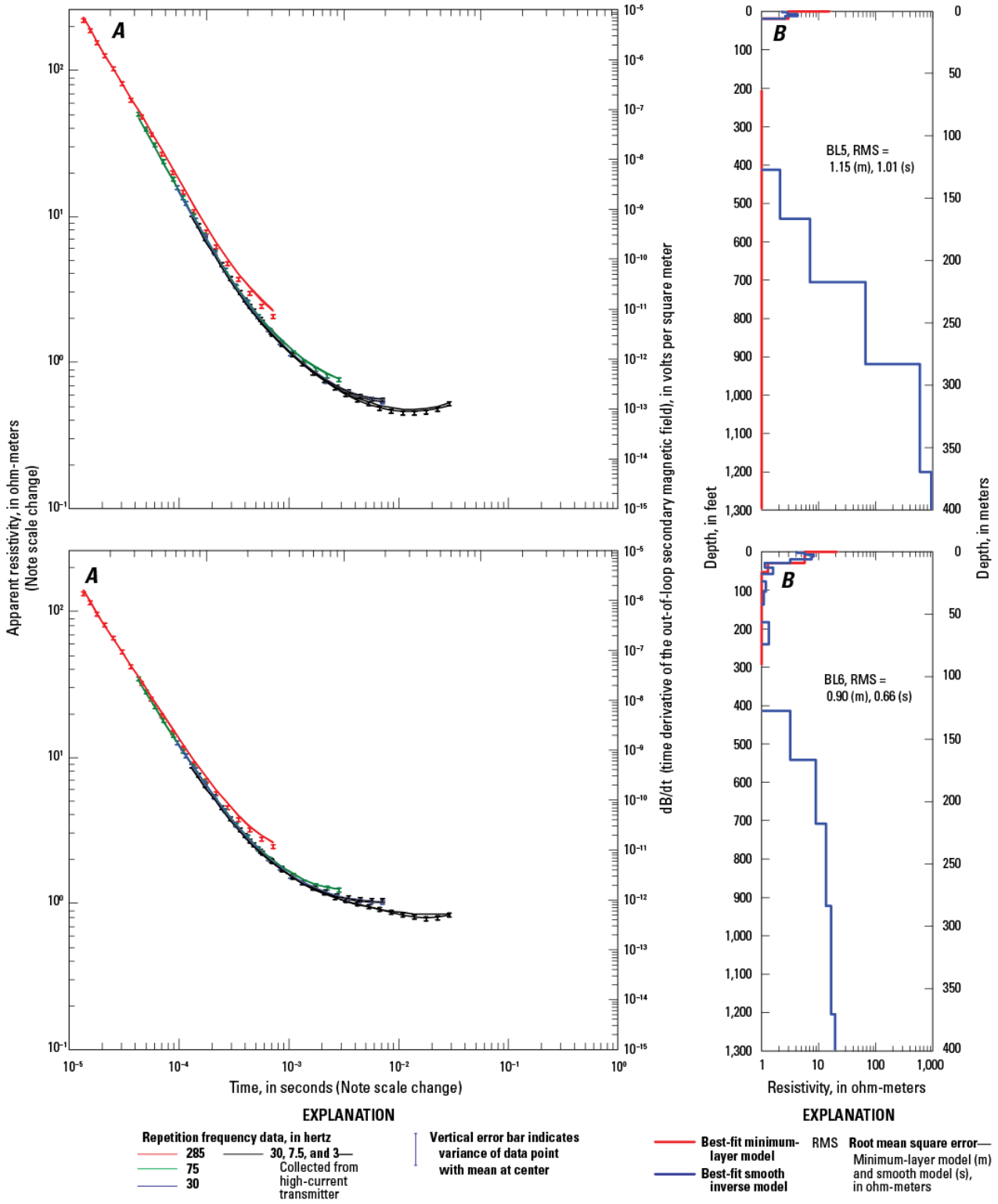

Figure A3. Graphs showing relations between *A*, central-loop resistivity (lower left curve, left axis), out-of-loop vertical magnetic field (time-derivative, upper right curve, right axis), and time; *B*, depth below land surface and subsurface resistivity modeled from TEM sounding for sites BL5 and BL6, Fort Irwin National Training Center, California.

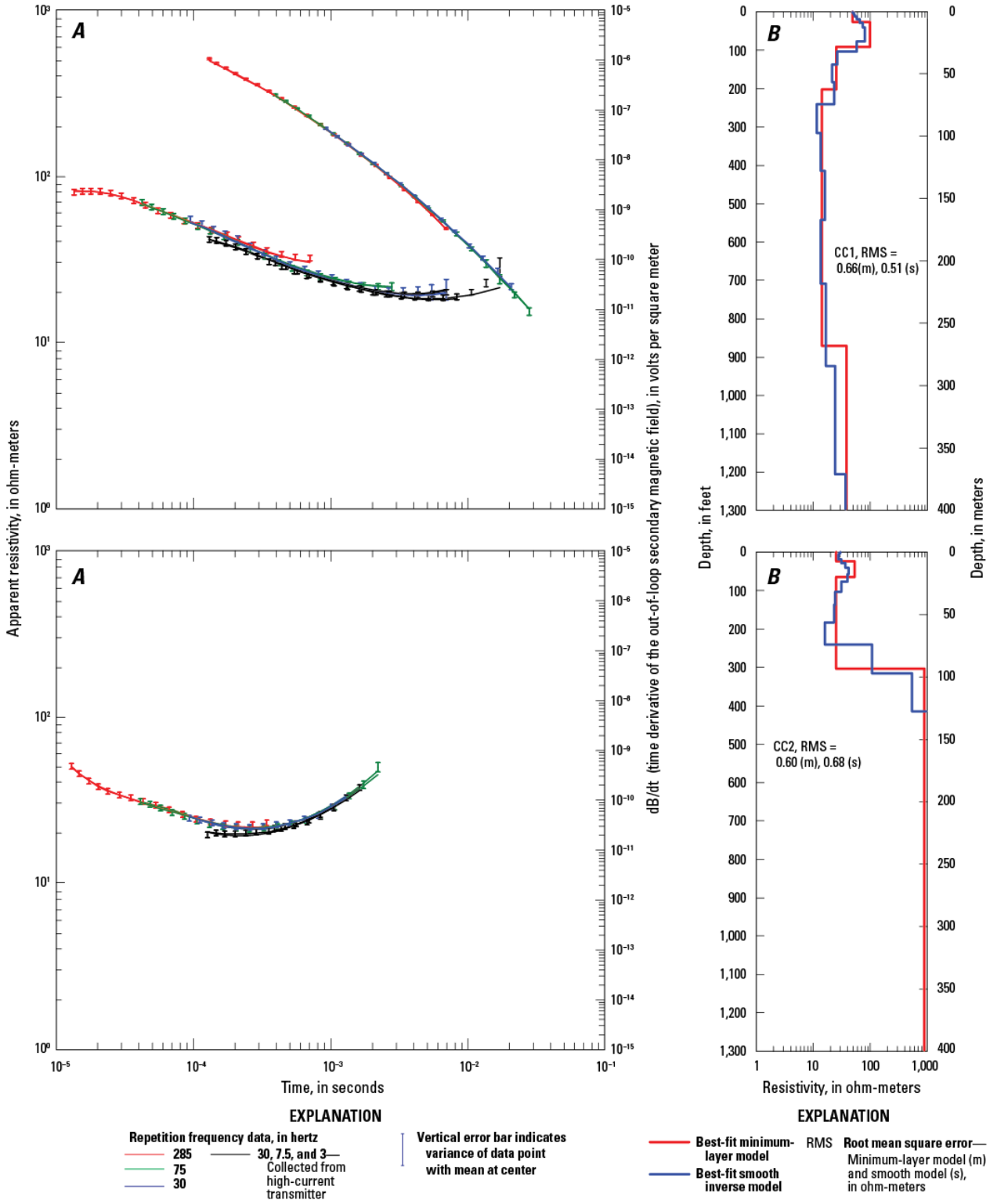

Figure A4. Graphs showing relations between *A*, central-loop resistivity (lower left curve, left axis), out-of-loop vertical magnetic field (time-derivative, upper right curve, right axis), and time; *B*, depth below land surface and subsurface resistivity modeled from TEM sounding for sites CC1 and CC2, Fort Irwin National Training Center, California.

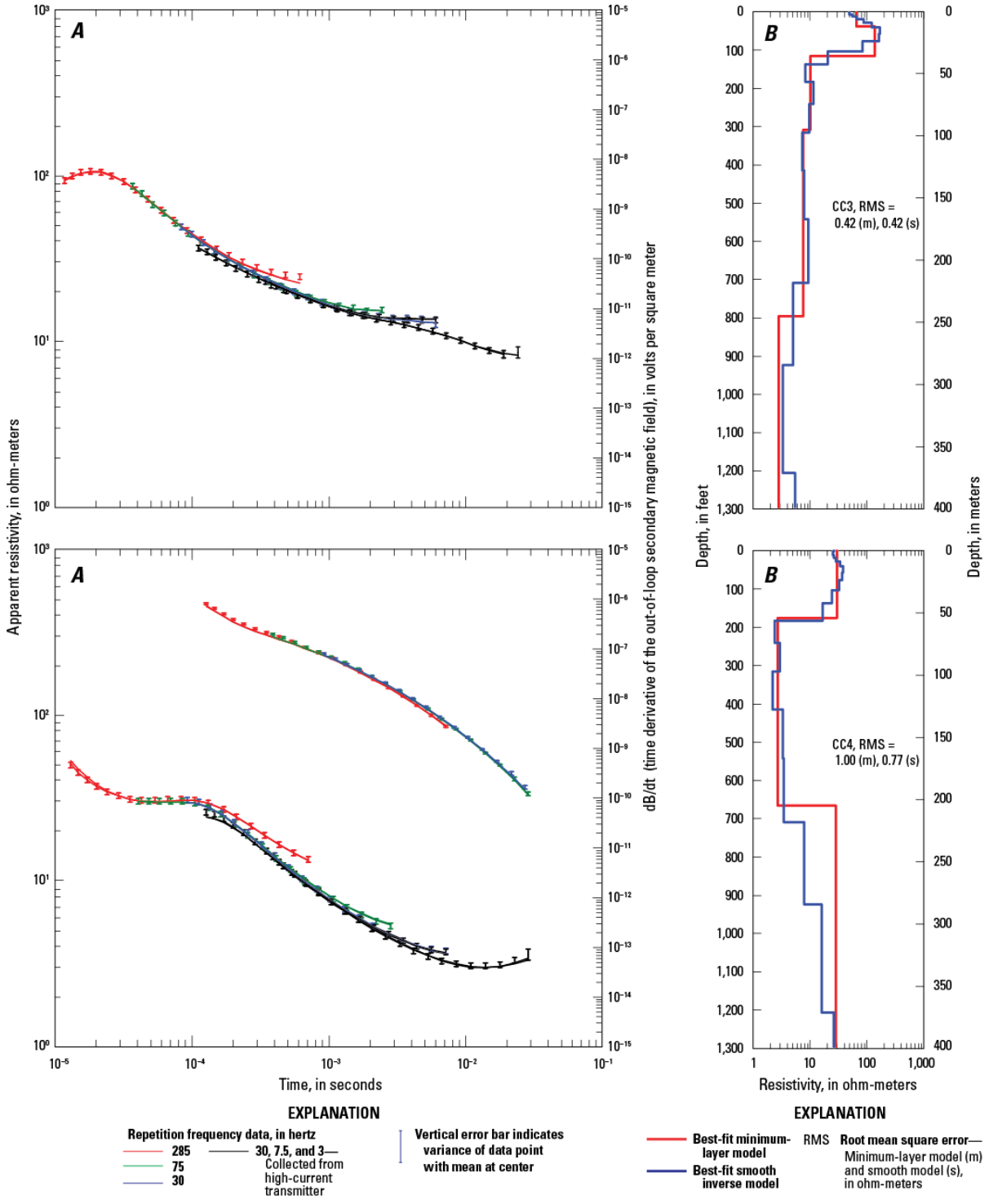

Figure A5. Graphs showing relations between *A*, central-loop resistivity (lower left curve, left axis), out-of-loop vertical magnetic field (time-derivative, upper right curve, right axis), and time; *B*, depth below land surface and subsurface resistivity modeled from TEM sounding for sites CC3 and CC4, Fort Irwin National Training Center, California.

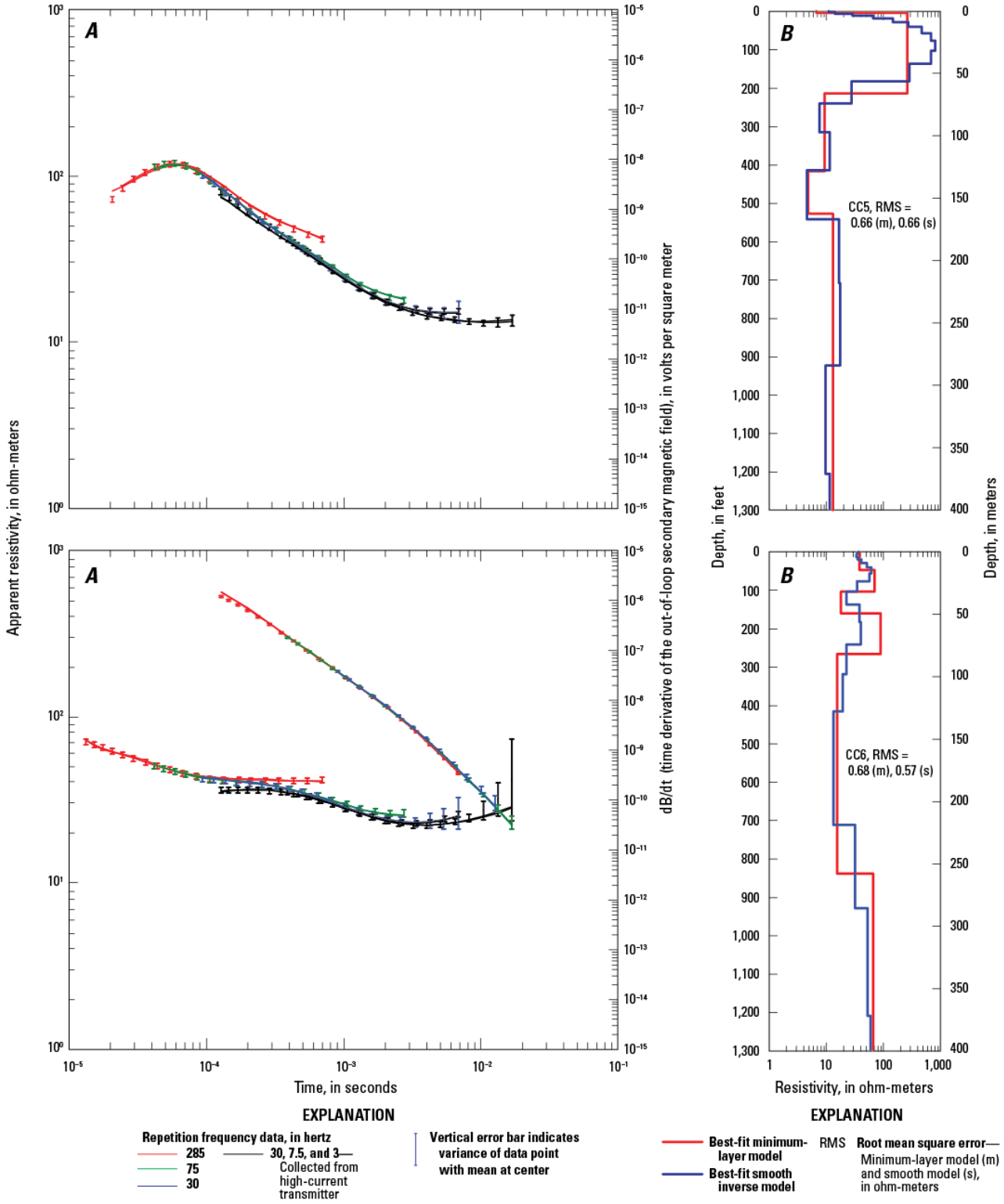

Figure A6. Graphs showing relations between *A*, central-loop resistivity (lower left curve, left axis), out-of-loop vertical magnetic field (time-derivative, upper right curve, right axis), and time; *B*, depth below land surface and subsurface resistivity modeled from TEM sounding for sites CC5 and CC6, Fort Irwin National Training Center, California.

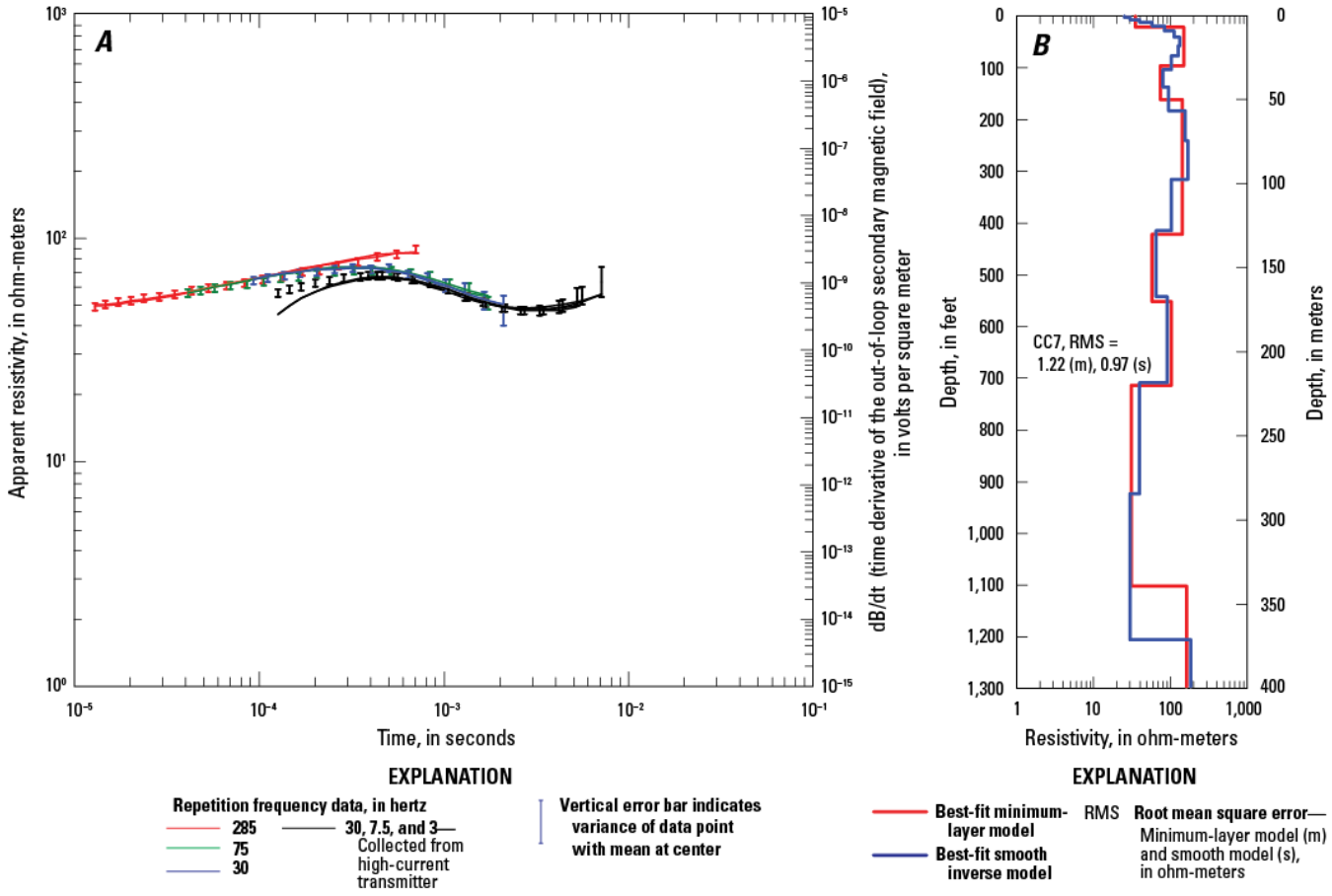

Figure A7. Graphs showing relations between *A*, central-loop resistivity (lower left curve, left axis), out-of-loop vertical magnetic field (time-derivative, upper right curve, right axis), and time; *B*, depth below land surface and subsurface resistivity modeled from TEM sounding for site CC7, Fort Irwin National Training Center, California.

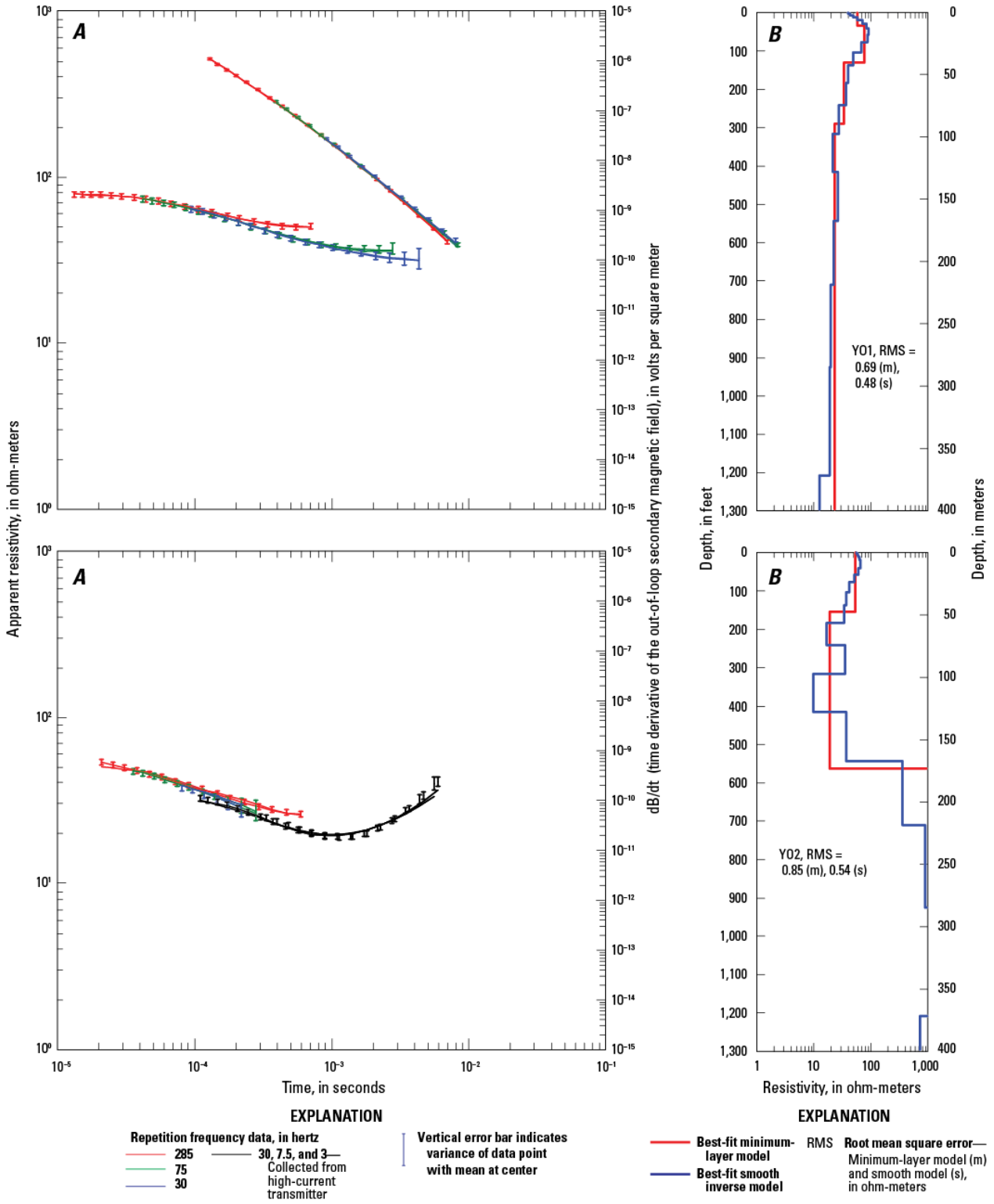

Figure A8. Graphs showing relations between *A*, central-loop resistivity (lower left curve, left axis), out-of-loop vertical magnetic field (time-derivative, upper right curve, right axis), and time; *B*, depth below land surface and subsurface resistivity modeled from TEM sounding for sites YO1 and YO2, Fort Irwin National Training Center, California.

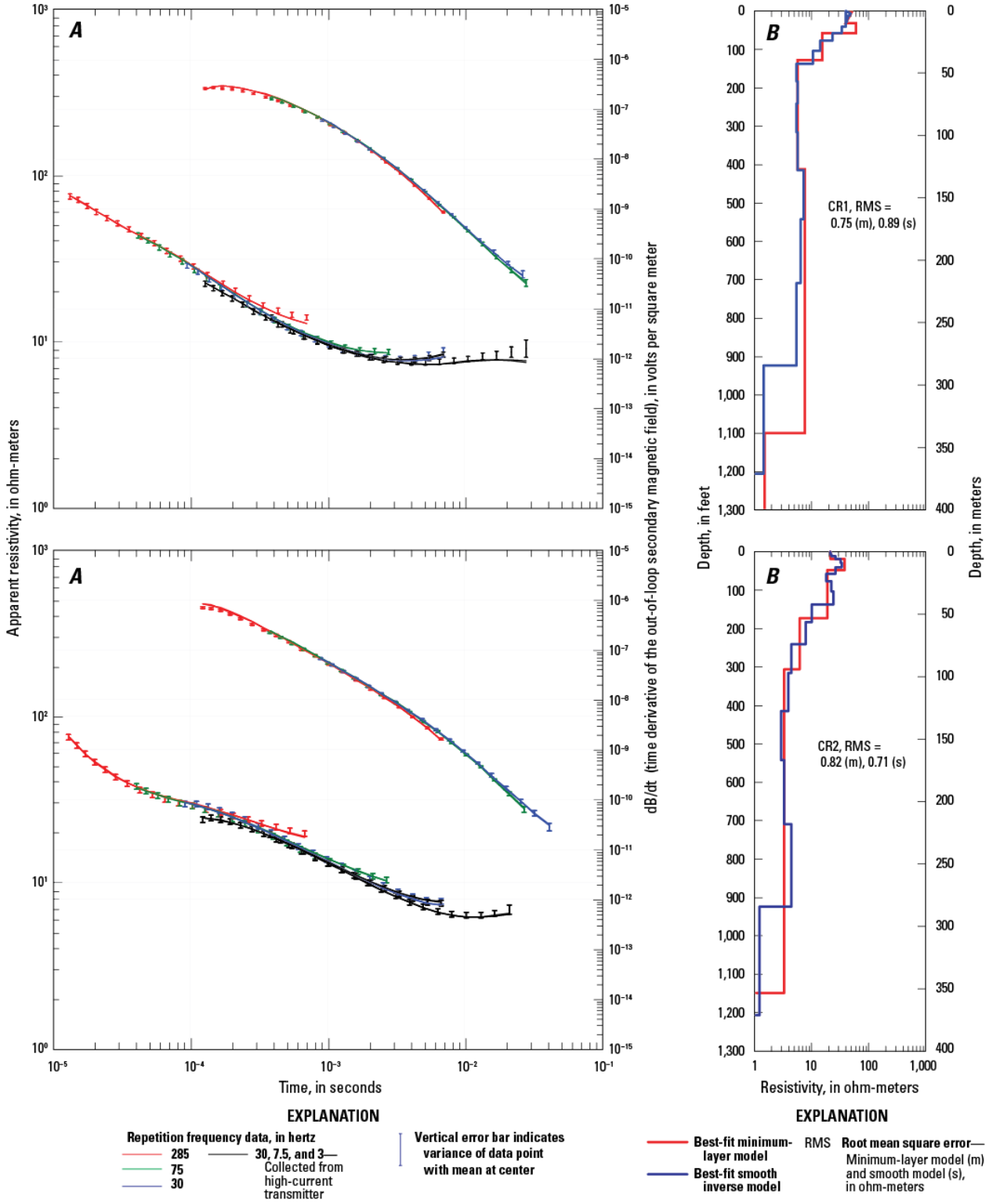

Figure A9. Graphs showing relations between *A*, central-loop resistivity (lower left curve, left axis), out-of-loop vertical magnetic field (time-derivative, upper right curve, right axis), and time; *B*, depth below land surface and subsurface resistivity modeled from TEM sounding for sites CR1 and CR2, Fort Irwin National Training Center, California.

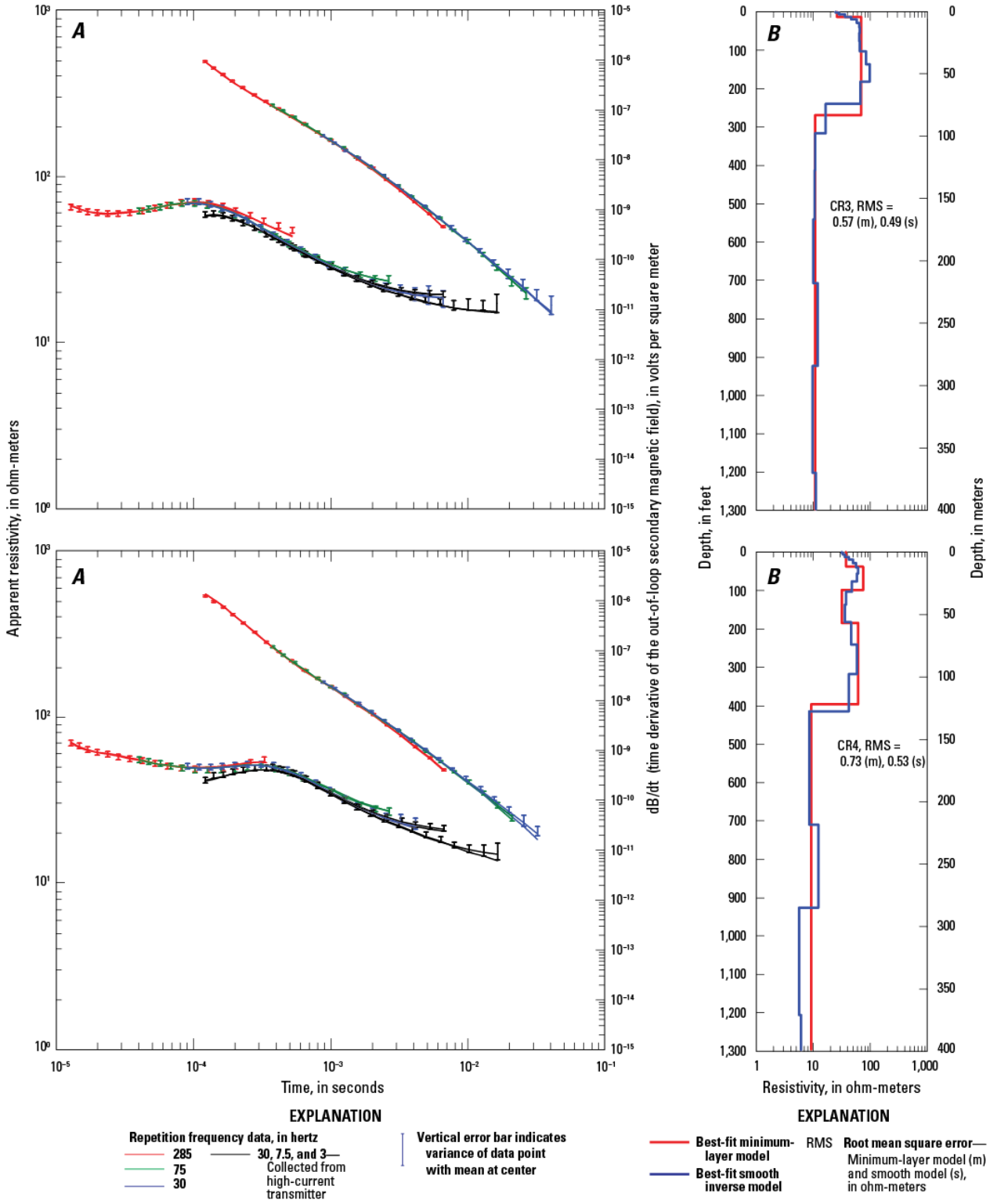

Figure A10. Graphs showing relations between *A*, central-loop resistivity (lower left curve, left axis), out-of-loop vertical magnetic field (time-derivative, upper right curve, right axis), and time; *B*, depth below land surface and subsurface resistivity modeled from TEM sounding for sites CR3 and CR4, Fort Irwin National Training Center, California.

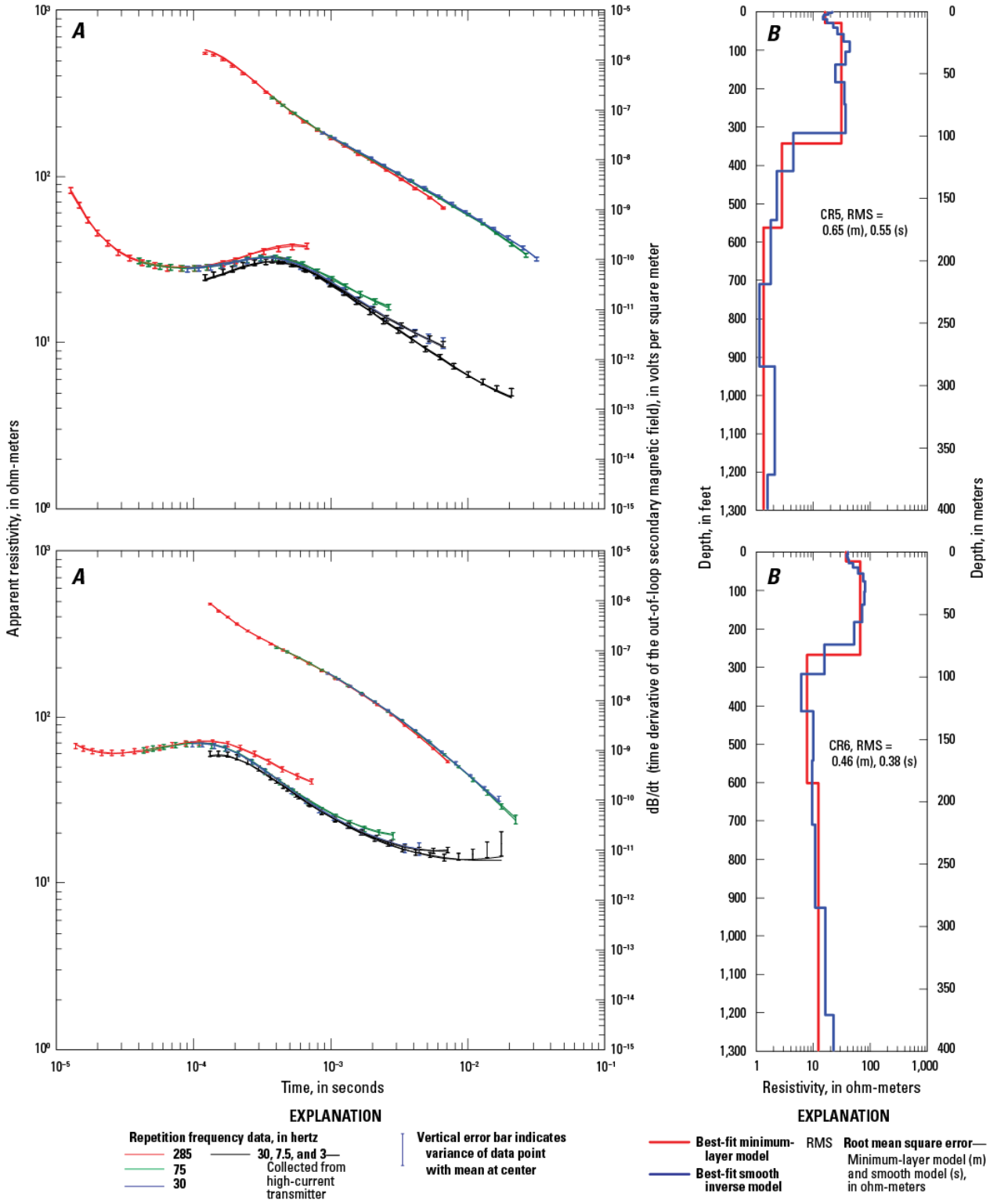

Figure A11. Graphs showing relations between *A*, central-loop resistivity (lower left curve, left axis), out-of-loop vertical magnetic field (time-derivative, upper right curve, right axis), and time; *B*, depth below land surface and subsurface resistivity modeled from TEM sounding for sites CR5 and CR6, Fort Irwin National Training Center, California.

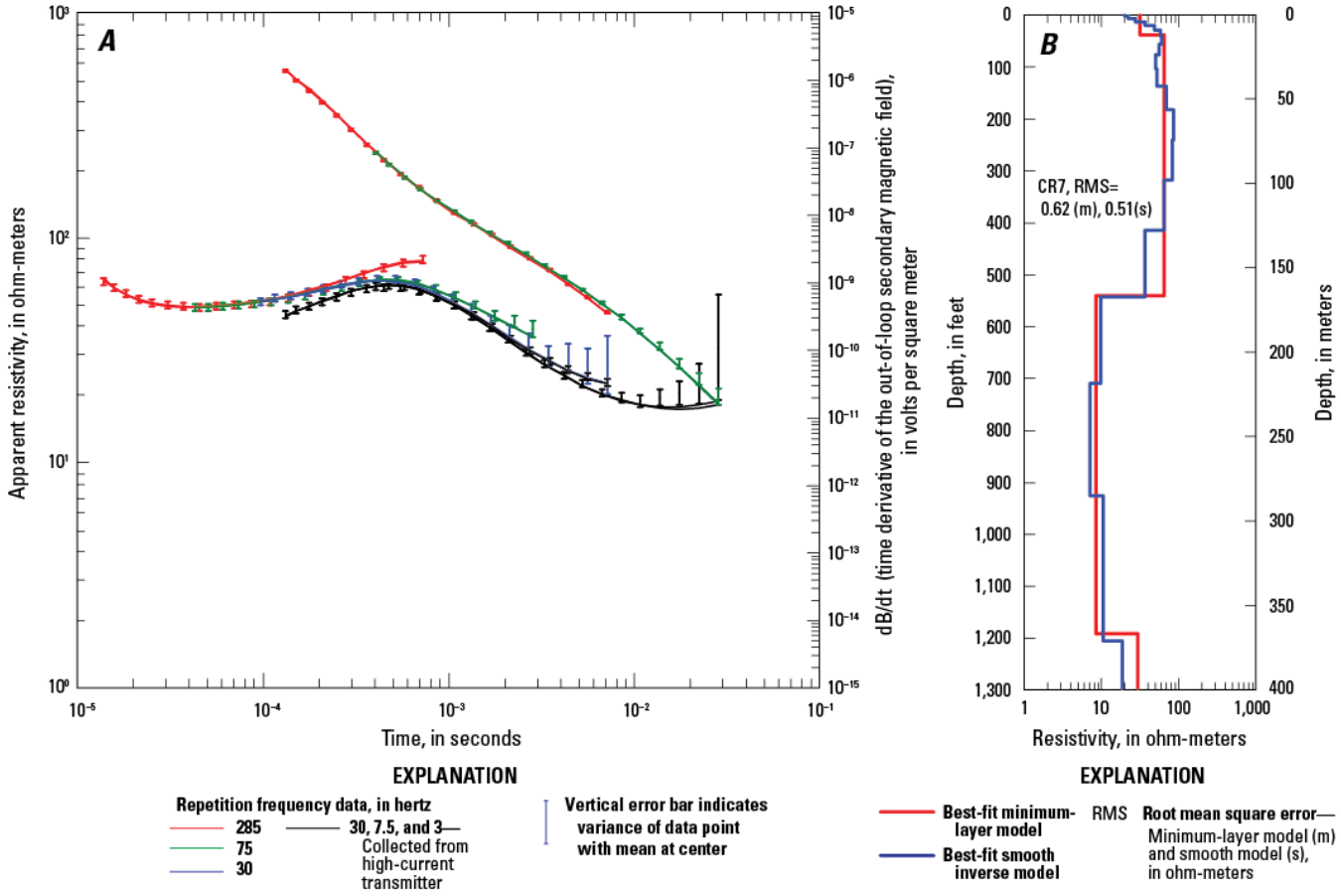

Figure A12. Graphs showing relations between *A*, central-loop resistivity (lower left curve, left axis), out-of-loop vertical magnetic field (time-derivative, upper right curve, right axis), and time; *B*, depth below land surface and subsurface resistivity modeled from TEM sounding for site CR7, Fort Irwin National Training Center, California.

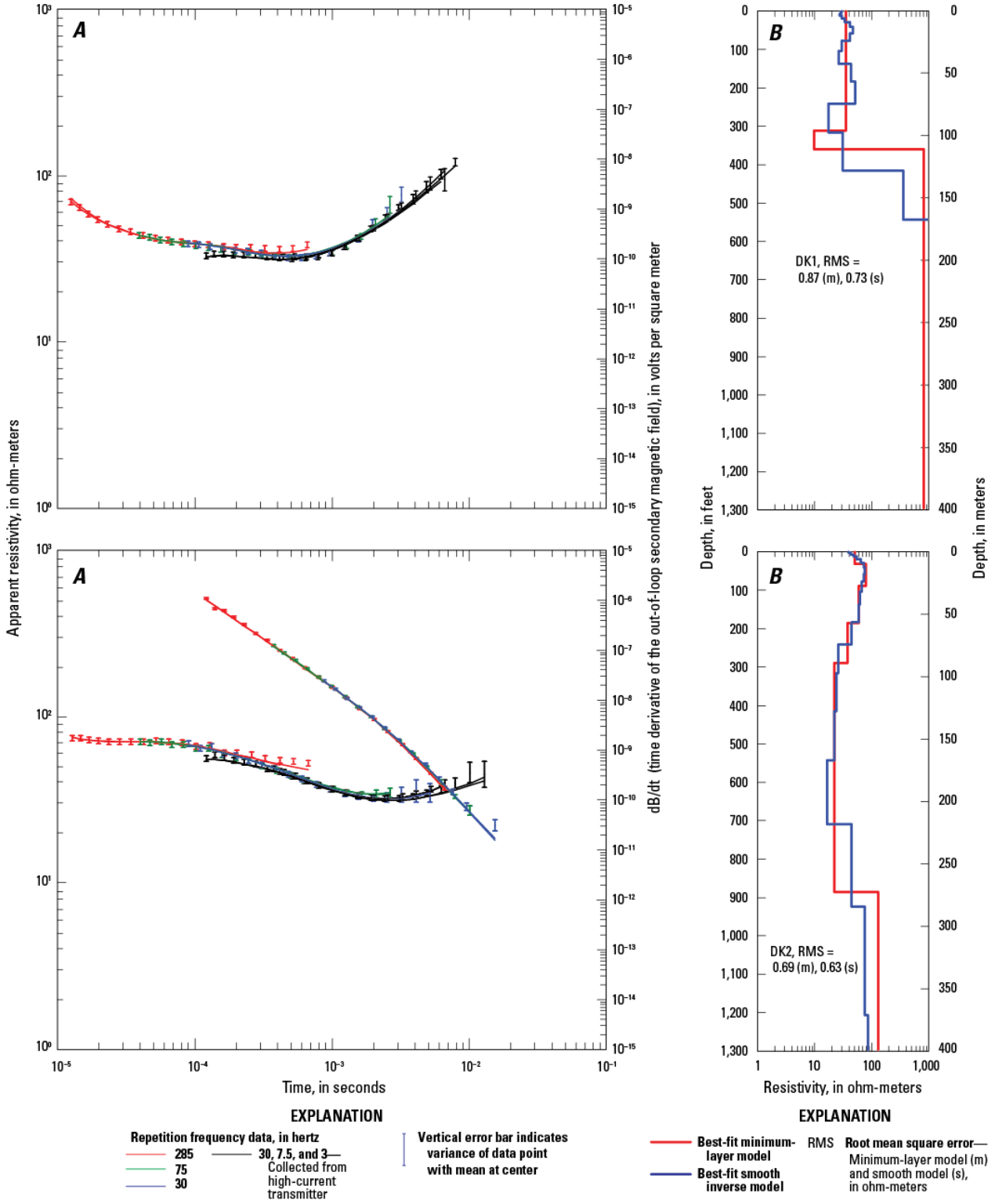

Figure A13. Graphs showing relations between *A*, central-loop resistivity (lower left curve, left axis), out-of-loop vertical magnetic field (time-derivative, upper right curve, right axis), and time; *B*, depth below land surface and subsurface resistivity modeled from TEM sounding for sites DK1 and DK2, Fort Irwin National Training Center, California.

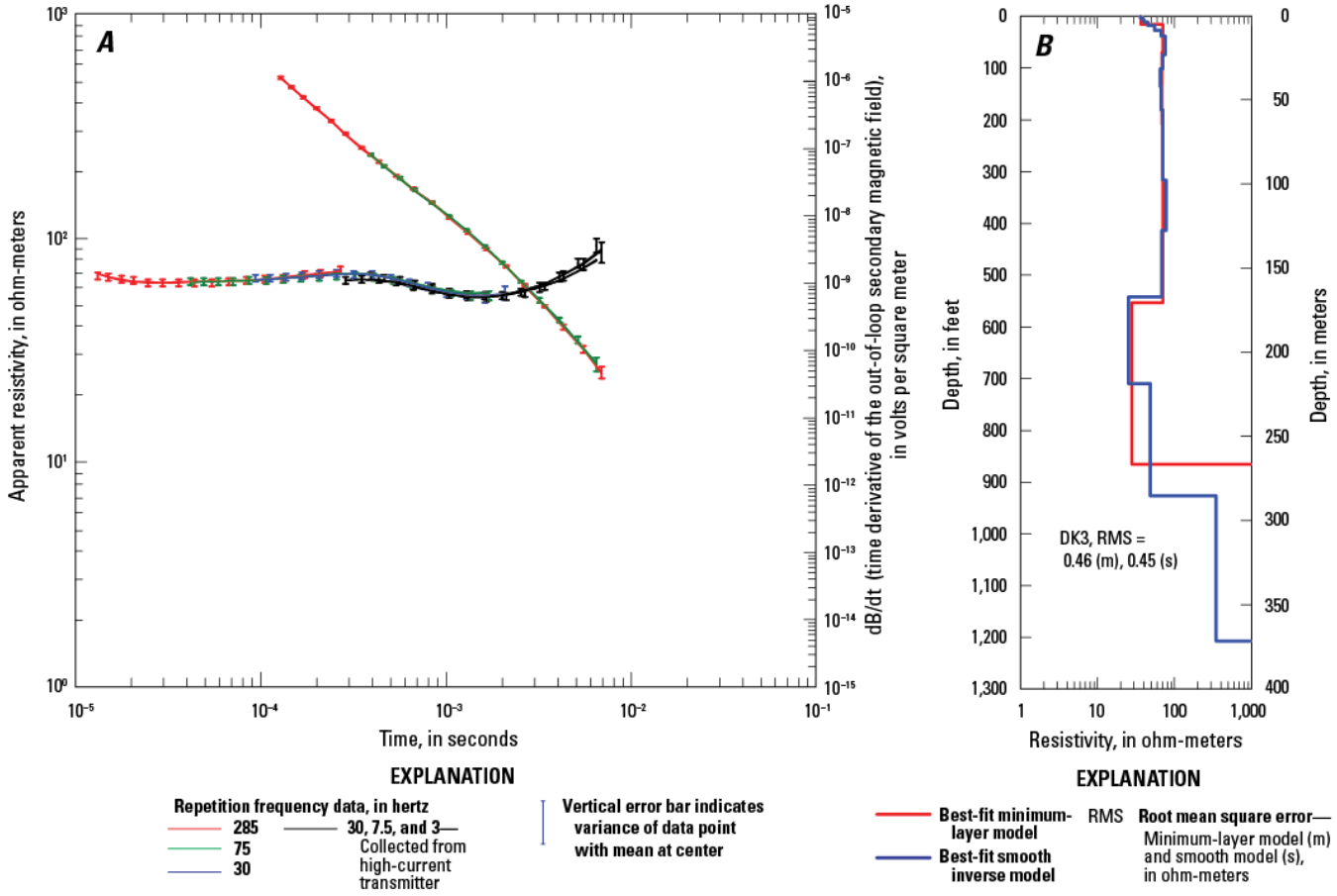

Figure A14. Graphs showing relations between *A*, central-loop resistivity (lower left curve, left axis), out-of-loop vertical magnetic field (time-derivative, upper right curve, right axis), and time; *B*, depth below land surface and subsurface resistivity modeled from TEM sounding for site DK3, Fort Irwin National Training Center, California.

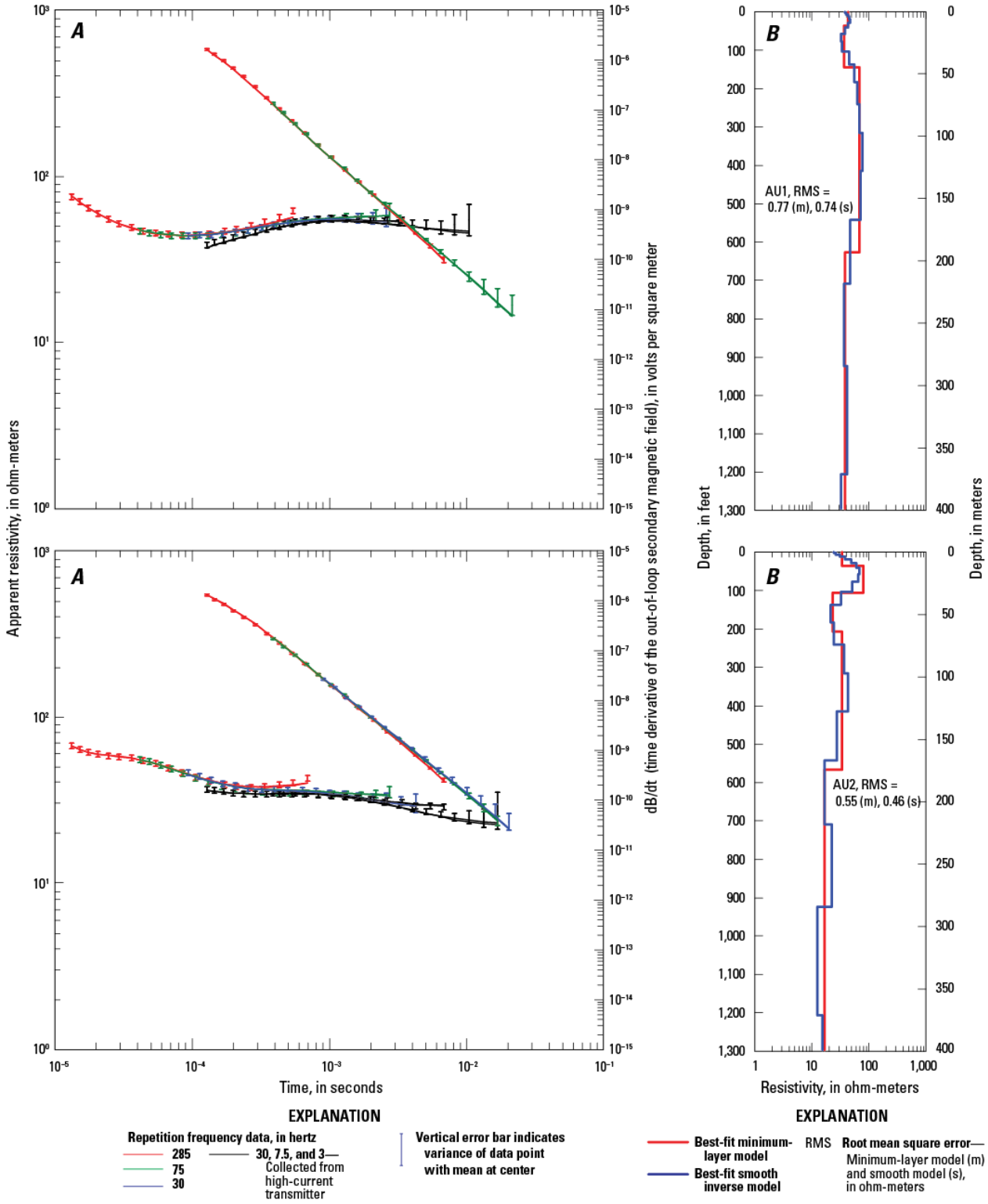

Figure A15. Graphs showing relations between *A*, central-loop resistivity (lower left curve, left axis), out-of-loop vertical magnetic field (time-derivative, upper right curve, right axis), and time; *B*, depth below land surface and subsurface resistivity modeled from TEM sounding for sites AU1 and AU2, Fort Irwin National Training Center, California.

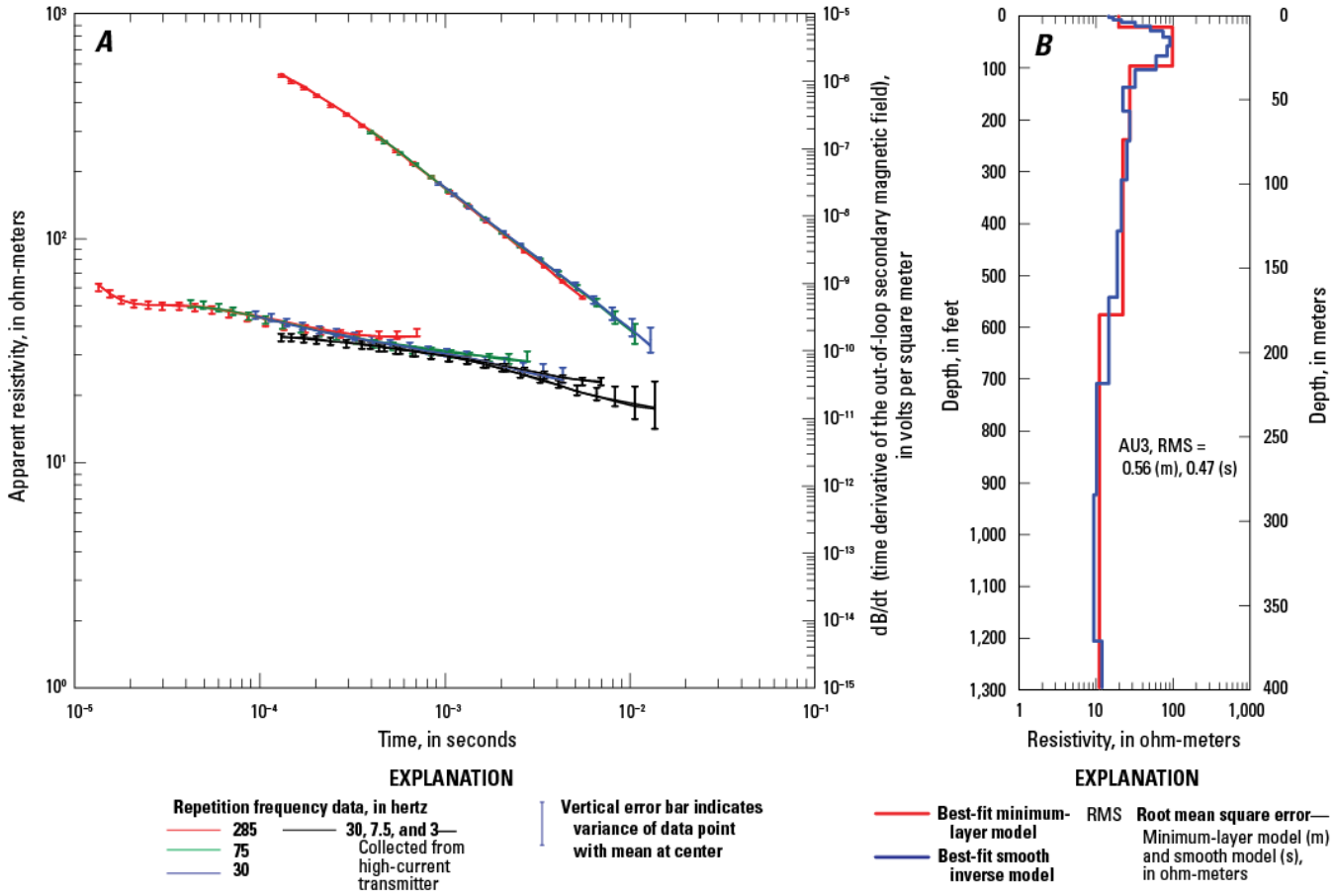

Figure A16. Graphs showing relations between *A*, central-loop resistivity (lower left curve, left axis), out-of-loop vertical magnetic field (time-derivative, upper right curve, right axis), and time; *B*, depth below land surface and subsurface resistivity modeled from TEM sounding for site AU3, Fort Irwin National Training Center, California.

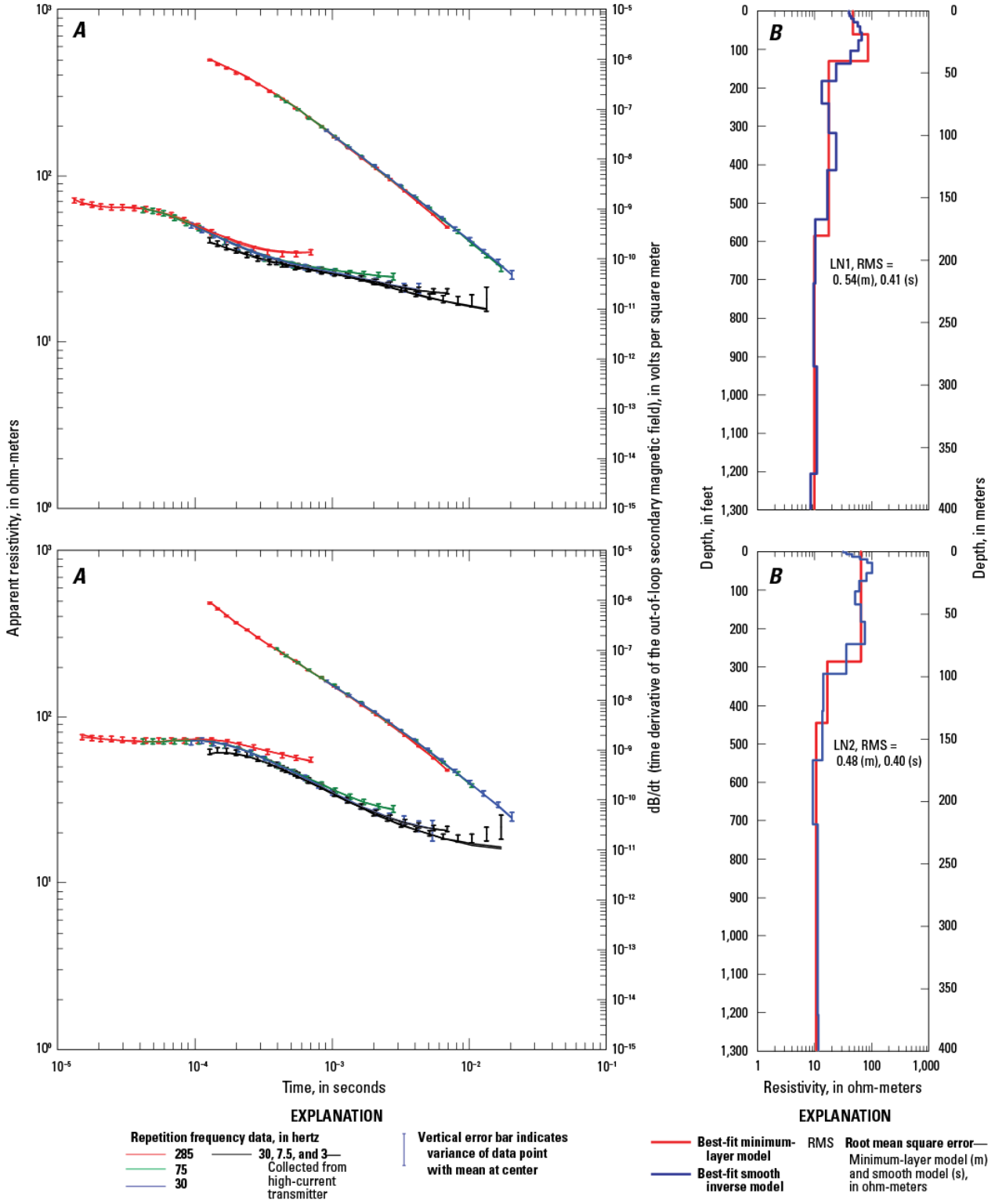

Figure A17. Graphs showing relations between *A*, central-loop resistivity (lower left curve, left axis), out-of-loop vertical magnetic field (time-derivative, upper right curve, right axis), and time; *B*, depth below land surface and subsurface resistivity modeled from TEM sounding for sites LN1 and LN2, Fort Irwin National Training Center, California.

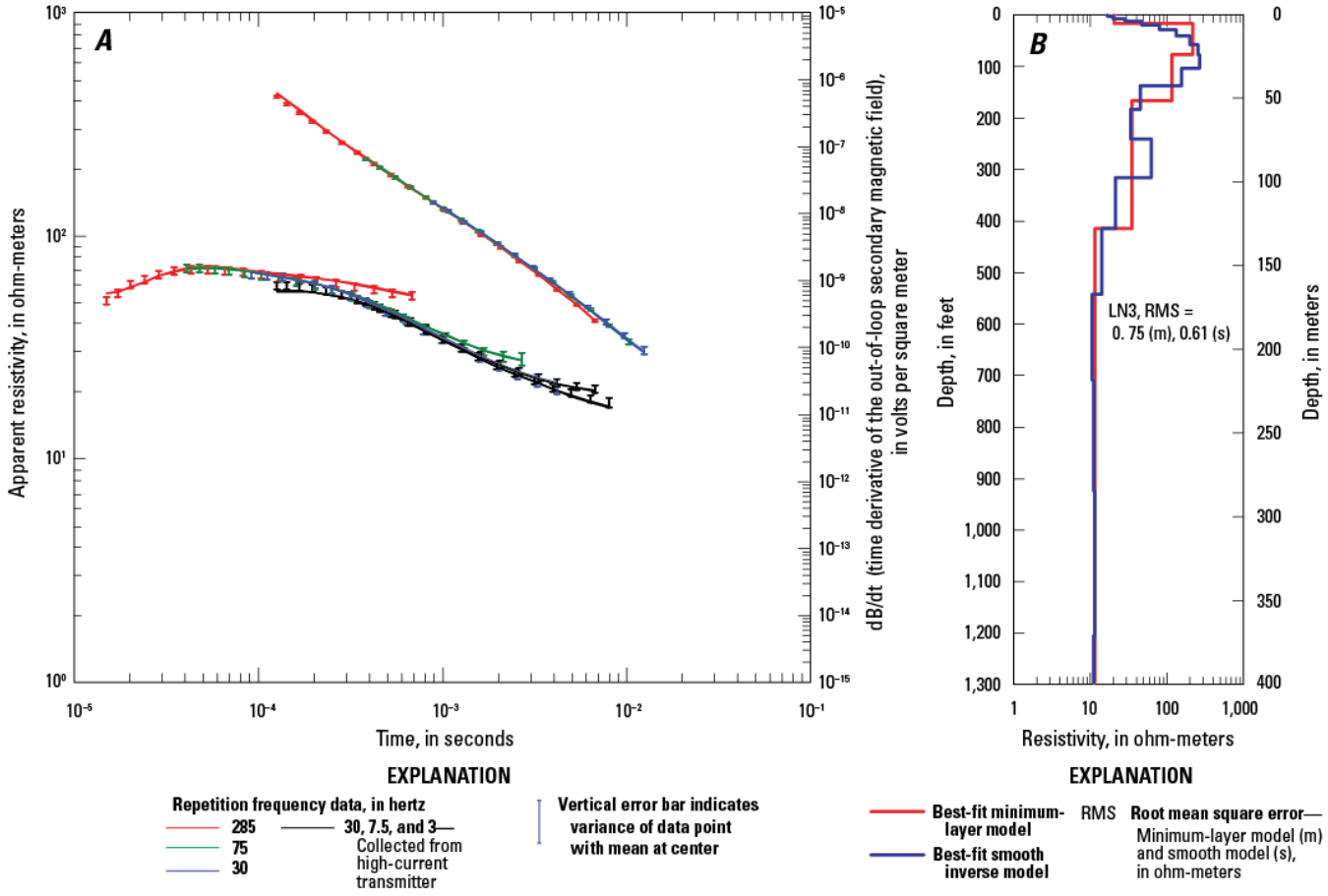

Figure A18. Graphs showing relations between *A*, central-loop resistivity (lower left curve, left axis), out-of-loop vertical magnetic field (time-derivative, upper right curve, right axis), and time; *B*, depth below land surface and subsurface resistivity modeled from TEM sounding for sites LN3, Fort Irwin National Training Center, California.

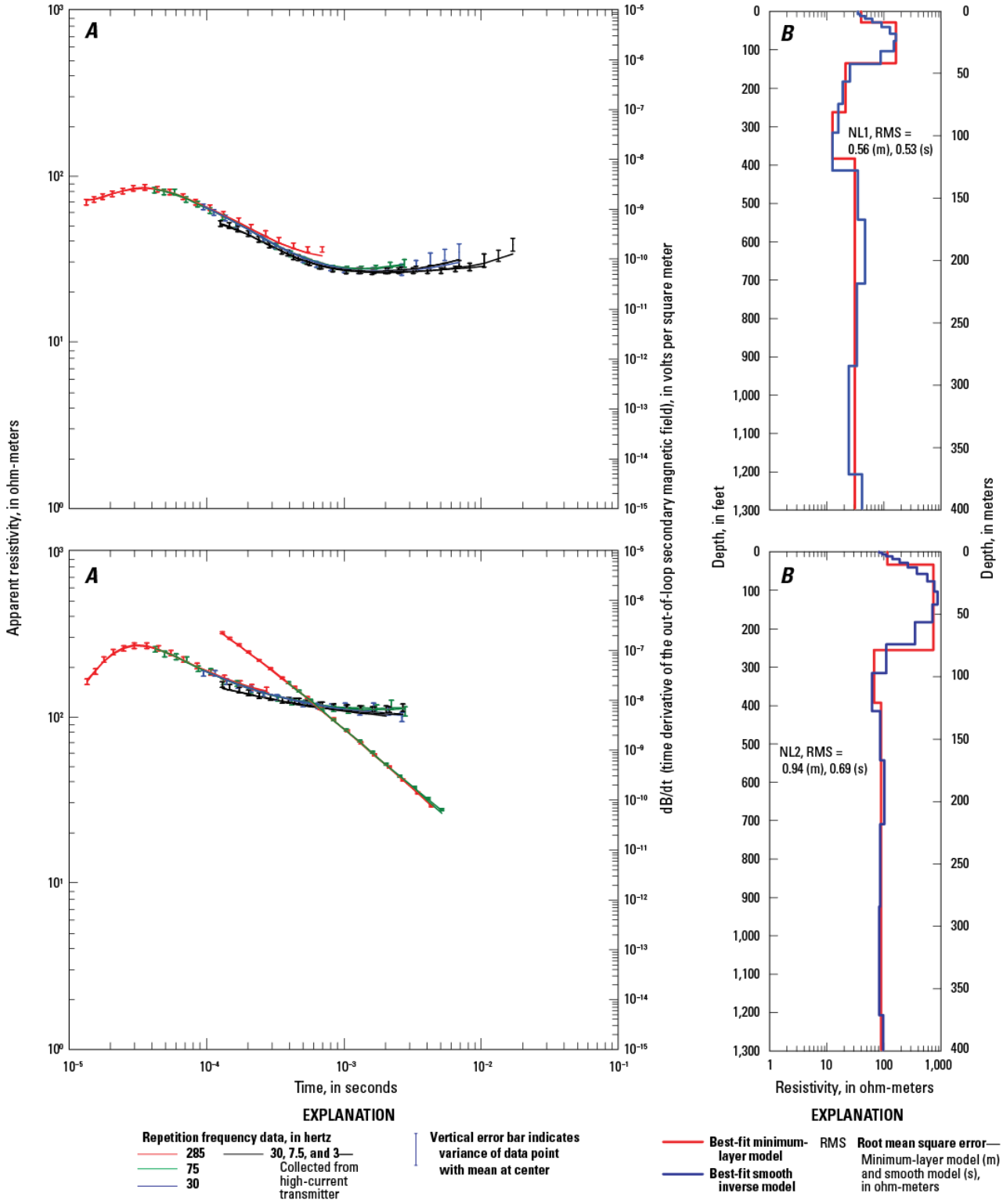

Figure A19. Graphs showing relations between *A*, central-loop resistivity (lower left curve, left axis), out-of-loop vertical magnetic field (time-derivative, upper right curve, right axis), and time; *B*, depth below land surface and subsurface resistivity modeled from TEM sounding for sites NL1 and NL2, Fort Irwin National Training Center, California.

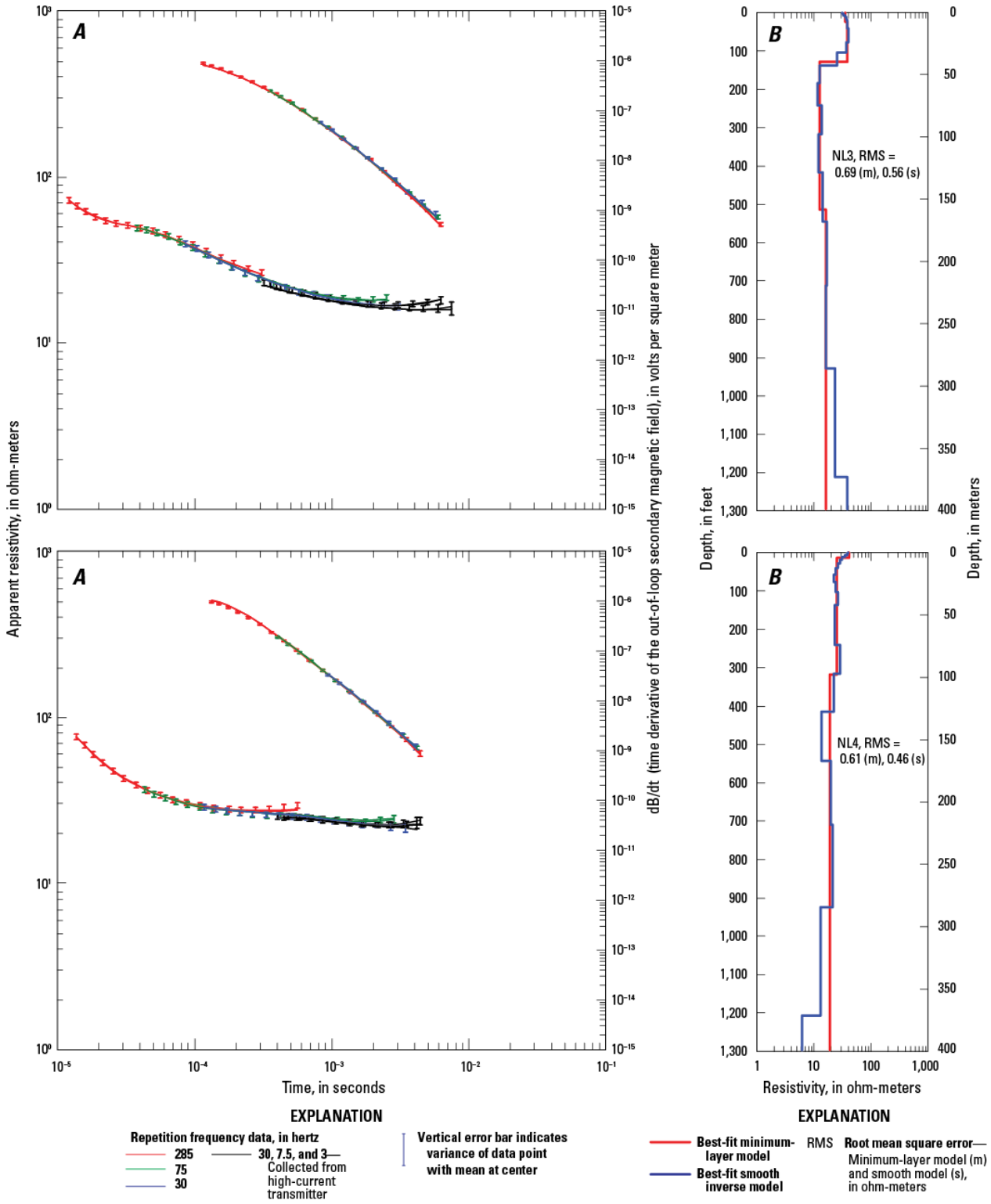

Figure A20. Graphs showing relations between *A*, central-loop resistivity (lower left curve, left axis), out-of-loop vertical magnetic field (time-derivative, upper right curve, right axis), and time; *B*, depth below land surface and subsurface resistivity modeled from TEM sounding for sites NL3 and NL4, Fort Irwin National Training Center, California.

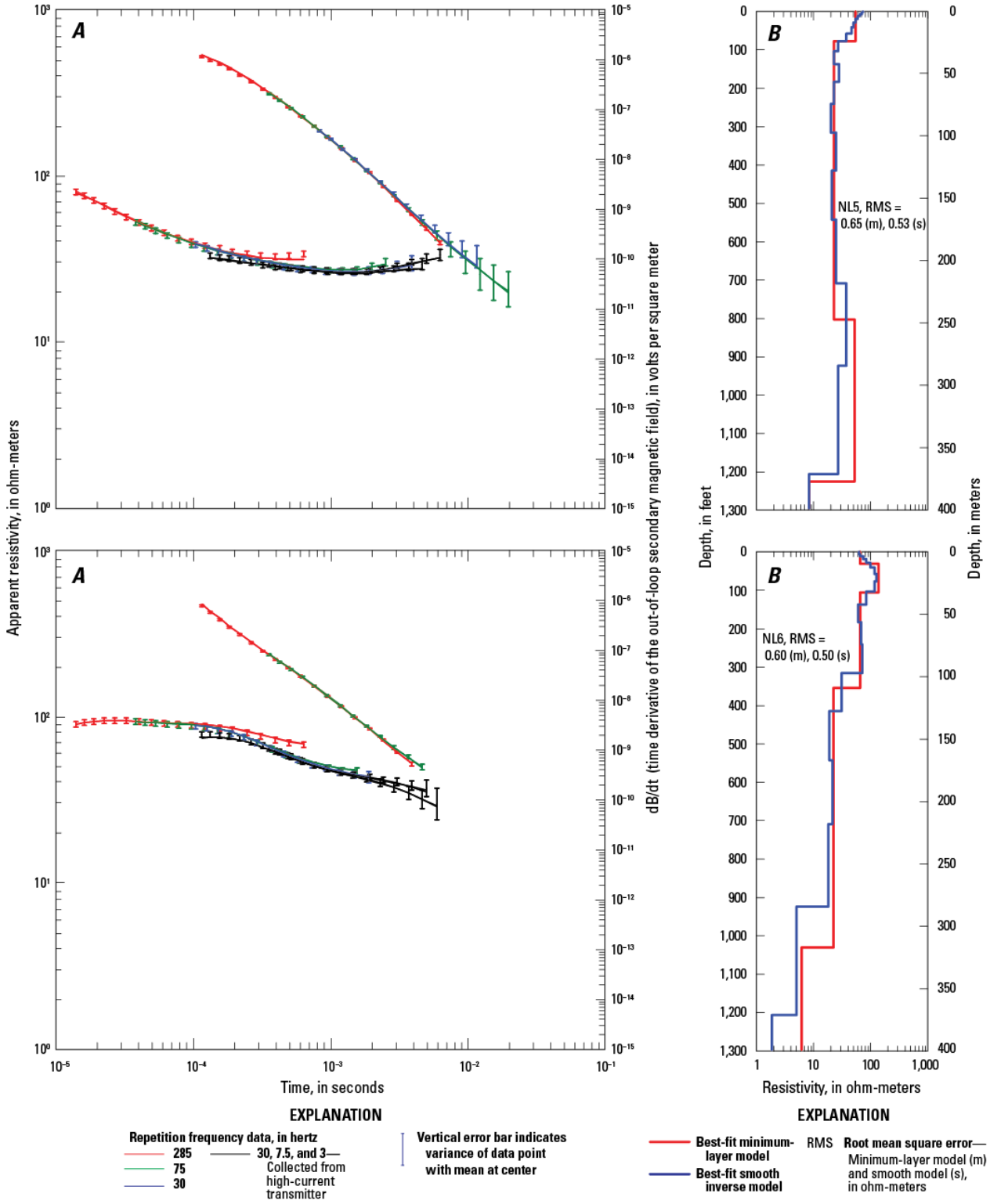

Figure A21. Graphs showing relations between *A*, central-loop resistivity (lower left curve, left axis), out-of-loop vertical magnetic field (time-derivative, upper right curve, right axis), and time; *B*, depth below land surface and subsurface resistivity modeled from TEM sounding for sites NL5 and NL6, Fort Irwin National Training Center, California.

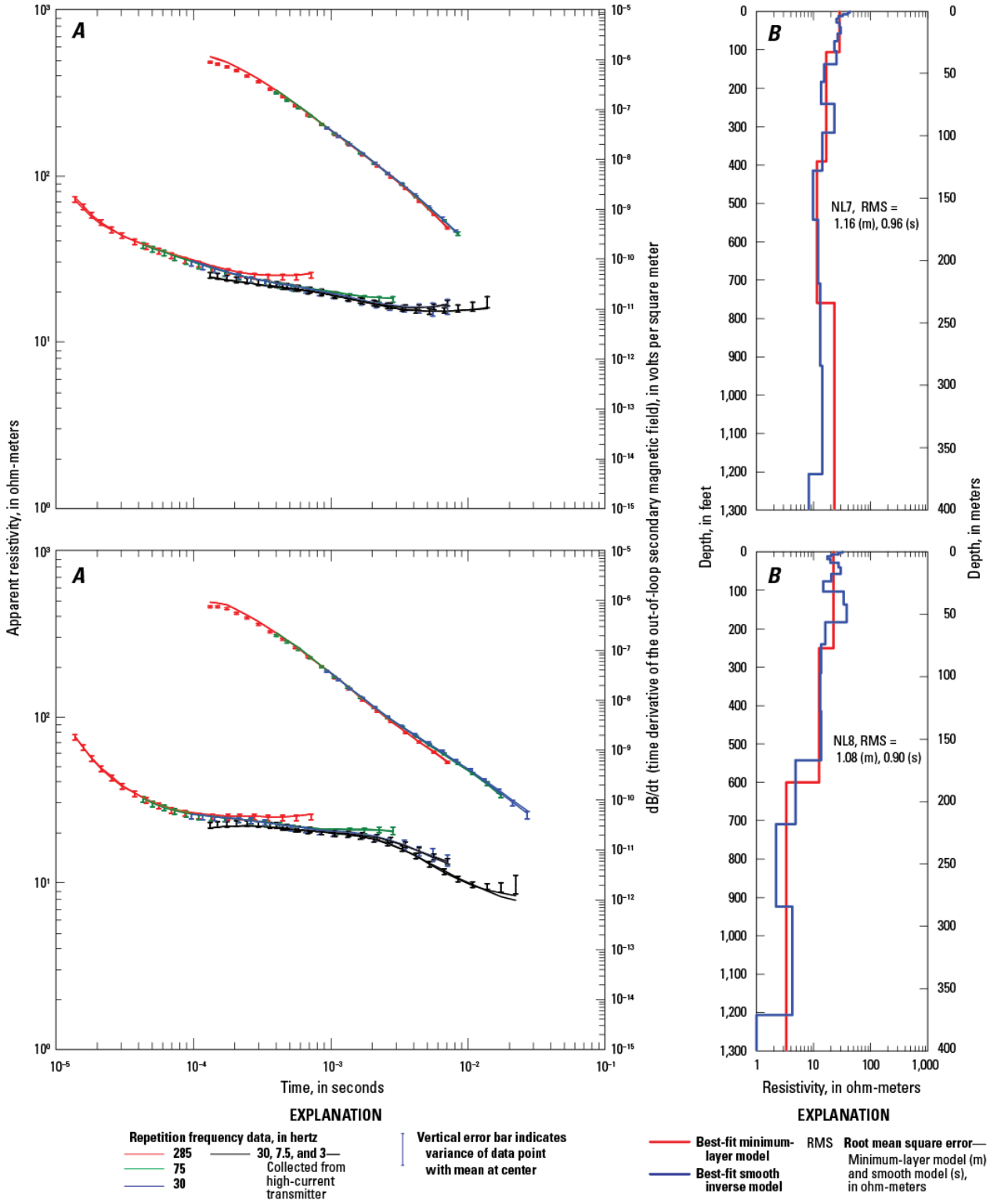

Figure A22. Graphs showing relations between *A*, central-loop resistivity (lower left curve, left axis), out-of-loop vertical magnetic field (time-derivative, upper right curve, right axis), and time; *B*, depth below land surface and subsurface resistivity modeled from TEM sounding for sites NL7 and NL8, Fort Irwin National Training Center, California.

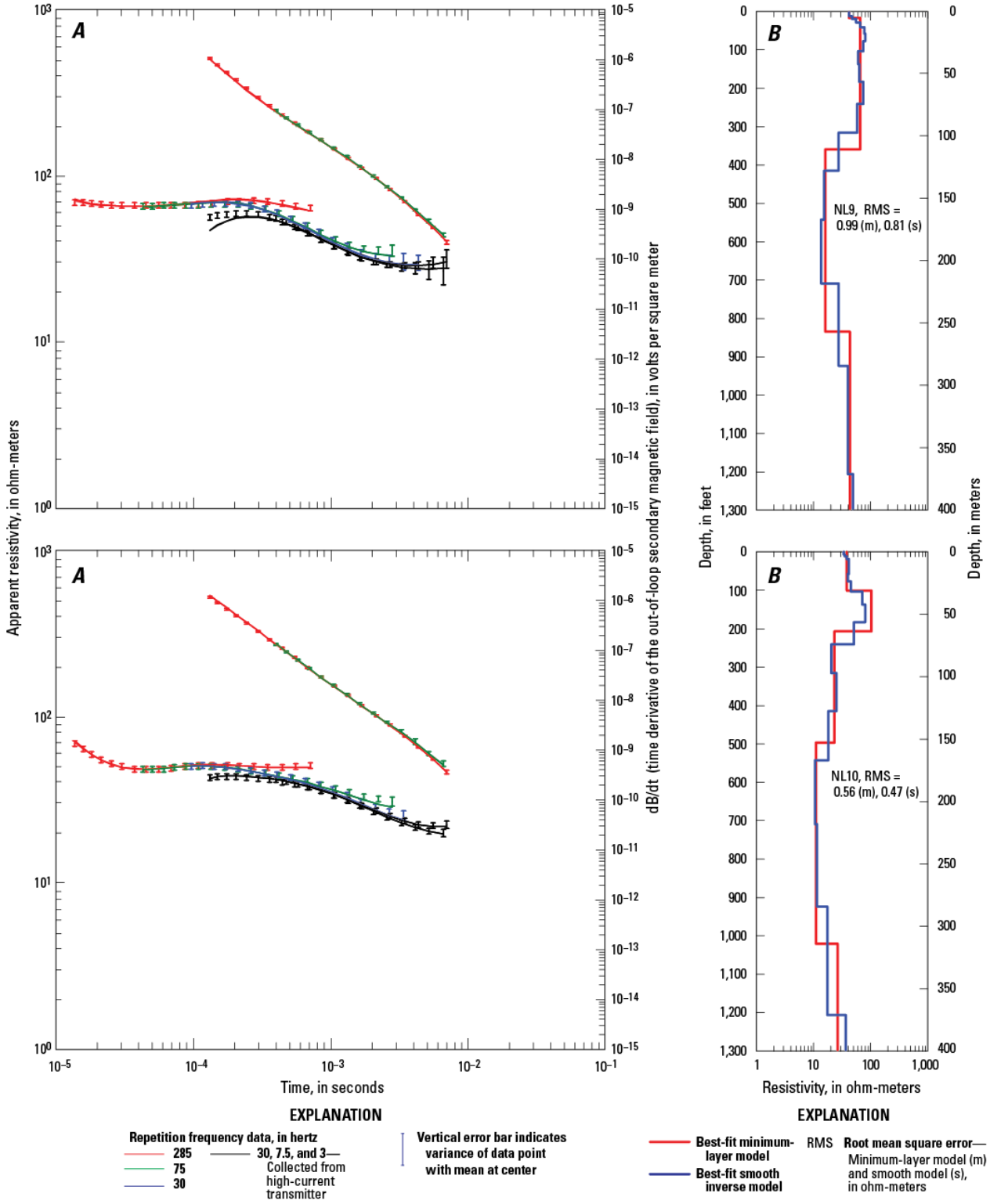

Figure A23. Graphs showing relations between *A*, central-loop resistivity (lower left curve, left axis), out-of-loop vertical magnetic field (time-derivative, upper right curve, right axis), and time; *B*, depth below land surface and subsurface resistivity modeled from TEM sounding for sites NL9 and NL10, Fort Irwin National Training Center, California.

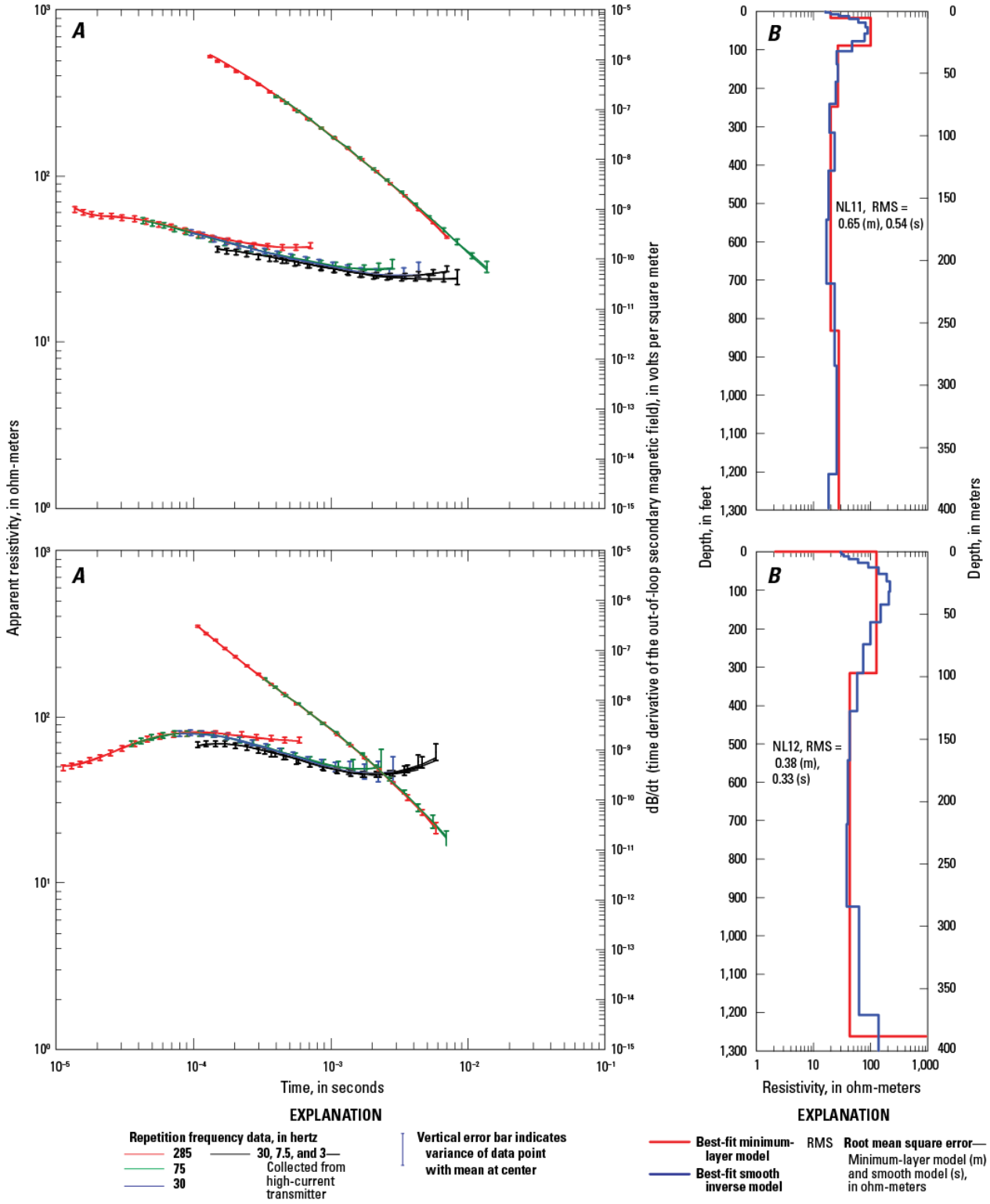

Figure A24. Graphs showing relations between *A*, central-loop resistivity (lower left curve, left axis), out-of-loop vertical magnetic field (time-derivative, upper right curve, right axis), and time; *B*, depth below land surface and subsurface resistivity modeled from TEM sounding for sites NL11 and NL12, Fort Irwin National Training Center, California.

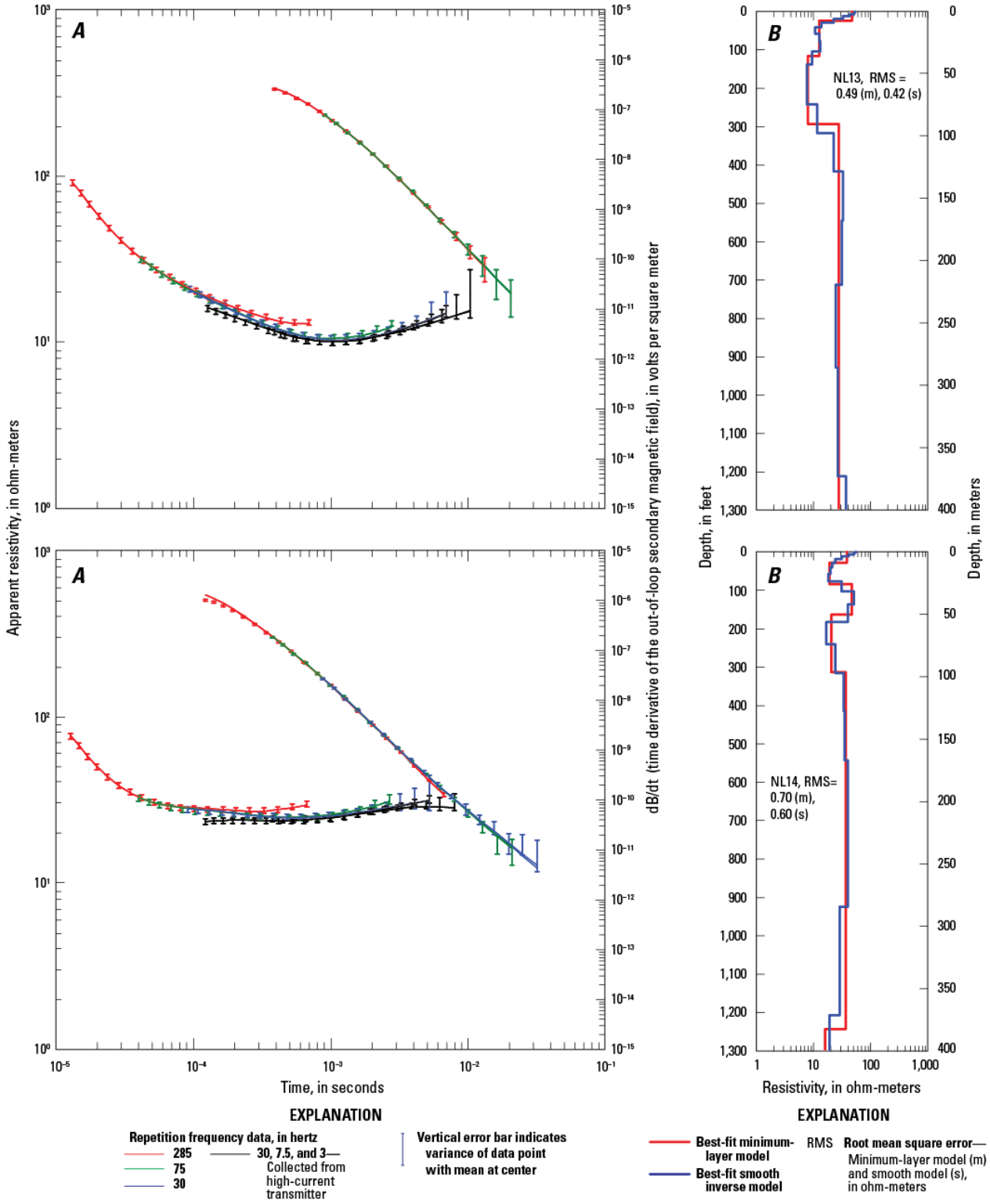

Figure A25. Graphs showing relations between *A*, central-loop resistivity (lower left curve, left axis), out-of-loop vertical magnetic field (time-derivative, upper right curve, right axis), and time; *B*, depth below land surface and subsurface resistivity modeled from TEM sounding for sites NL13 and NL14, Fort Irwin National Training Center, California.

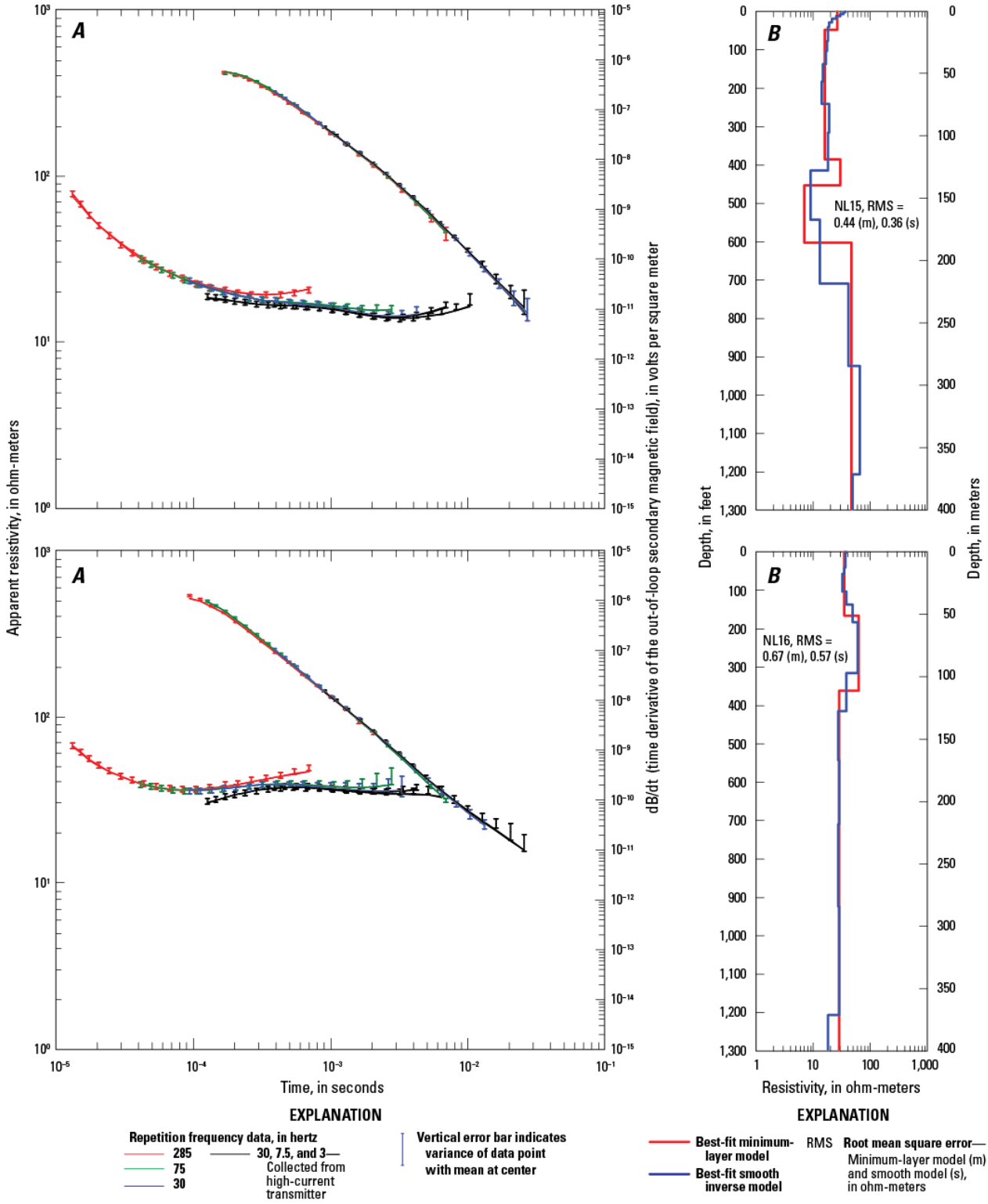

Figure A26. Graphs showing relations between *A*, central-loop resistivity (lower left curve, left axis), out-of-loop vertical magnetic field (time-derivative, upper right curve, right axis), and time; *B*, depth below land surface and subsurface resistivity modeled from TEM sounding for sites NL15 and NL16, Fort Irwin National Training Center, California.

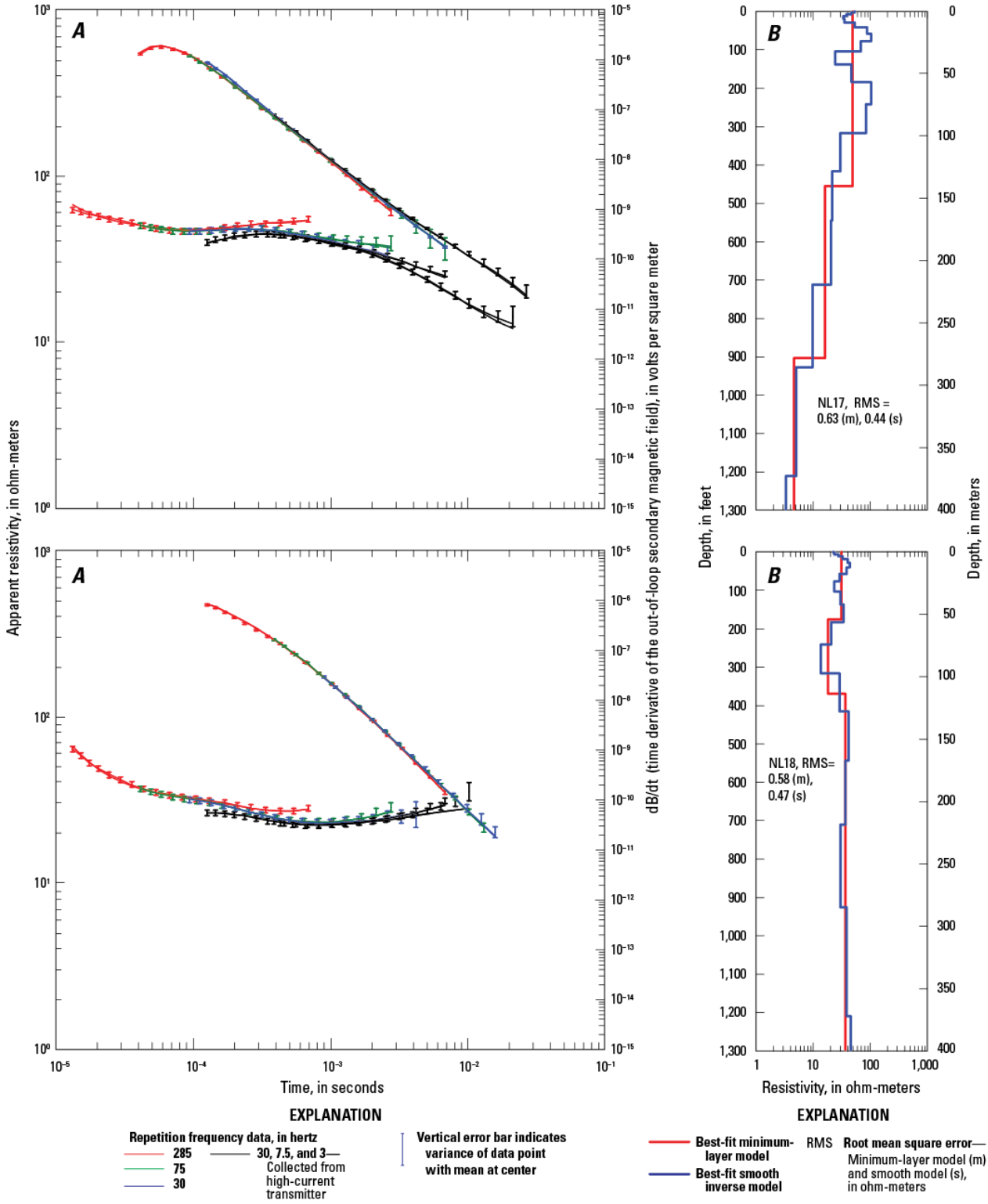

Figure A27. Graphs showing relations between *A*, central-loop resistivity (lower left curve, left axis), out-of-loop vertical magnetic field (time-derivative, upper right curve, right axis), and time; *B*, depth below land surface and subsurface resistivity modeled from TEM sounding for sites NL17 and NL18, Fort Irwin National Training Center, California.

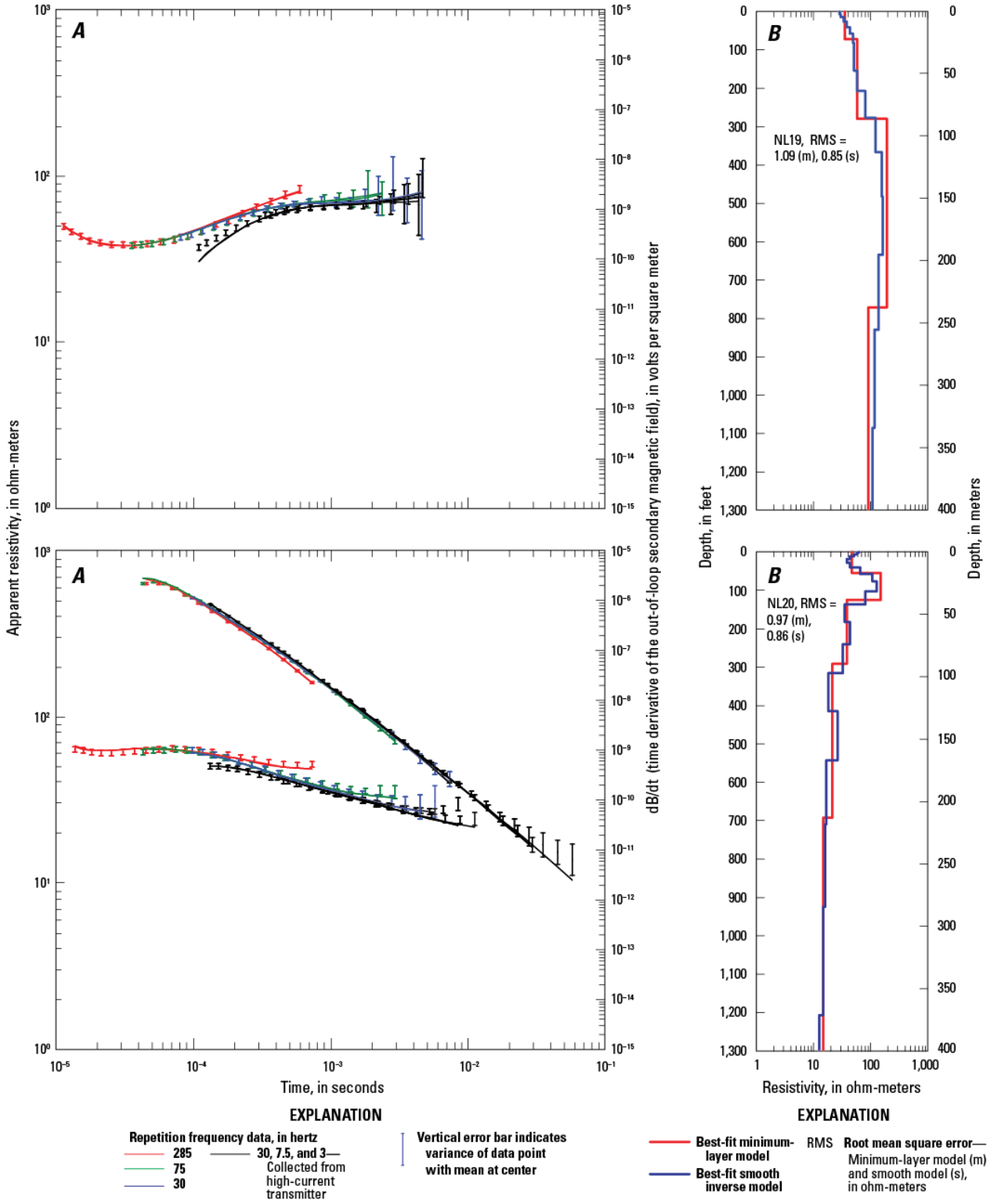

Figure A28. Graphs showing relations between *A*, central-loop resistivity (lower left curve, left axis), out-of-loop vertical magnetic field (time-derivative, upper right curve, right axis), and time; *B*, depth below land surface and subsurface resistivity modeled from TEM sounding for sites NL19 and NL20, Fort Irwin National Training Center, California.

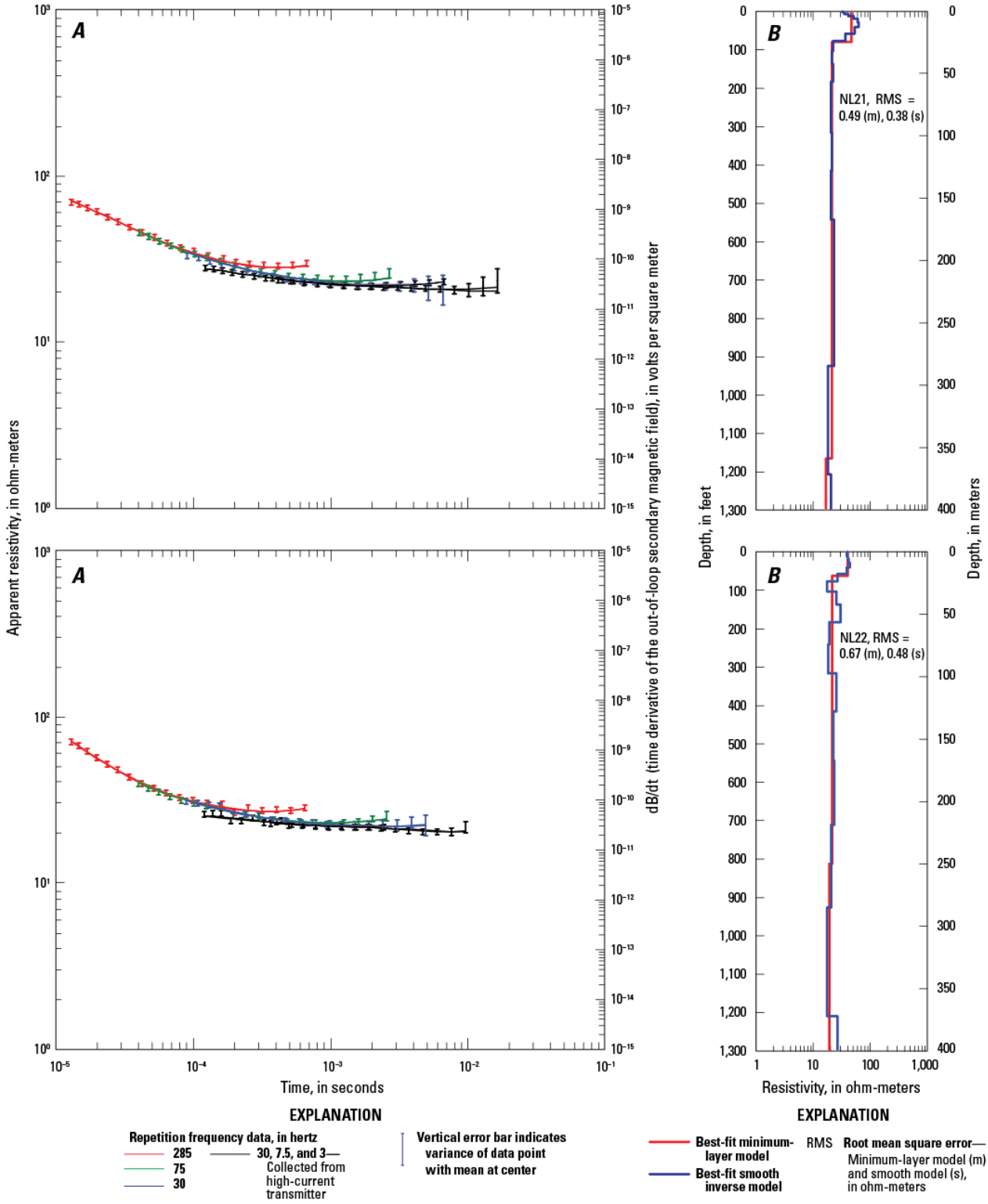

Figure A29. Graphs showing relations between *A*, central-loop resistivity (lower left curve, left axis), out-of-loop vertical magnetic field (time-derivative, upper right curve, right axis), and time; *B*, depth below land surface and subsurface resistivity modeled from TEM sounding for sites NL21 and NL22, Fort Irwin National Training Center, California.

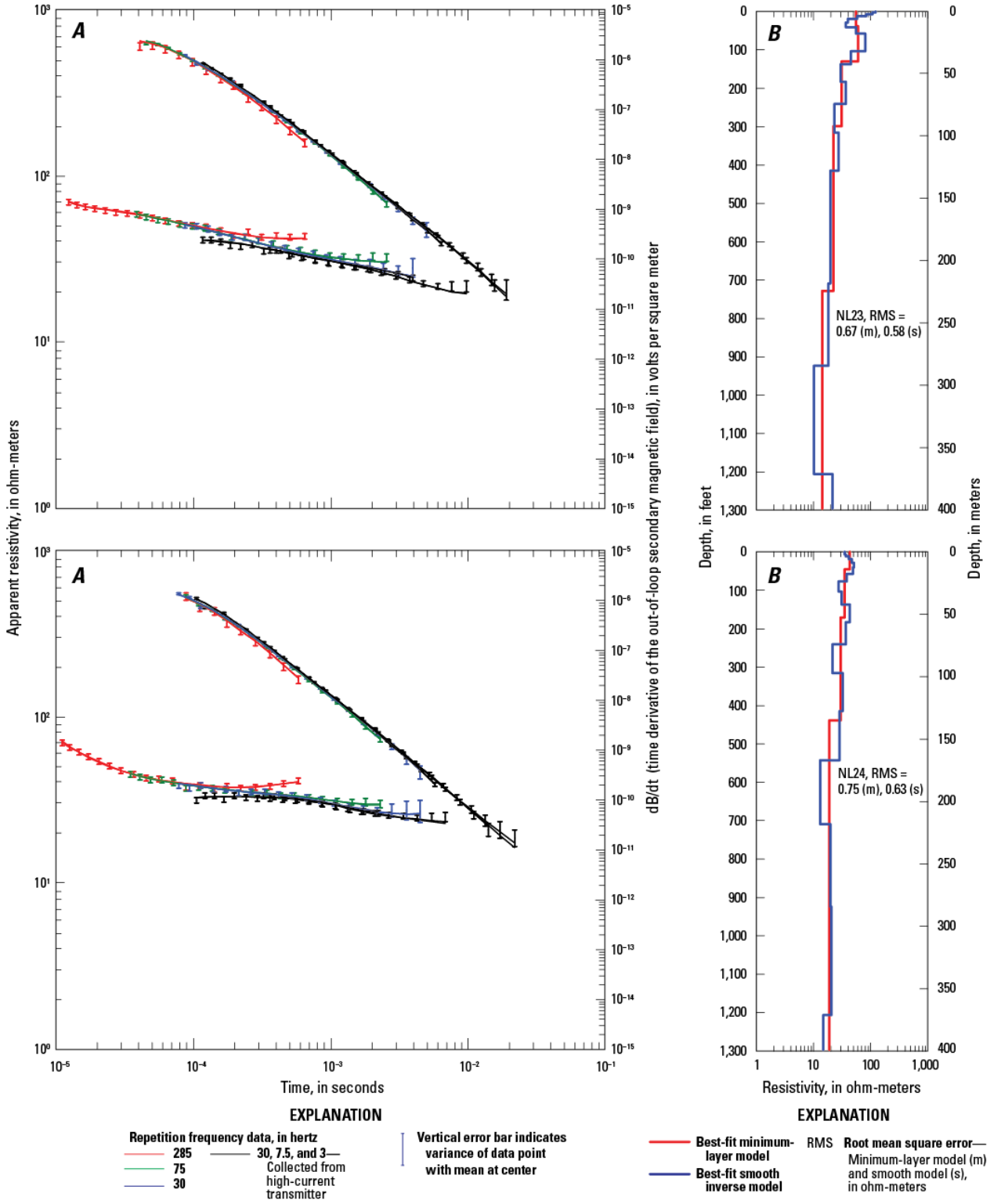

Figure A30. Graphs showing relations between *A*, central-loop resistivity (lower left curve, left axis), out-of-loop vertical magnetic field (time-derivative, upper right curve, right axis), and time; *B*, depth below land surface and subsurface resistivity modeled from TEM sounding for sites NL23 and NL24, Fort Irwin National Training Center, California.

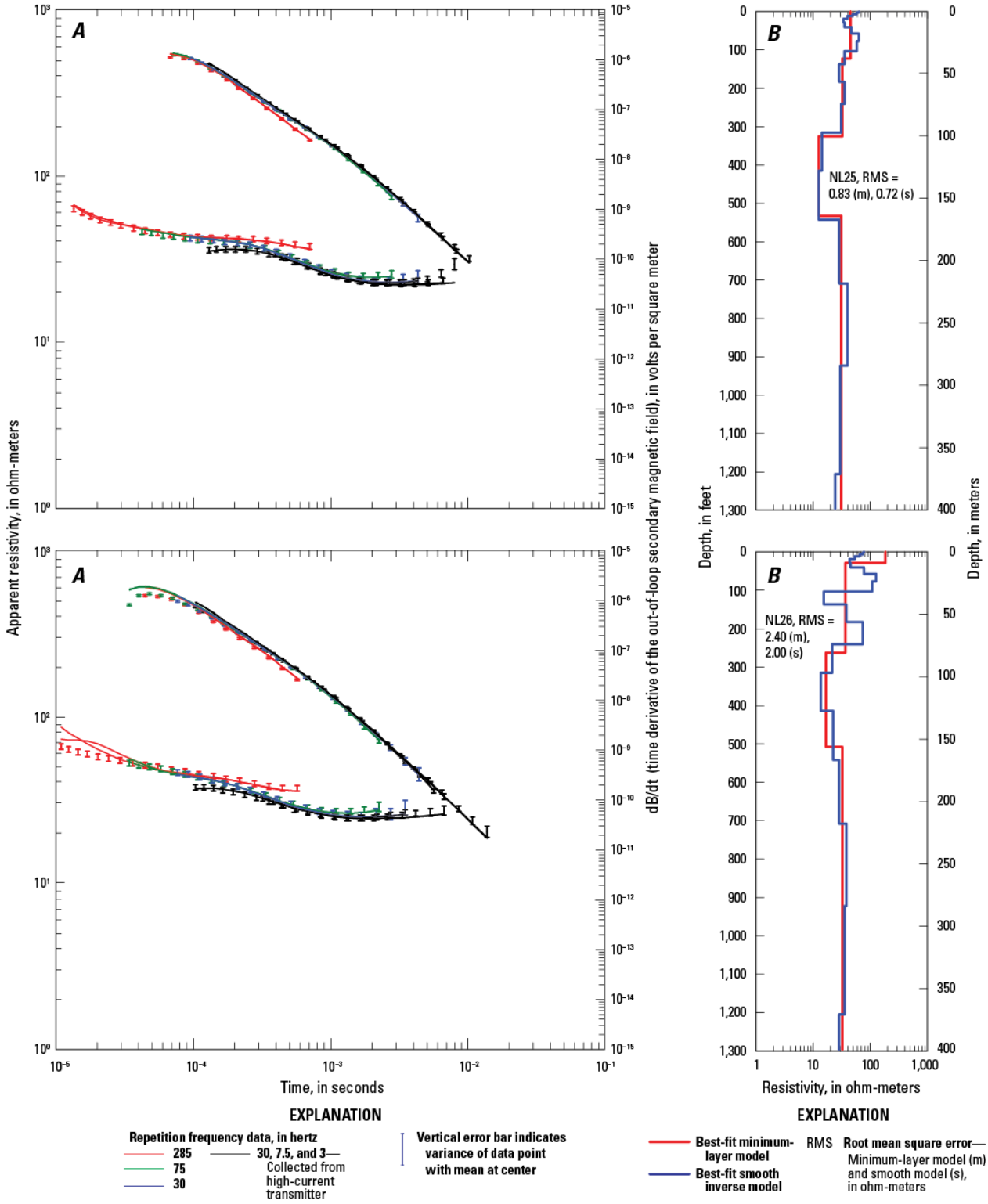

Figure A31. Graphs showing relations between *A*, central-loop resistivity (lower left curve, left axis), out-of-loop vertical magnetic field (time-derivative, upper right curve, right axis), and time; *B*, depth below land surface and subsurface resistivity modeled from TEM sounding for sites NL25 and NL26, Fort Irwin National Training Center, California.

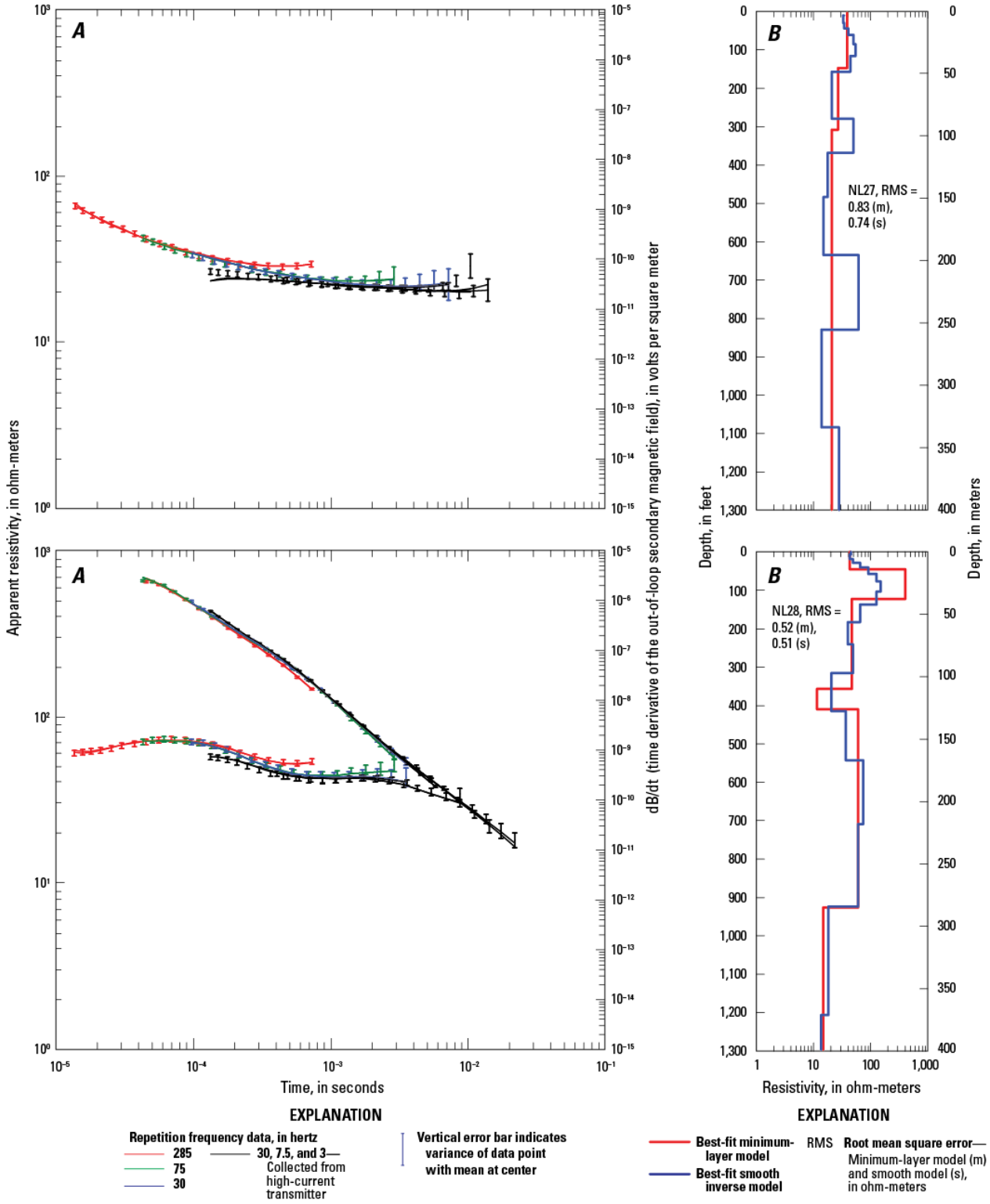

Figure A32. Graphs showing relations between *A*, central-loop resistivity (lower left curve, left axis), out-of-loop vertical magnetic field (time-derivative, upper right curve, right axis), and time; *B*, depth below land surface and subsurface resistivity modeled from TEM sounding for sites NL27 and NL28, Fort Irwin National Training Center, California.

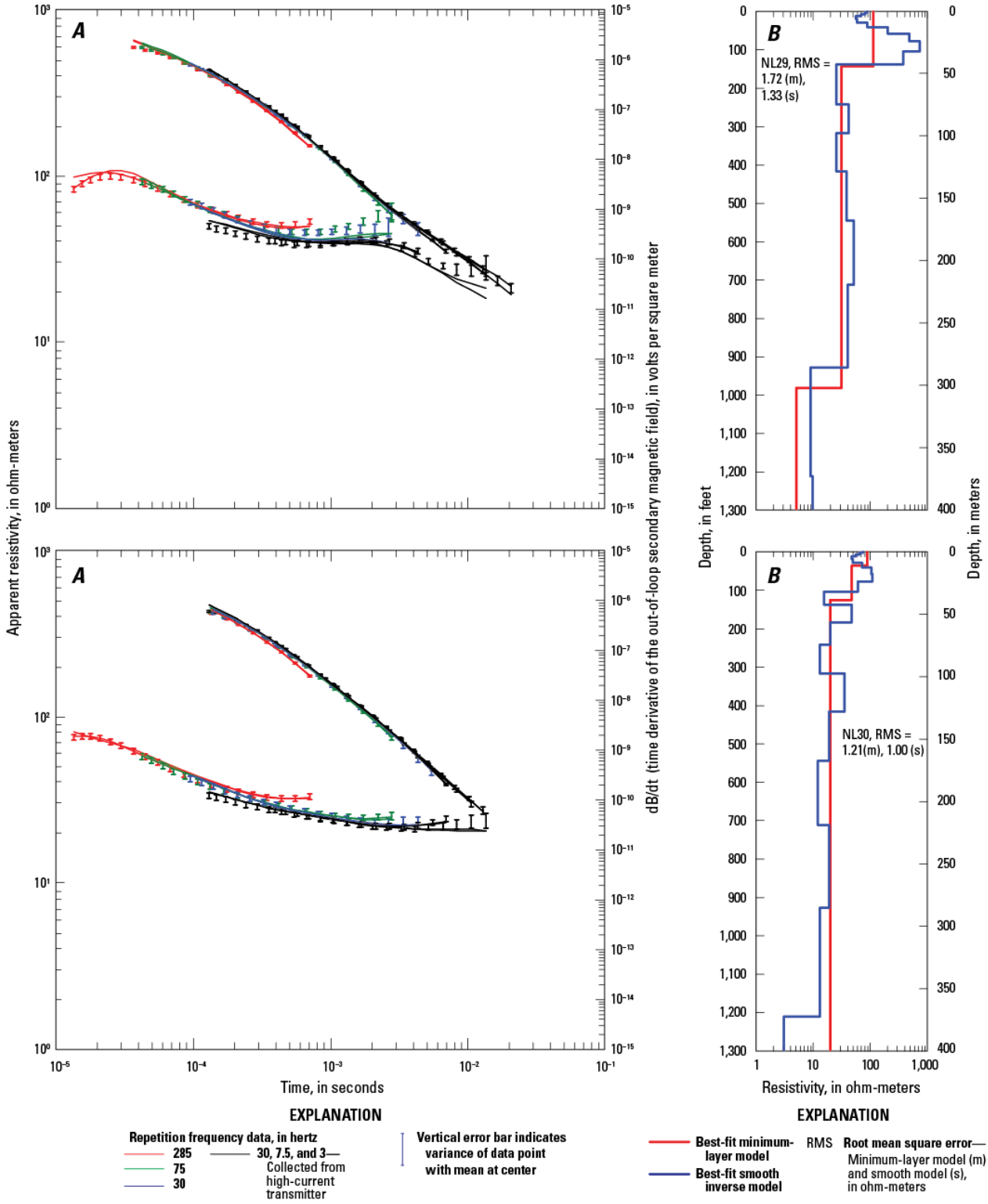

Figure A33. Graphs showing relations between *A*, central-loop resistivity (lower left curve, left axis), out-of-loop vertical magnetic field (time-derivative, upper right curve, right axis), and time; *B*, depth below land surface and subsurface resistivity modeled from TEM sounding for sites NL29 and NL30, Fort Irwin National Training Center, California.

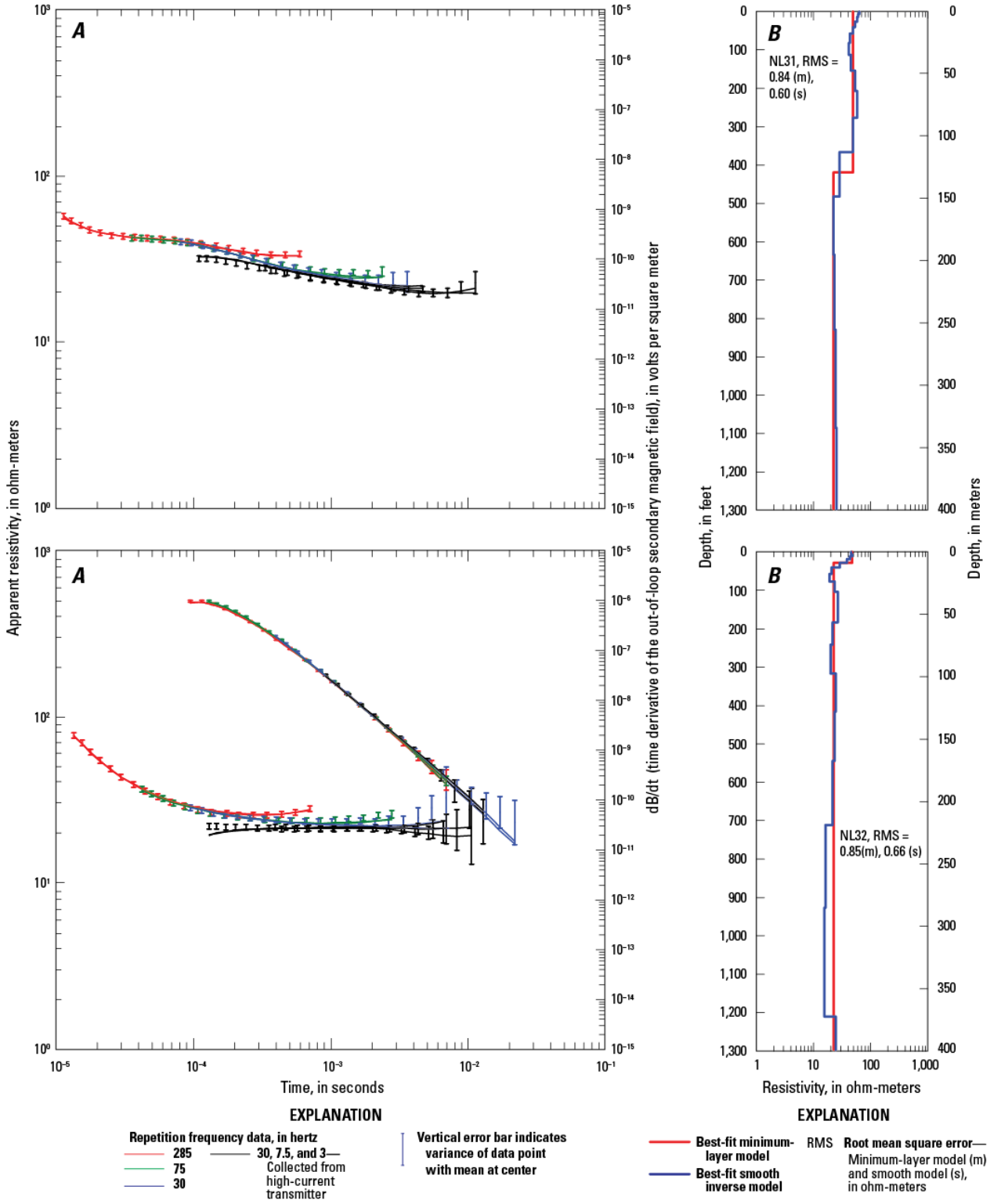

Figure A34. Graphs showing relations between *A*, central-loop resistivity (lower left curve, left axis), out-of-loop vertical magnetic field (time-derivative, upper right curve, right axis), and time; *B*, depth below land surface and subsurface resistivity modeled from TEM sounding for sites NL31 and NL32, Fort Irwin National Training Center, California.

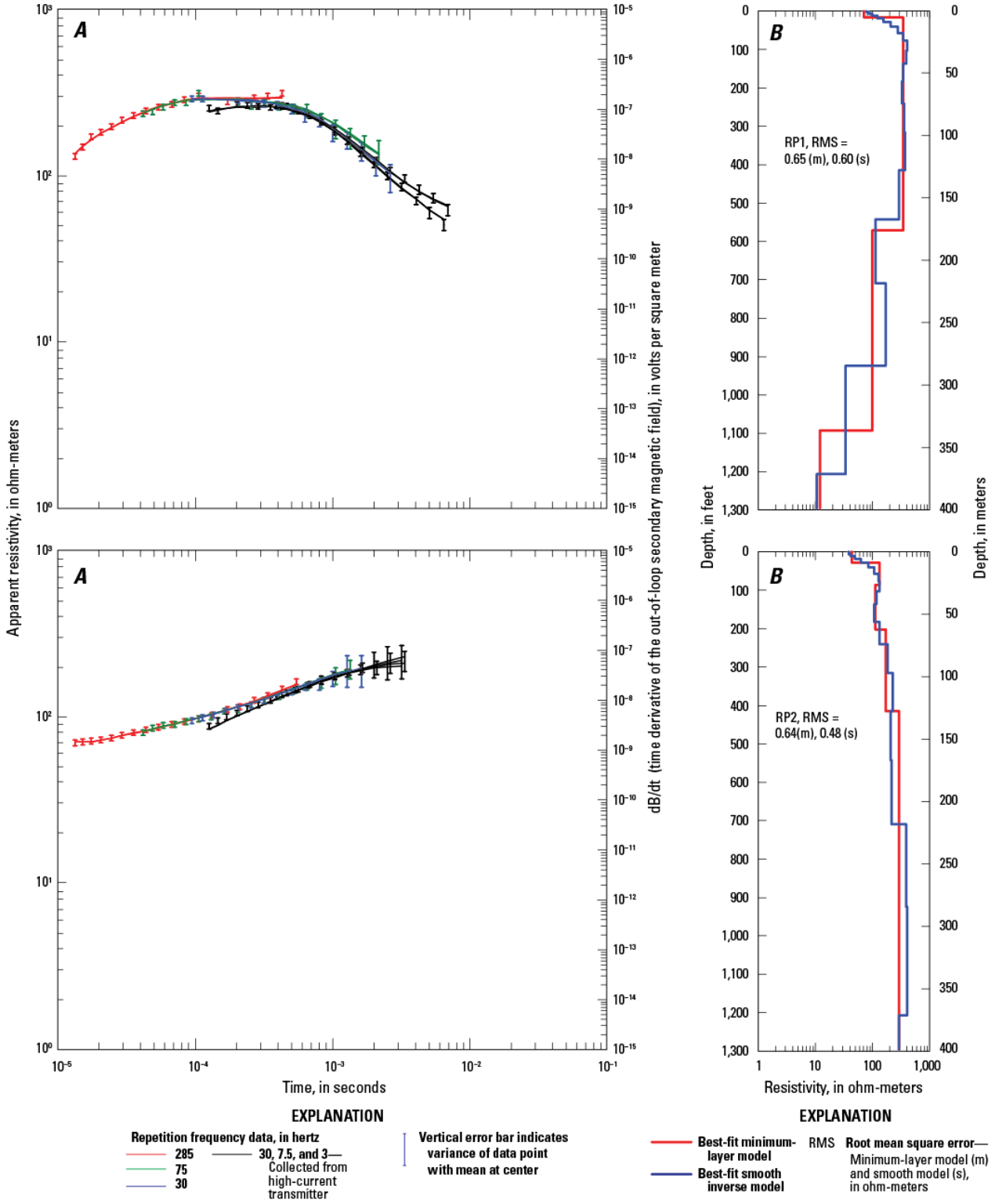

Figure A35. Graphs showing relations between *A*, central-loop resistivity (lower left curve, left axis), out-of-loop vertical magnetic field (time-derivative, upper right curve, right axis), and time; *B*, depth below land surface and subsurface resistivity modeled from TEM sounding for sites RP1 and RP2, Fort Irwin National Training Center, California.

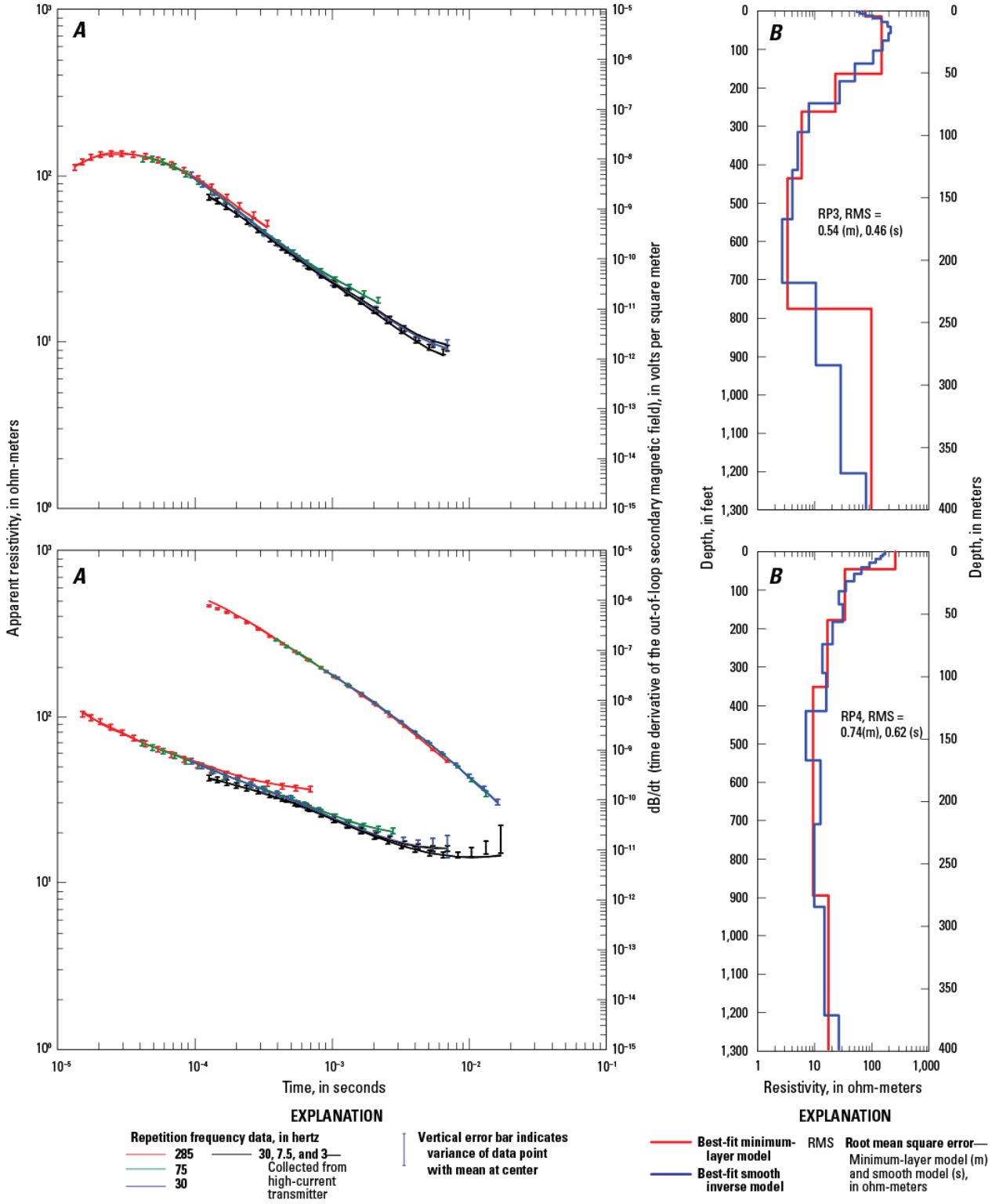

Figure A36. Graphs showing relations between *A*, central-loop resistivity (lower left curve, left axis), out-of-loop vertical magnetic field (time-derivative, upper right curve, right axis), and time; *B*, depth below land surface and subsurface resistivity modeled from TEM sounding for sites RP3 and RP4, Fort Irwin National Training Center, California.

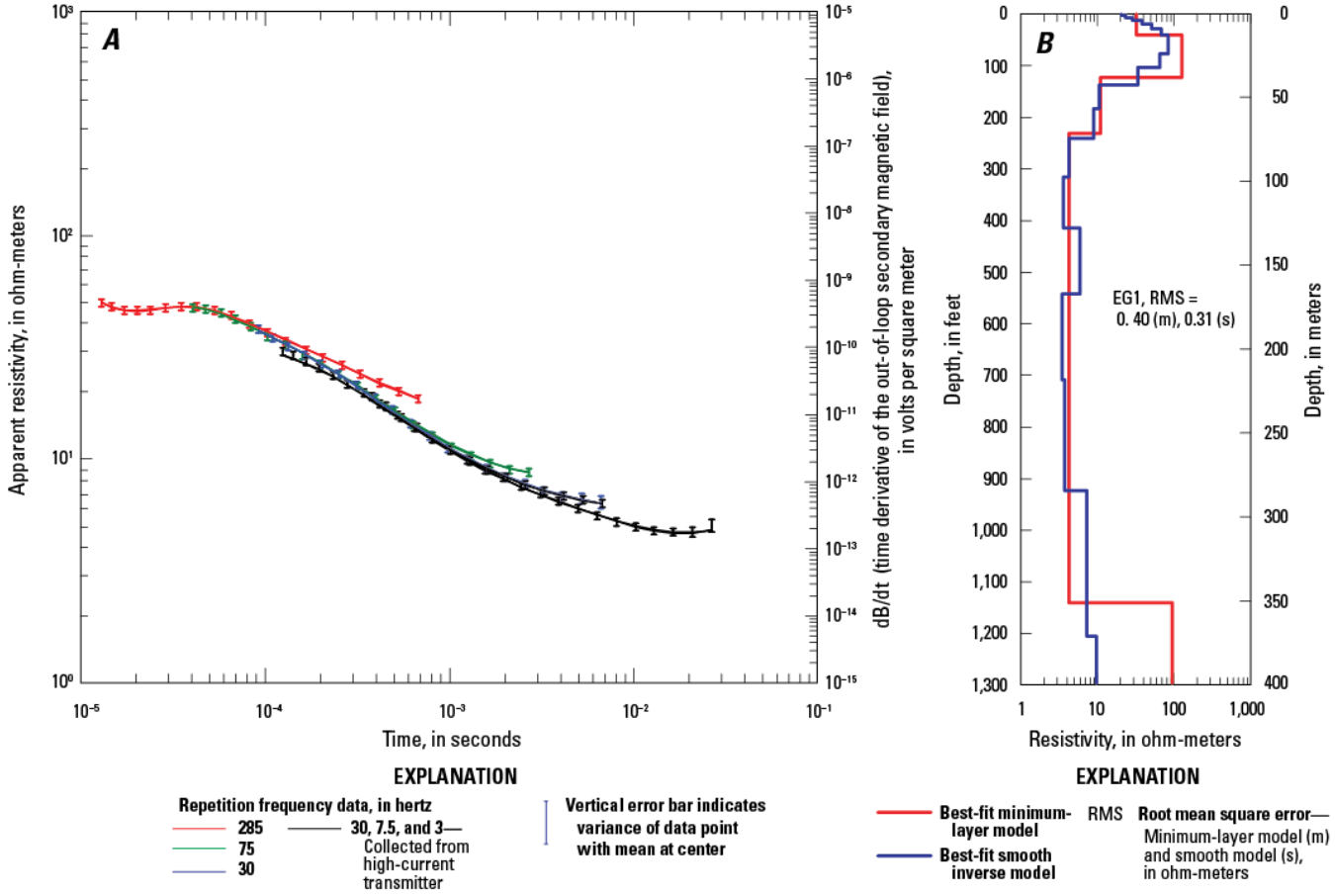

Figure A37. Graphs showing relations between *A*, central-loop resistivity (lower left curve, left axis), out-of-loop vertical magnetic field (time-derivative, upper right curve, right axis), and time; *B*, depth below land surface and subsurface resistivity modeled from TEM sounding for site EG1, Fort Irwin National Training Center, California.

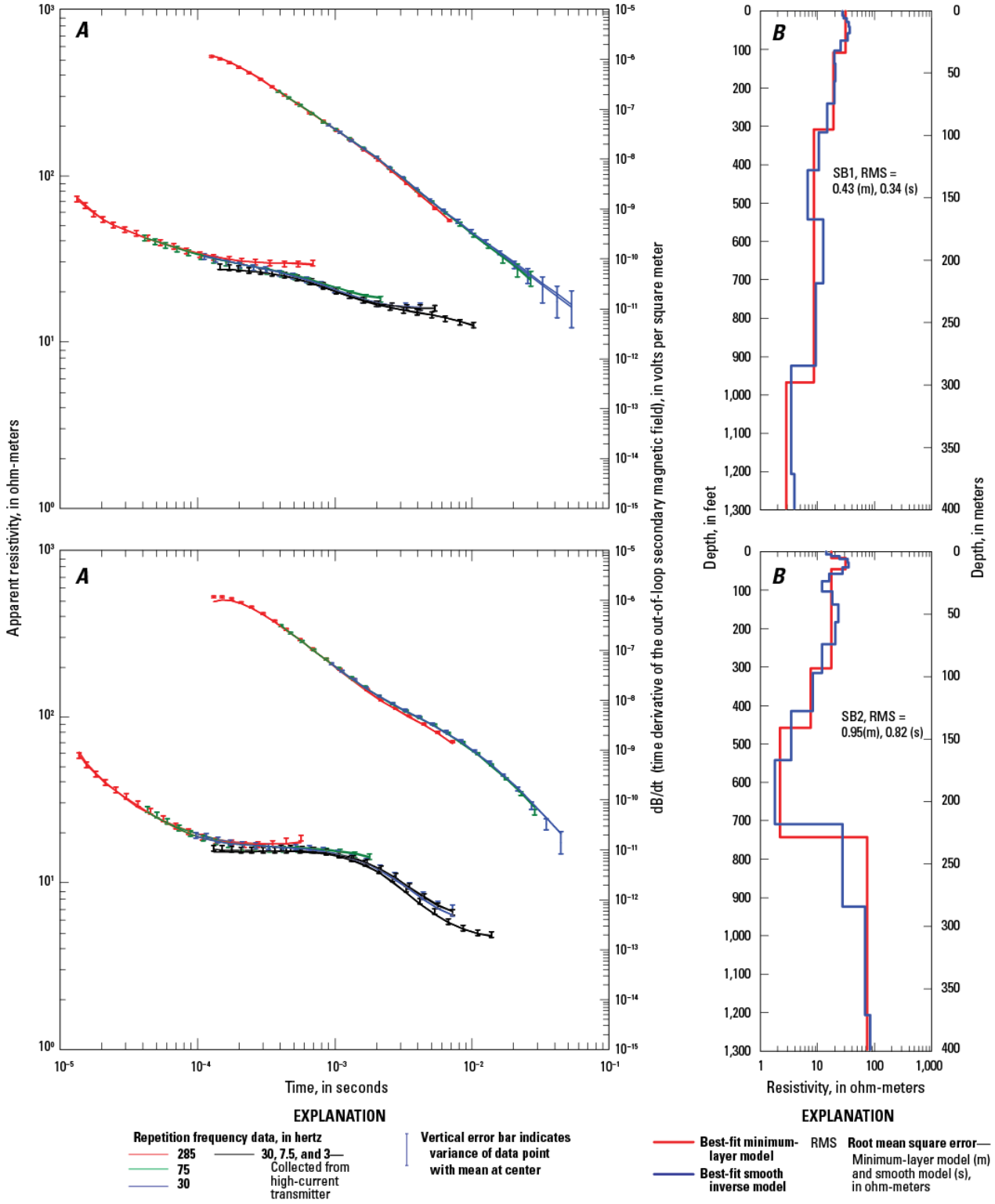

Figure A38. Graphs showing relations between *A*, central-loop resistivity (lower left curve, left axis), out-of-loop vertical magnetic field (time-derivative, upper right curve, right axis), and time; *B*, depth below land surface and subsurface resistivity modeled from TEM sounding for sites SB1 and SB2, Fort Irwin National Training Center, California.

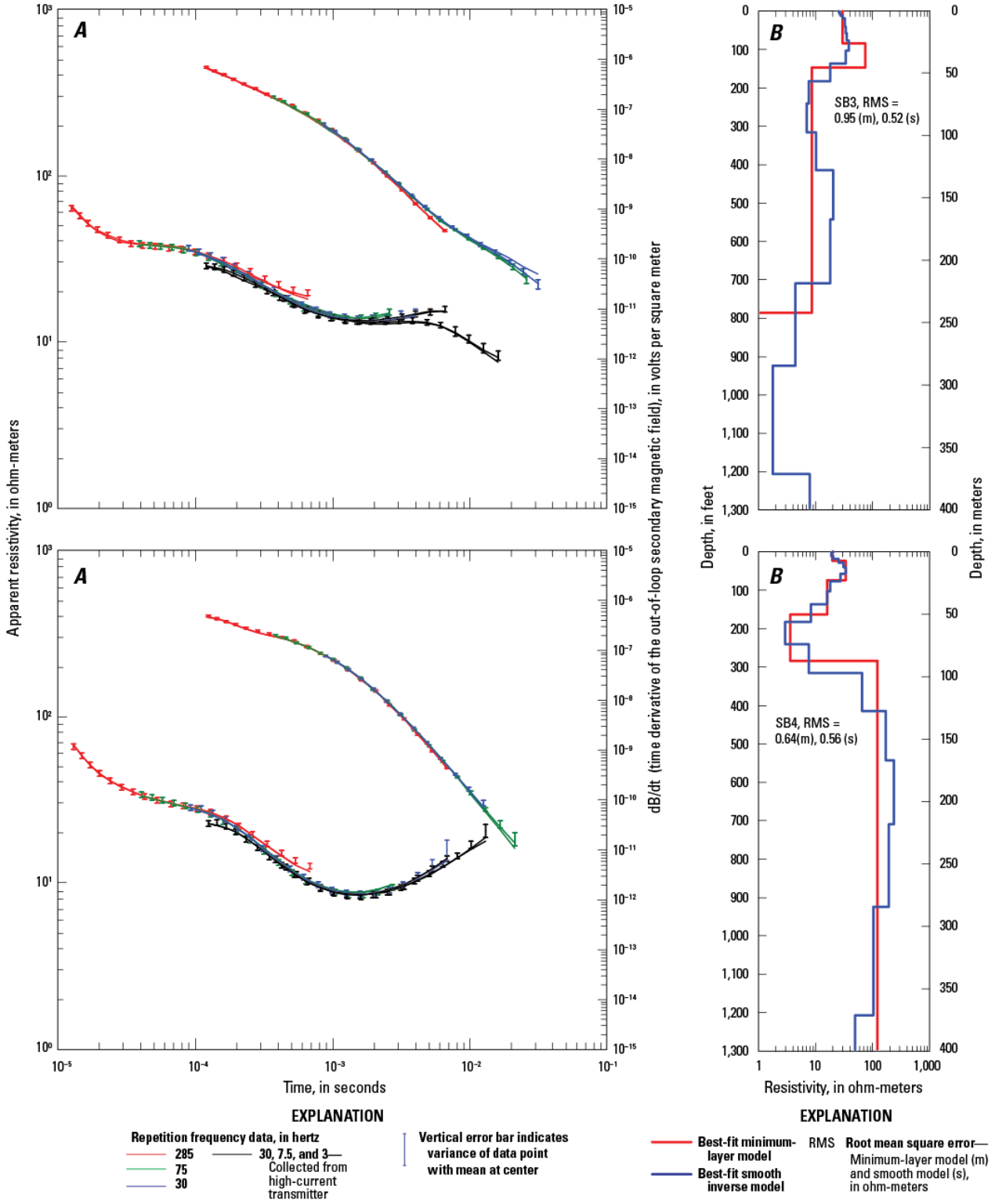

Figure A39. Graphs showing relations between *A*, central-loop resistivity (lower left curve, left axis), out-of-loop vertical magnetic field (time-derivative, upper right curve, right axis), and time; *B*, depth below land surface and subsurface resistivity modeled from TEM sounding for sites SB3 and SB4, Fort Irwin National Training Center, California.